UNIVERSITÉ LIBRE DE BRUXELLES

ÉCOLE POLYTECHNIQUE DE BRUXELLES

PHD THESIS SUBMITTED FOR THE DEGREE OF

DOCTOR IN ENGINEERING SCIENCES AND TECHNOLOGY

Fault location with travelling waves

Xavier BUSTAMANTE MPARSAKIS

Thesis director

Prof. Jean-Claude Maun - BEAMS Electrical Energy

ÉCOLE POLYTECHNIQUE DE BRUXELLES

UNIVERSITÉ LIBRE DE BRUXELLES

February 4, 2018

Abstract

Travelling wave fault locators (TWFL) have the possibility to get rid of the limitation of typical locators based on the 50Hz impedance. Their principles were invented in the early 1900's, but only recently became economically viable. Some TWFL devices are now commercialized.

Despite the recent commercialization of TW fault locators, actual field experience of TWFL is hard to acquire and rarely presented in the literature. Due to this, most studies are based on simplified simulation models.

Practical experience in the form of TW records are important. It is the basis to understand the practical difficulties of applying TWFL algorithms. It is also necessary to illustrate the simulations limitations, and to test algorithms on real records.

The work performed in this thesis was supported by Siemens with the hope to develop TWFL devices based on the results. The aim of the work was first to acquire experience in the practical side of TWs and their recording in substations. Based on this practical experience, the second objective was to study a TWFL that includes a new method for wave detection: the pattern recognition algorithm (PRA).

The practical experience was acquired with a measurement campaign performed in the Belgian transmission network, and with laboratory tests that reproduce the measurements of currents inside a substation.

Fault records suitable to TW studies were acquired during the measurement campaign, and are analysed in this report. The fault records and the laboratory tests highlighted and characterized the impact of the substation measurements on the waves recorded. Modelling those measurement systems is shown to improve the accuracy of the simulation tools.

This report also presents a theoretical development of the PRA. The algorithm is adapted to take into account the practical difficulties previously analysed. An applicable version of the algorithm is proposed and tested.

The algorithm proposal provides a precision better than 300m when applied to the simulation models. This precision varies with the set of parameters used, with the line topology, and with the fault location. On the field record acquired, the algorithm provides the fault location with a precision of 110m.

A prototype has been developed by Siemens, and some devices have been installed at the end of this thesis. The TW records that will be acquired by those prototypes will provide a significant help in continuing the work presented in this report.

Acknowledgements

I would like to take the opportunity to thank the many people that contributed, directly or indirectly, to this project.

First of all, I thank my thesis promoter, Prof. Jean-Claude Maun, for the opportunity to work on this project. His expertise on the subject and the numerous advices throughout the whole project were invaluable. I appreciated the work flexibility that he offered, and our various trips to Berlin.

I thank Siemens for their support of this project: to Matthias Kereit for managing the team, and to Cezary Dzienis, Michael Claus, Bert Winkler, Andreas Jurisch and Jorg Blumschein for their precious input during our meetings.

I also thank the 'Fondation Jaumotte-Demoulin' and the 'Fonds David and Alice Van Buuren' for funding the writing of this document.

I express my gratitude to Elia for allowing the installation of devices in their substations. In particular to Benjamin Genêt and Caroline Bosschaert for managing the operation, and to Joeri Duhau for the practical help provided during the campaign.

I also thank the technical team from the BEAMS, Christophe and Geoffrey, for their practical help provided during the laboratory tests.

A considerable thank goes to my colleagues at the BEAMS department for providing a fantastic environment. They contributed to 4 amazing years. I can confidently say that many of you will remain close friends well beyond this PhD. Our always shifting traditions such as the 'café chantilly', badminton, mini-basketball and 'diner presque-parfait' will be deeply missed.

Finally, to my friends and family whose love and support helped me grow as a person these past few years: thank you.

Contents

List of Figures

List of Tables

List of Abbreviations

AC	**A**lternative **C**urrent
CT	**C**urrent **T**ransformer
DC	**D**irect **C**urrent
EM	**E**lectro **M**agnetic
EMTP	**E**lectro **M**agnetic **T**ransients **P**rogram
FL	**F**ault **L**ocation
HV	**H**igh **V**oltage
LCC	**L**ines (and) **C**ables **C**onstant
LSE	**L**east **S**quare **E**stimation
MT	**M**easurement **T**ransformer
MV	**M**edium **V**oltage
PRA	**P**attern **R**recognition **A**lgorithm
TSO	**T**ransmission **S**ystem **O**perator
TW	**T**ravelling **W**aves
VT	**V**oltage **T**ransformer

Introduction

Context

The power network is the electrical grid used for delivering the electricity to the consumers. The electricity is transmitted from the power stations, in which it is produced, to the consumers. This transmission occurs through high voltage transmission lines or underground cables.

The transmission lines consist of aerial conductors that can transport the electricity. They are elevated thanks to big metallic towers that are placed every few hundreds of meters. Because those towers are metallic and conduct electricity, they cannot directly be connected the conductors. Doing so would lead to the current flowing through the towers instead of the conductors only. To avoid this, insulators are used. They offer a mechanical support between the tower and the conductor, without allowing the current to flow through them.

Faults frequently occur in transmission lines. They are most commonly caused by a lightning stroke hitting the line, causing the breaking of insulators. An arc will be generated, allowing the current to flow across the insulator, from the line to the tower and to the ground. Faults can also be caused by a multitude of different events, such as snow accumulating on the line, a tree falling down, man-caused incidents, etc.

During a fault, the current flowing inside the system usually rises to high levels. This high current is dangerous and might deteriorate elements of the network. It is therefore important to detect those faults rapidly, and to isolate the faulted line section to stop the high current from flowing. This is the task of protection algorithms running inside protection relays.

After the protection occurs and the faulted line section has been isolated, the arc has faded and the current flowing through the line and across the isolator stops. If the isolator has not been permanently damaged, it will operate correctly again when the line is re-energized. The power network will then operate correctly. If the isolator has been permanently damaged, an arc will

re-appear, and the fault remains. The isolator has to be replaced before the line can be put back in operation.

Knowing the fault location is therefore of significant importance. It helps the system operator dispatch repair teams at the correct place to solve the problem, whereas without fault location, a visual inspection has to be performed along the faulty line. This can take a lot of time for long lines, or for lines that present a difficult physical access.

Fault location and protection algorithms

Protection and fault location algorithms are important to the safe and reliable use of the power network. They are therefore subject to many past and ongoing researches to improve their performances. A good protection should act quickly after a fault, with a good security (the protection won't activate if there is no fault in the monitored line) and selectivity (it will function consistently if the fault is in the line). A good fault location should provide a precise fault location, with a good reliability (for as many faults as possible).

Nowadays, the most widely used algorithms for protection and fault location are based on the measurement of the 50Hz line impedance [1]. In these methods, the voltages and currents are measured at one or both ends of the line. With those measurements, the impedance to the fault is computed and converted into a physical distance based on the knowledge of the line impedance.

While these methods are efficient most of the time, they have some limitations. The protection algorithms requires at least a half period of measurements. This leads to a tripping time higher than 10ms. The fault location algorithms can have a low precision due to the low accuracy of the zero-sequence impedance and to the high impedance of some faults. Typically an impedance fault locator has a precision better than 2 % of the line length, which for long transmission lines can represent a significant distance.

Due to those limitations, there is an interest in the development of alternative algorithms. In particular, algorithms based on travelling waves theoretically have the possibility to get rid of those limitations.

Travelling wave fault locators

Travelling waves (TWs) are electro-magnetic (EM) transients generated when a sudden voltage disturbance occurs [2–5]. This will happen for the majority of the faults occurring on overhead lines. Those EM transients propagate in overhead lines in both directions starting from the fault point. They have a propagation velocity close to the speed of light in overhead lines. The propagation velocity of TWs in a specific line can be computed if the geometrical data is available [2].

The theory of TWs can be used in fault location (FL) algorithms. The theoretical principles of fault locators based on TWs were invented in the early 1900's [6, 7]. Such methods have the theoretical advantage of being more precise than classical impedance based FL, even for high impedance faults.

If the propagation velocity and the length of the monitored line are known, the fault location can be computed based on the measurement of the arrival times of the TWs. TW FL algorithms can either be passive (using the waves generated during the fault) or active (generating travelling waves to be reflected on the fault point). They can also either be two-ended (recording arrival times of the first wave at both ends of the line), or one-ended (recording the arrival times of the first wave and first reflected wave at one end of the line).

While the principles of such fault locators have been well known for decades, they require the measurement of the arrival time of the TWs with a good precision. Due to their high velocity, an error of 1 μs in the arrival time measurements introduces an error of almost 300m in the fault location. A high sampling frequency is therefore needed to have a good accuracy in the arrival time measured (typically higher than $1MHz$). For the two-ended algorithms, a time synchronization with a good precision is also required. Those technologies only recently became affordable. For that reason, TWFL is an emerging technology. A few TWFLs are now commercialized [8–11].

Motivations

This project focuses on the study of fault locators based on travelling waves in high voltage transmission overhead lines. The work has been supported by Siemens with the hope of developing future devices based on the results from this project. As such, an emphasis was put on the practical side of the

study, and on the limitations and difficulties to apply such algorithms on real transmission lines.

Actual records of faults that occur in the network are difficult to find. They require a high sampling frequency and are expensive to obtain. There is then little incentive for the record owners to share them. For this reason, most studies are based on simulations. Some studies from the literature are validated with field records [12–15], but the experience acquired is seldom discussed in detail such as in [14, 15].

Simulation tools available in the literature accurately represent the overhead lines for travelling waves studies [16–19]. However, the effect of substation measurements on the travelling waves is still an ongoing research topic. Those substation measurements have a significant effect on the travelling waves and might affect the precision of the algorithms used [20–23].

The precision of a TW fault locator is dependent on the measurement precision of the TW arrival times. The simplest and most common way to detect the waves arrival times is by using a threshold. This method is subject to error notably due to the attenuation and distortion that occur when the waves propagate inside the overhead lines. Most work performed on the subject of TWFL are related with the improvement of those measurements [13, 24–34].

Developing more complex algorithms is a challenging task due to the lack of information on the effect of the travelling waves measurements. A method could provide good results with perfect primary records, but fail with the imperfect measurements available.

This project aimed first at reviewing the TWFL literature, at doing a preliminary study of the subject, and at acquiring experience in the practical side of TWs and the effect of their measurements. This was done with laboratory testing of measurement transformers, and with a measurement campaign in the Belgian transmission network, where travelling waves generated during a fault were recorded. Based on the positive outlook of this work, some prototypes have been developed and installed by Siemens with the objective to acquire more TW records.

The second objective of this project was to use the experience acquired to improve and validate simulation models and study a new wave detection algorithm while keeping the practical limitations in mind. These analysis were based on the fault records and laboratory tests. They will be improved and validated with the additional fault records from the installed prototypes. Due to the time frame linked to the development, installation and recording of faults, these additional analysis are not part of this thesis.

Structure of the thesis

This document reports the study of a two-ended fault locator based on TWs. This fault locator uses a new algorithm for wave detection, the pattern recognition algorithm. The study was based on laboratory tests, on fault records acquired in the Belgian transmission network, and on simulation tools developed thanks to the practical experience acquired.

The report is divided in two parts. Part I refers to the theoretical side of the study, and part II describes the practical tests and simulations, and their results. The report has been designed so that each part could be read and understood independently. The results presented in part II are referred to the theory described in part I.

Part I starts with a presentation of the concept of TWs in Chapter 1. Their properties are highlighted and mathematically developed. The state of the art of simulation tools is presented in Chapter 2. They are used to illustrate the basic TW concepts from Chapter 1. The different FL algorithms based on TWs are described in Chapter 3, focusing on their practical challenges and limitations. Chapter 4 presents the new wave detection algorithm studied in part II, the PRA.

Part II first describes the practical tests and their results: the laboratory testing of measurement transformers (Chapter 1) and the measurement campaign in the Belgian transmission network (Chapter 2). The simulation models from part I are improved and validated in Chapter 3 with the practical test results. Finally, the FL algorithm presented in part I is analysed in Chapter 4 with those simulation tools and with the fault record from the measurement campaign.

Publications

Three papers have been presented at international conferences based on this work:

- Powertech 2017: "Travelling wave fault location based on pattern recognition". This paper presents the theoretical development of the pattern recognition algorithm. This is the topic of Chapter 4 of this document.
- IPST 2017: "Fault locator using travelling waves: experience in the Belgian transmission network". This paper presents the measurement campaign and analyses its results. It is the topic of Chapter 6.

- Pacworld 2017: "Travelling wave fault location based on pattern recognition: Application to complex topologies and field records". This paper presents the application of the pattern recognition algorithm to different topologies, and the analysis of its limitations. It is the topic of Chapter 8.

Part I

Theory

Part I develops the theoretical side of the study.

In Chapter 1, the theory of TWs is described in detail. The general concept and their different properties are first explained and illustrated. Their mathematical developments are then proposed. The limitation of practically recording TWs are then discussed.

In Chapter 2, the state of the art of the simulation tools for high frequencies are presented. These models are used to illustrate the theory from Chapter 1.

In Chapter 3, the fault location algorithms based on TWs are presented. They are updated for more general situations, where the lines are non homogeneous. The practical considerations to apply them are discussed in detail.

In Chapter 4, the PRA is developed. This algorithm is a new method to detect the difference of arrival times of TWs, used in the algorithms presented in Chapter 3. The PRA is first mathematically developed and illustrated. The practical difficulties are then discussed, and the complete fault location algorithm is presented, before being analysed in part II.

Chapter 1

Travelling waves

Travelling waves (TWs) are the propagation of electro-magnetic (EM) transients in the transmission network. They are generated in the power network

when a sudden change of voltage occurs. Many events can cause this sudden change of voltage, including lightning surges, switching operations and faults. Those waves then propagate in both directions with a high velocity.

This chapter focuses on the analysis of TWs in transmission lines. An overview of TWs is first proposed. The mathematics behind them are then developed, starting from the general equations describing the behaviour of the transmission lines: the Telegrapher's equations. The practical ways of measuring travelling waves are then discussed.

1.1 Overview

TWs are the propagation of EM transients inside the transmission line [2–5, 35]. They are called as such because they contain equal parts electric and magnetic energy. They are generated whenever a sudden change of voltage occurs on the transmission line. These changes of voltage frequently occur, whenever switching operations are performed by the system operator, or whenever a lightning surge or a fault occurs. The TWs generated will then propagate in both directions in a two direction model (Figure 1.1). The frequency content of a travelling wave can reach the MHz [13, 35, 36].

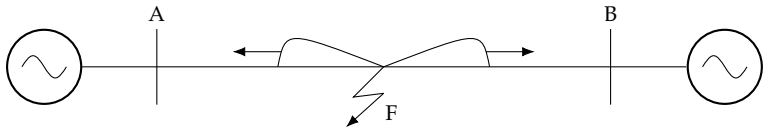

FIGURE 1.1: TWs are the propagation of EM transients generated when a sudden change of voltage occurs (a fault in this figure) [2].

When voltage waves propagate, an associated current wave propagates with the same speed. The ratio between the voltage and current waves is called the characteristic impedance Z_c, also named surge impedance. The travelling waves have a high propagation speed v in overhead lines, typically close to the speed of light [6].

In theory, the characteristic impedance and propagation speed are variable. Because the losses in overhead lines are small, an assumption frequently made is to neglect them. This allows us to consider v and Z_c as constant for a particular line. Furthermore, if the geometry and material properties of a line are known, the value of v and Z_c can be computed [2].

While the TWs propagate in the transmission lines, their amplitude will decrease. This is called attenuation, and is caused by the losses in the line. During the propagation, the shape of the waves will change. This is called distortion.

Whenever the waves reach a point of discontinuity, reflection occurs. A point of discontinuity is any point in the system where there is a change of characteristic impedance. When reflection occurs, part of the initial wave is transmitted, and part of it is reflected. The ratio with which they are transmitted and reflected can be computed based on the characteristic impedances on both sides.

1.2 Transmission lines

Theoretical analysis must be based on models that describe real phenomena with sufficient accuracy. Transmission line models can be used to study the behaviour of currents and voltages in it. They can be modelled with different level of complexity, depending on the application.

The transmission line is usually modelled as a 4 terminal system, which is correct for single-phase systems. Because the transmission lines are actually composed of three interdependent phases, a modal transformation must be applied to obtain three independent modes, which can then be modelled and analysed as three independent 4-terminal transmission lines.

Transmission line models can be separated in two major groups: lumped element models and distributed parameters models.

1.2.1 Lumped element models

In lumped element models, the behaviour of the transmission line is described using a set of discrete entities. The most commonly used lumped element model is the Pi-model (Figure 1.2), where the total inductance of the line L represents the magnetic field, the capacitance C represents the electric field, the resistance R the losses in the line and the conductance G the losses in the di-electric medium [37].

Lumped element models are suitable and typically used for steady state studies, when the power frequency is a constant 50 or 60 Hz. However, they do not take in consideration the propagation time inside the line. As such, they are not suitable for the studies of high frequency transients, where this propagation time is important [2, 17, 35, 38].

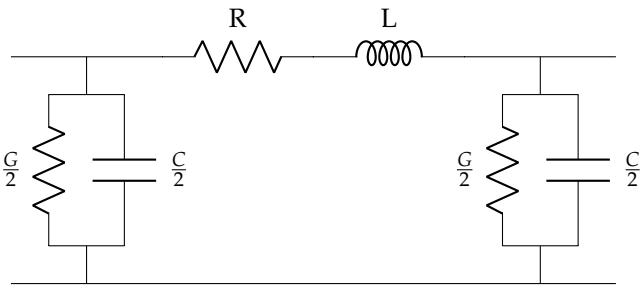

FIGURE 1.2: Lumped element model of a transmission line (pi-model).

1.2.2 Distributed parameter models

In distributed models, the parameters of the line (L, C, R, G) are equally distributed along the line. In this case, we are not talking about a total value of each parameters, but of their lineic value (a value per unit length). Figure 1.3 displays a line segment Δx of a distributed parameter transmission line model. Distributed element models are necessary for frequencies where the propagation time inside the line is relevant.

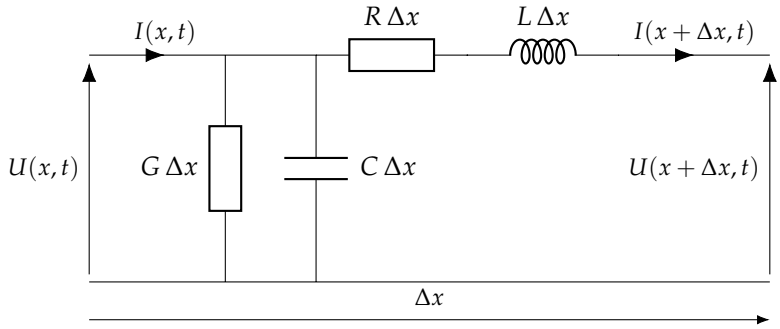

FIGURE 1.3: Distributed model of a differential-length line segment Δx of a transmission line in the time domain [38].

Distributed transmission line models are classified in two groups: constant parameters or frequency dependent parameters models. In real transmission lines, the parameters are not constant with the frequency [2, 35, 37, 38](see section 1.2.4). When these variations are not significant for a given problem, constant parameters models are used; the parameters are considered constant in the whole frequency range. When these variations are significant, frequency dependent models are used.

1.2.3 Modal analysis

Transmission lines are three-phased. Due to the EM coupling between those phases, they cannot be considered independently. This complicates their analysis, as the two-conductor models presented cannot be used as is. A modal analysis is used to decompose a group of coupled equations into decoupled equations, which can be analysed independently. In this work, Clark's transformation matrix was used for the modal decomposition [39] :

$$\begin{bmatrix} V_\alpha \\ V_\beta \\ V_0 \end{bmatrix} = T \cdot \begin{bmatrix} V_A \\ V_B \\ V_C \end{bmatrix} \tag{1.1}$$

$$\begin{bmatrix} I_\alpha \\ I_\beta \\ I_0 \end{bmatrix} = T \cdot \begin{bmatrix} I_A \\ I_B \\ I_C \end{bmatrix} \tag{1.2}$$

With:

$$T = \frac{1}{3} \cdot \begin{bmatrix} 2 & -1 & -1 \\ 0 & \sqrt{3} & -\sqrt{3} \\ 1 & 1 & 1 \end{bmatrix} \tag{1.3}$$

The Clark matrix transform is not a full modal transformation. It transforms the three-phase voltages and currents into three modal voltages and three modal currents. Two of those are aerial modes (alpha, beta) and one of them is a ground mode (zero).

Sometimes, parallel overhead lines are used. These parallel lines consist in multiple 3-phase systems put in parallel. Depending on the number of phases, different matrix transforms are used to decompose the system into modal components.

Each of the modes will have their associated parameters. The earth mode propagation speed is significantly slower than the aerial modes. The ground mode is also more sensible to attenuation and distortion than the aerial modes. In this work, as in most TWFL studies [13, 27, 32, 40, 41], only the aerial modes are used. They are faster, which means that the first wave reaching substations are aerial, and their lower distortion makes it easier to detect them.

1.2.4 Line parameters

The parameters of an overhead line can be computed based on the material used, and based on the geometrical disposition of the conductors [42].

Resistance

The DC resistance of a conductor is computed by considering that the current is flowing uniformly over the cross-section area of the conductor. It is evaluated with:

$$R_{dc} = \frac{\rho}{A} \quad [\Omega/m] \tag{1.4}$$

Where

- ρ is the conductor resitivity (Ωm)
- A is the conductor cross-section area (m^2)

When AC current is flowing instead of DC current, skin effect occurs. When the frequency increases, the current tends to go toward the surface of the conductor, reducing the effective cross-section area used by the current. The AC resistance will therefore increase with the frequency. A skin correction factor can be computed at different frequencies by using differential equations and Bessel functions. The skin effect is higher for the zero sequence resistance [42].

Inductance

The total inductance of a conductor consists in an internal inductance and a mutual inductance. These values can be computed and depend only on the line configuration. For example, the phase inductance of a transposed three-phase line is evaluated with:

$$L_{phase} = \frac{\mu_0}{2\pi} \ln\left(\frac{GMD}{GMR_{cond}}\right) \quad [H/m] \tag{1.5}$$

Where:

- $GMD = \sqrt[3]{D_{AB}D_{BC}D_{CA}}$ is the geometrical mean distance for the three phase line.
- $GMR_{cond} = e^{-1/4}r = 0.7788r$ is the geometric mean radius of the conductors

The positive sequence inductance slightly changes due to the skin effect. The zero sequence inductance is more affected by it.

Capacitance

The capacitance can also be computed based on the line configuration. For a three-phase transposed line, the capacitance from one phase to neutral is evaluated with:

$$C_{AE} = \frac{2\pi\varepsilon_0}{\ln\left[\frac{GMD}{r}\right]} \quad [F/m] \tag{1.6}$$

where r is the conductor radius.

Frequency dependence

Figure 1.4 shows the evolution of the resistances and of the inductances evaluated at different frequencies for a particular overhead line (the line and parameters values are available in Appendix B). The ground mode parameters are more affected by the skin effect, and vary more strongly with the frequency [42].

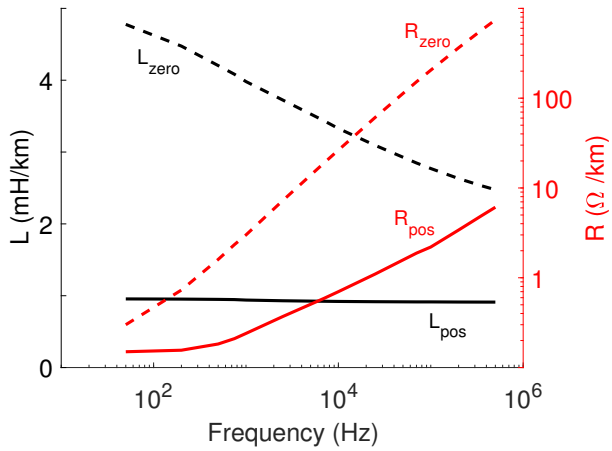

FIGURE 1.4: Parameters of an overhead line evaluated for different frequencies.

1.2.5 Non homogeneous lines

Most transmission lines have constant geometry and material used on their whole length, which leads to constant parameters with regards to the distance. In some situations, a line can consist in different distinct sections, each with their own geometry and associated parameters.

A classic situation is the mixed cable/overhead lines. In these mixed lines, overhead lines are connected to underground cables. They are becoming popular in recent years in some parts of Europe, due to a mix of poor public acceptance of overhead lines, and of economic preference for forested area. Another situation in which a line is non homogeneous is a change of line geometry (using parallel lines or not, changing the conductor material or disposition, etc). An example of this situation can be found in the measurement campaign performed during this work (Chapter 6).

The behaviour of travelling waves in non homogeneous lines is more complex due to the additional reflections occurring on the point of discontinuity, and to the different propagation speed associated with each line sections (Figure 1.5).

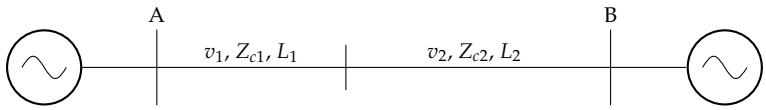

FIGURE 1.5: Non homogeneous lines have distinct sections. Those sections may have different lengths, propagation speed and characteristic impedances.

1.3 Transmission line equations

The transmission line equations for constant distributed parameters models are developed in this section. They describe the behaviour of the voltage and of the current with respect to time t and distance x in the transmission line. They can be developed either in the time domain or in the frequency domain [2, 38, 43, 44].

1.3.1 Time domain

Equations 1.7 and 1.8 are Kirchhoff's laws applied to the distributed model in the time domain (Figure 1.3). Equation (1.7) expresses that the voltage at

the end of the system is equal to the sum of the voltage at the start of the system, and of the voltage drop on the inductance and resistance. Equation (1.8) expresses that the current entering the system is equal to the sum of the current leaving the system, and the currents flowing through the capacitance and leakage conductance.

$$U(x+\Delta x,t) = U(x,t) - L\cdot\Delta x\cdot\frac{\partial I(x+\Delta x,t)}{\partial t} - R\cdot\Delta x\cdot I(x+\Delta x,t) \quad (1.7)$$

$$I(x,t) = I(x+\Delta x,t) + C\cdot\Delta x\cdot\frac{\partial U(x,t)}{\partial t} + G\cdot\Delta x\cdot U(x,t) \quad (1.8)$$

These equations can be re-arranged as:

$$\frac{U(x+\Delta x,t)-U(x,t)}{\Delta x} = -L\cdot\frac{\partial I(x+\Delta x,t)}{\partial t} - R\cdot I(x+\Delta x,t) \quad (1.9)$$

$$\frac{I(x+\Delta x,t)-I(x,t)}{\Delta x} = -C\cdot\frac{\partial U(x,t)}{\partial t} - G\cdot U(x,t) \quad (1.10)$$

The telegraph equations (1.11), (1.12) are obtained when we take the limit as $\Delta x \to 0$:

$$\frac{\partial U(x,t)}{\partial x} = -L\cdot\frac{\partial I(x,t)}{\partial t} - R\cdot I(x,t) \quad (1.11)$$

$$\frac{\partial I(x,t)}{\partial x} = -C\cdot\frac{\partial U(x,t)}{\partial t} - G\cdot U(x,t) \quad (1.12)$$

These equations describe the behaviour of the current and of the voltage inside a generic line. They do not have an analytical closed-form solution in the time domain, except in some special cases such as the lossless line or when the Heaviside condition is respected ($\frac{G}{C} = \frac{R}{L}$).

1.3.2 Frequency domain

The current and voltage properties of the system can also be analysed in the frequency domain, and be converted in the time-domain afterwards. Figure 1.6 shows the representation of a distributed model in the frequency domain. Using Kirchhoff's law in the frequency domain gives:

$$\boldsymbol{U}(x+\Delta x) = \boldsymbol{U}(x) + \boldsymbol{z}\cdot\Delta x\cdot\boldsymbol{I}(x) \quad (1.13)$$

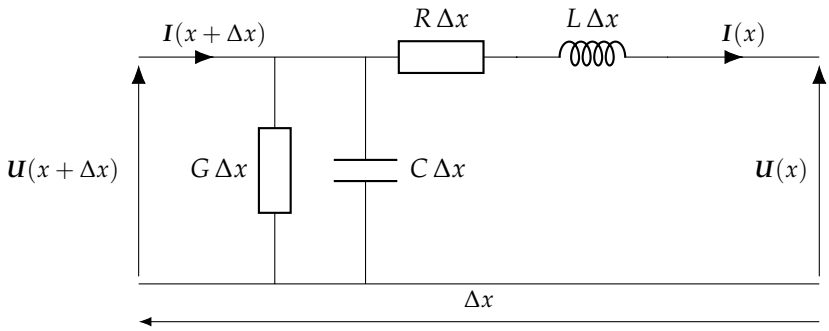

FIGURE 1.6: Distributed model of a differential-length line segment Δx of a transmission line in the frequency domain.

$$\boldsymbol{I}(x+\Delta x) = \boldsymbol{I}(x) + \boldsymbol{y}\cdot\Delta x\cdot\boldsymbol{U}(x+\Delta x) \tag{1.14}$$

with $\boldsymbol{z} = R + j\omega L$ the impedance of the series elements, and $\boldsymbol{y} = G + j\omega C$ the admittance of the shunt elements. Those equations can be re-arranged as:

$$\frac{\boldsymbol{U}(x+\Delta x) - \boldsymbol{U}(x)}{\Delta x} = \boldsymbol{z}\cdot\boldsymbol{I}(x) \tag{1.15}$$

$$\frac{\boldsymbol{I}(x+\Delta x) - \boldsymbol{I}(x)}{\Delta x} = \boldsymbol{y}\cdot\boldsymbol{U}(x+\Delta x) \tag{1.16}$$

We can take the limit as $\Delta x \to 0$ to obtain the equivalent of the Telegraph equations in the frequency domain:

$$\frac{d\boldsymbol{U}(x)}{dx} = \boldsymbol{z}\cdot\boldsymbol{I}(x) \tag{1.17}$$

$$\frac{d\boldsymbol{I}(x)}{dx} = \boldsymbol{y}\cdot\boldsymbol{U}(x) \tag{1.18}$$

If we differentiate those equations with respect to x, and substitute with (1.15) and (1.16) we obtain a pair of homogeneous differential equations:

$$\frac{d^2\boldsymbol{U}(x)}{dx^2} - \boldsymbol{z}\cdot\boldsymbol{y}\cdot\boldsymbol{U}(x) = 0 \tag{1.19}$$

$$\frac{d^2\boldsymbol{I}(x)}{dx^2} - \boldsymbol{z}\cdot\boldsymbol{y}\cdot\boldsymbol{I}(x) = 0 \tag{1.20}$$

Those are well known systems of equations. Using boundary conditions, they can be solved in the frequency domain. The boundary conditions for our

problem are set at the sending end: $x = 0, \boldsymbol{U}(0) = U_s, \boldsymbol{I}(0) = I_s$. The solution of this system gives us the transmission line equations in the frequency domain:

$$\boldsymbol{U}(x) = \frac{1}{2}(U_s + I_s \cdot \boldsymbol{Z_c})e^{\gamma x} + \frac{1}{2}(U_s - I_s \cdot \boldsymbol{Z_c})e^{-\gamma x} \tag{1.21}$$

$$\boldsymbol{I}(x) = \frac{1}{2\boldsymbol{Z_c}}(U_s + I_s \cdot \boldsymbol{Z_c})e^{\gamma x} + \frac{1}{2\boldsymbol{Z_c}}(U_s - I_s \cdot \boldsymbol{Z_c})e^{-\gamma x} \tag{1.22}$$

Two important parameters appear in those equations: Z_c the characteristic impedance, and γ the propagation constant:

$$\boldsymbol{Z_c} = \sqrt{\frac{\boldsymbol{z}}{\boldsymbol{y}}} = \sqrt{\frac{R + j\omega L}{G + j\omega C}} \tag{1.23}$$

$$\gamma = \sqrt{\boldsymbol{z}\boldsymbol{y}} = \sqrt{(R + j\omega L)(G + j\omega C)} \tag{1.24}$$

The characteristic impedance represents the ratio between the voltage and current waves, and will be further developed in Section 1.4. The propagation constant includes information on the propagation velocity, the attenuation and the distortion of the wave. It is further developed in section 1.6. It should be noted that the common name of propagation constant is misleading, as it varies with the frequency, as seen with the presence of ω in the expression.

1.4 The lossless line

The Telegraph equations for general transmission lines (1.11), (1.12) do not have an analytical general solution [2, 44]. An assumption frequently made to continue the analytical analysis is to assume a lossless line. The equations are then simplified, which allows a better understanding of the TW theory, as well as the development of simplified expressions of the TW parameters. Those simplified expression can be used in practice, for example for lines where the losses are not significant or at the start of a phenomenon when the losses are not important.

The analysis in this section will be performed using the following assumptions for the transmission line:

- 4 terminal constant distributed parameters model (Figure 1.3)
- Losses neglected (R = G = 0)

1.4.1 Propagation speed

The propagation speed inside the lossless line can be derived from the expression of the current (1.25) and of the electromagnetic force (1.28) around a line segment Δx of the transmission line (Figure 1.3) [2].

$$I = \frac{dQ}{dt} \tag{1.25}$$

$$Q = CV \tag{1.26}$$

$$I = lim_{\Delta x \to 0} \frac{\Delta Q}{\Delta t} = lim_{\Delta x \to 0} \frac{CU\Delta x}{\Delta t} = CU\frac{dx}{dt} = CUv \tag{1.27}$$

Where:

- Q is the number of charges present on the line section
- C is the lineic capacitance
- U is the voltage applied to the line

Starting when the transient enters the line until when the waves reach the distance Δx, after a time Δt, there will be ΔQ charges on the line charging the capacitance.

$$Emf = \frac{d\phi}{dt} \tag{1.28}$$

$$\Delta\phi = L\Delta x I \tag{1.29}$$

$$Emf = lim_{\Delta x \to 0} \frac{\Delta\phi}{\Delta t} = LCU\Big(\frac{dx}{dt}\Big)^2 = LCUv^2 \tag{1.30}$$

Where:

- Emf is the electromagnetic force applied to the system
- ϕ is the magnetic flux

We use the expression of the current previously found (1.27), Faraday's law (1.28) and the definition of an inductance (1.29). Because there is no discontinuity in the system, the emf must be equal to the voltage applied to the system, U. This gives us the expression of the propagation velocity (1.31).

$$v = \frac{1}{\sqrt{LC}} \tag{1.31}$$

It results from this analysis that the propagation speed depends only on the parameters of the line, L and C. Those parameters in turn depend only on the geometry of the line and can be computed for a specific line (see Section 1.2.4).

For overhead lines, the propagation speed is close to the speed of light. For underground cables, the speed is significantly lower (typically 2 to 3 times lower depending on the geometry).

1.4.2 Characteristic impedance

By combining (1.27) and (1.31), we obtain the expression of the characteristic impedance Z_c. The characteristic impedance is the ratio of the voltage wave over the current wave.

$$Z_c = \sqrt{\frac{L}{C}} = \frac{U}{I} \tag{1.32}$$

For lossless lines, the characteristic impedance is also constant and depends only on the geometry of the line.

1.4.3 General solution

For a lossless transmission line, (1.33) and (1.34) simplify to:

$$\frac{\partial U(x,t)}{\partial x} = -L \cdot \frac{\partial I(x,t)}{\partial t} \tag{1.33}$$

$$\frac{\partial I(x,t)}{\partial x} = -C \cdot \frac{\partial U(x,t)}{\partial t} \tag{1.34}$$

Applying Taylor's series to the general solution of this set of differential equation results in the expression for the voltage and current waves in the time domain [2]:

$$U(x,t) = f_1(t + \frac{x}{v}) + f_2(t - \frac{x}{v}) \tag{1.35}$$

$$I(x,t) = -\frac{1}{Z_c}\Big[f_1(t + \frac{x}{v}) - f_2(t - \frac{x}{v})\Big] \tag{1.36}$$

This expression describes that at any point in the system, the value of the voltage and of the current is a combination of a forward travelling wave f_2 and of a backward travelling wave f_1 (Figure 1.7).

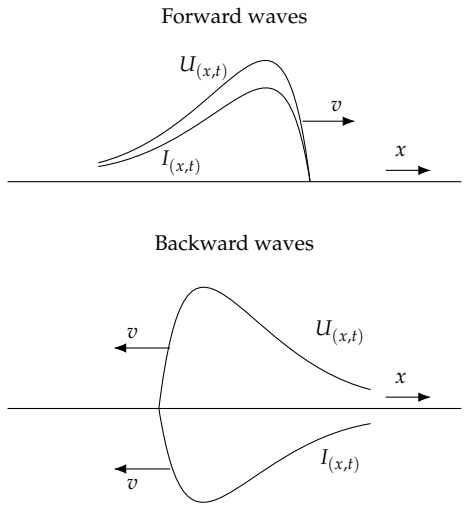

FIGURE 1.7: Forward and backward travelling waves [2].

1.5 Reflections

We saw that there is a fixed ratio between the voltage and the current waves, the characteristic impedance Z_c. When a wave reaches a point in the system where there is a change of characteristic impedance (called point of discontinuity), reflections occur so that this proportionality is not violated. New waves are generated: the reflected waves travel back, and the transmitted waves continue through the point of discontinuity. With this reflection process, energy conservation is satisfied and the voltages and currents at the point of discontinuity are themselves continuous.

1.5.1 Reflections on line junctions

Let us consider the junction between a line of characteristic impedance Z_A and another line of characteristic impedance Z_B. At the point of discontinuity x_0, part of the incident waves (V_1, I_1) will be reflected (V_2, I_2), and part of it will be transmitted (V_3, I_3). The ratio of the incident wave that is reflected and

transmitted can be computed based on the characteristic impedances. They are expressed as [3]:

$$I_2 = \left(\frac{Z_A - Z_B}{Z_A + Z_B}\right) I_1 \tag{1.37}$$

$$U_2 = \left(\frac{Z_B - Z_A}{Z_A + Z_B}\right) U_1 \tag{1.38}$$

$$I_3 = \left(\frac{2Z_A}{Z_A + Z_B}\right) I_1 \tag{1.39}$$

$$U_3 = \left(\frac{2Z_B}{Z_A + Z_B}\right) U_1 \tag{1.40}$$

When taking measurements at points of discontinuity, the measured wave corresponds to the sum of the incident and reflected wave, which is the transmitted wave.

The equations presented are valid at the junctions of two lines with different characteristic impedances. They can be generalized for any point where the line divides into N different lines of characteristic impedance Z_i [3]:

$$I_{3B} = \frac{U_{3B}}{Z_B}, \quad I_{3C} = \frac{U_{3C}}{Z_C}, ..., I_{3N} = \frac{U_{3N}}{Z_N} \tag{1.41}$$

$$I_{2A} = -\frac{U_{2A}}{Z_A} \tag{1.42}$$

$$U_{1A} + U_{2A} = U_{3B} = U_{3C} = ... = U_{3N} \tag{1.43}$$

$$I_{1A} + I_{2A} = I_{3B} + I_{3C} + ... + I_{3N} \tag{1.44}$$

Fig. 1.8 shows an example for $n = 3$.

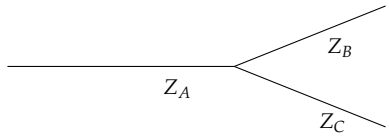

FIGURE 1.8: The wave arriving at a T-junction will see a change of characteristic impedance [3].

1.5.2 Reflections on line terminations

The second type of discontinuity on which TWs will be reflected is the line termination. The impedance of the termination can range anywhere from the short-circuit to the open circuit. Those two extreme cases are illustrated in this section. A third example is provided, in which the line termination is not resistive [3].

Short circuit

The transmitted voltage wave for a short circuit must always be equal to zero (by property of the short circuit). This might be verified using (1.40) with $Z_B = 0$. The energy content of the initial wave was equally divided between electrical and magnetic energy. Since the transmitted voltage wave was cancelled, all the electric energy content of the travelling wave disappeared. It has been converted into magnetic energy in the form of the current wave, which has been doubled (equation 1.39).

$$U_3 = 0, \quad I_3 = 2 \cdot I_1 \tag{1.45}$$

Open circuit

By property of the open circuit, the transmitted current must be equal to zero. Using (1.39) and (1.40), we see that the voltage wave is then doubled.

$$U_3 = 2 \cdot U_1, \quad I_3 = 0 \tag{1.46}$$

Pure inductance

For the general case of a line terminated in an impedance Z_{end}, equations 1.37 - 1.40 must be analysed using Laplace transforms. The voltage and current profiles across the termination impedance can then be found. Figure 1.9 displays the results for a wave reaching a pure inductance.

The inductance is first seen as an open circuit for the wave (voltage wave doubled, current wave cancelled), progressing exponentially into a short-circuit (voltage wave cancelled, current wave doubled). The time constant of the exponential progression depends on the inductance value and on the characteristic impedance of the incident line.

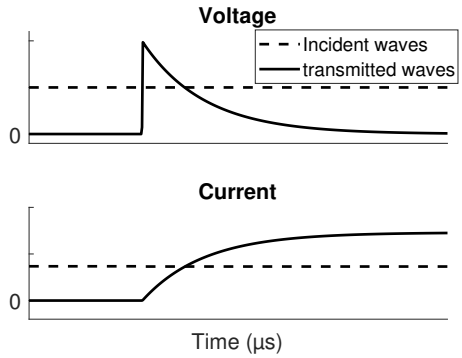

FIGURE 1.9: Voltages and currents transmitted at an inductive line termination.

1.5.3 Lattice diagram

Reflections on the network happen on a lot of elements: line junctions, bus bars, fault points, etc. To keep track of the reflections, the lattice diagram has been developed by Bewley [5].

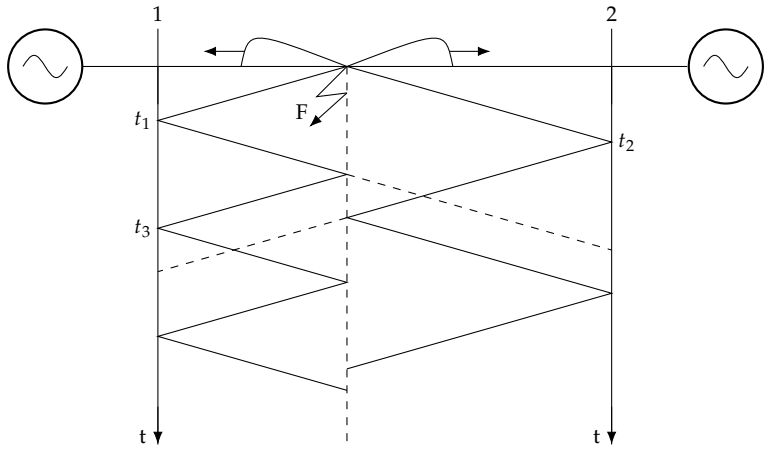

FIGURE 1.10: Lattice diagram build for a lightning stroke occurring on an overhead line. Reflections occur on fault point and on both substations.

Figure 1.10 shows a lattice diagram build for a lightning stroke occurring on an overhead line. The paths of each reflections are easily followed on the zig-zag lines. Sometimes the amplitudes of the waves are of interest. In those cases, the reflection coefficients are computed and displayed at each

reflection point. The waves amplitude of each reflection is then computable with a simple multiplication.

1.6 Attenuation and distortion

When the losses are included, the mathematical analysis and the behaviour of TWs become much more complex. This section does not provide the full mathematical description of this complex case, but rather provides a qualitative analysis of the impact of the losses on TWs.

The presence of resistance in the line means that losses occur whenever a current flows in the line, and the presence of the leakage conductance means that losses occur when a voltage is established between the conductors. Those losses occur at the expense of the travelling waves. The waves are reduced in magnitude, or attenuated, as they progress along the line [3].

In practical cases, attenuation is accompanied by distortion of the waves. The shape of the waves changes and become more elongated. This is caused by the fact that the electric losses and the magnetic losses inside the line are not equal. The attenuation suffered by the voltage and current waves are not proportional. To conserve the energy, new waves are initiated. This is the same situation as the reflections that are generated at point of discontinuity, seen in section (1.5). A continuous process of energy reflection is taking place at each point on the line as it is encountered by the wavefront [3]. The consequence is that waves change their shape as they travel and suffer attenuation.

In a particular case, the electric losses are equal to the magnetic losses, and the waves suffer no distortion while propagating. It can be demonstrated that this is the case when the Heaviside conditions are satisfied, in which case we are talking about a distortionless line [2]:

$$\frac{R}{L} = \frac{G}{C} \tag{1.47}$$

In addition to the attenuation and distortion caused by the losses in the line, we must remember that the line parameters change with the frequency. This means that, even for a lossless or distortion-less line, the propagation velocity and the attenuation factor vary with the frequency. Figure 1.11 shows the variation of the propagation velocity and of the attenuation with the frequency. The aerial mode velocity is faster than the ground mode velocity, and vary less with the frequency.

Travelling waves contain a spectrum of frequencies, each of which will travel at a different speed. The consequence of this is also that their shape will change while propagating. This is more pronounced for the ground modes.

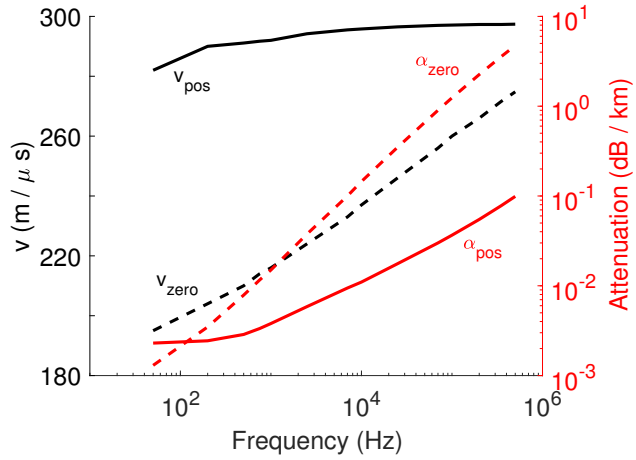

FIGURE 1.11: The propagation velocity and the attenuation constant change with the frequency.

1.7 The impact of substation measurement

There are currently no practical ways to record the travelling waves flowing in the transmission lines without going through a transducer first, such as a measurement transformer (MT). Those MTs decrease the voltage and current to acceptable levels for practical measurements inside the substation.

1.7.1 Transformers bandwidth

MTs are designed to perform at power frequency, where they provide an accurate representation of the transmission line currents and voltages. For very high frequencies, such as in TWs, the reduced signals will not be an exact representation of the signals flowing inside the line.

The effect of the MTs at very high frequencies is not extensively covered in the literature. Most research on TWs consider that current transformers (CTs) have a sufficiently good bandwidth to record TWs, but that voltage transformers (VTs) have a more limited bandwidth.

Actual studies to find the transformer bandwidths are however hard to come by. The studies made on current transformers found a good bandwidth

until at least $100kHz$ [20–23] and sometimes up to 500kHz [13]. For this reason, many algorithms based on travelling waves preferably make use of the current measurements [6, 13, 20, 21, 29, 31].

1.7.2 Secondary cable ringing

If the CTs themselves have a good bandwidth and do not affect the measurement of current TWs, a phenomenon called secondary cable ringing significantly changes the shape of the waves recorded [13, 23].

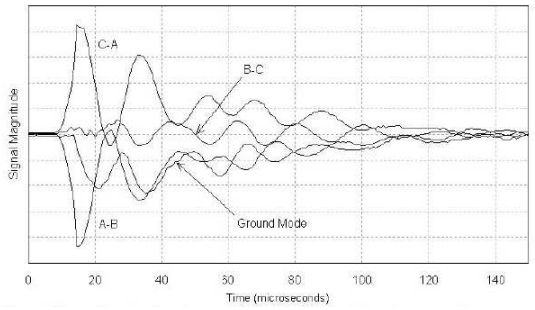

FIGURE 1.12: Fast reflections observed on the currents recorded during the energizing of a line [23]

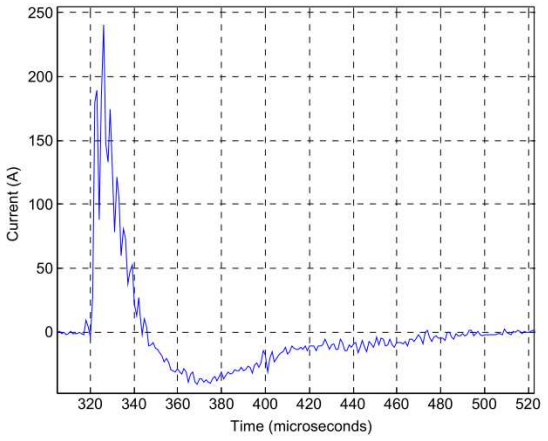

FIGURE 1.13: Fast reflections observed on the currents recorded during a fault in the power system [13]

The CTs are connected to the transmission line. On the secondary side of those transformers, cables are connected to transmit those signals inside the substations, in which the measurements are actually taken. Those cables

typically range from a few tens of meters, to a couple hundreds of meters in a few extreme cases.

One end of the cable is connected to the CT, which will act as an open circuit for the wave reflections. The other end of the cable is connected to the measurement devices, which have a low impedance. The consequence of this is that very fast reflections occur in those short cables. Two examples were found and are shown on Figures 1.12 and 1.13.

The fast reflections that occur at the secondary side of CTs alter the shape of current waves recorded. This can affect the performance of algorithms based on the recorded current waves.

Chapter 2

Simulation tools

The most convenient way to study a problem, and to test algorithms for different cases, is the use of simulation tools. Without them, algorithms must be tested exclusively on real situations. This might be a more or less complex task, depending on the problem. For TW FL studies in particular, acquiring suitable fault records is not an easy task, and will be the subject of Chapter 6.

Simulation tools are based on theoretical models, which mathematically represent what occurs in reality with a certain accuracy. In order to be useful, they must provide a good representation of the phenomena of interest. They can be validated by comparing their results with field records.

This chapter covers the literature review of power system models for fast transients. The simulation models are implemented on EMTP (Electro-Mechanical transient program) [45]. EMTP is a software that was specifically developed to study the transients in power systems. A free license, ATP-EMTP is available and includes a graphical interface with ATPDraw [46].

The existing models for the different power system elements are first presented, and their accuracy for TW studies is discussed. The models presented are then implemented to illustrate the theory of Chapter 1.

The overhead lines models are well-developed and generally accepted as providing a good representation of actual overhead lines. They take into account the propagation velocity depending on the line geometry, and the attenuation and distortion of the waves during propagation. The wave characteristics of different lines based on their geometry is analysed. There is currently no consensus on high frequency models for other elements of the system, such as the towers, the substation busbars, the fault inception and the transformers.

It comes out from this analysis that the propagation of transients in overhead lines is sufficiently well modelled for TWs analysis. The simulation tools do not provide a reliable way to model the inception of the fault and all the reflections that can occur in the network (towers, busbars, etc), or the effect of the measurement substations on the TWs recorded.

The simulation tools will be improved by adding the effect of those substation measurements based on laboratory tests and substation measurements on Chapter 7.

2.1 Power system model

Different models are available for each element of the power system. One element might be modelled differently, depending on the topic of interest. In particular, the low frequency models focus on having a good accuracy for the power frequency, while high frequency models focus on having a good accuracy for the fast transients. This last case is of interest in our TW FL study. This section covers the state of the art of the high frequency models for the different elements of the power system.

2.1.1 Overhead lines

We presented in section 1.2 the different line models. Distributed line models are required to study fast transients applications. Overhead lines are generally modelled using Bergeron models or J-Marti models, depending on the application.

Bergeron model

The Bergeron model is a constant distributed parameters model. In this model, the losses in the line are neglected ($R = G = 0$) and are taken into account as lumped element located at both ends and in the middle of the line.

This model does not take into account attenuation and distortion due to the constant parameters and to the neglected losses. This model is therefore suitable for situations where the attenuation and distortion of the waves are not important (namely when the length of the line is very short, or for telecommunication applications where distortionless lines are used [47]).

J-Marti model

The J-Marti model is a distributed parameter model which takes into account the frequency-dependence of the parameters [18]. The characteristic impedance and the propagation constant are approximated by rational functions of the frequency.

This model takes into account the attenuation and distortion of waves. The numerical computation method for the line parameters introduces some error in the earth return, which is not significant for overhead lines [48]. This model is considered as the most suitable for fast transients studies in overhead lines [17, 40, 48, 49].

LCC routine

EMTP allows an easy implementation of line models based on their geometry with the LCC routine (Lines and Cables Constants) [45, 46]. This routine computes the line parameters based on the line geometry introduced in the software, as detailed in Section 1.2.4.

In Bergeron models, the parameters are computed at a specified frequency, and are assumed constant on the whole frequency range. In J-Marti models, the parameters are computed over a frequency range specified by the user.

2.1.2 Measurement transformers

MTs are designed to perform at power frequencies. As such, the vast majorities of the studies on MTs, and the models available, are suitable for low frequencies. For TWs, an analysis up to a few 100s of kHz is needed.

Due to the bad bandwidth of VTs, TW algorithms are typically based on current waves only, and the VTs are then not modelled [6].

Few research has been performed to model CTs for high frequencies, especially when including the effect of the secondary cables (see Section 1.7). In most TWFL work, the effect of the CT is neglected [25, 26, 28, 29, 32, 36]. A few studies include either lumped element CT model, or blackbox models for the CT [22, 27, 40, 50].

Only two papers discussing the modelling of secondary cable ringing were found, showing an improved fitting with the field records when this effect is modelled [13, 23]. In [13], the model is not discussed. In [23], each element is modelled separately: the CT, the secondary cables and the termination burden caused by the substation devices.

Based on the literature and on the fault records presented in Section 6, it appears clearly that the secondary cables connected to the CT significantly affects the shape of the current waves recorded. This effect is investigated and implemented in simulation tools on Chapters 5, 6 and 7.

2.1.3 Neglected effects

The following effects are usually neglected or simplified when studying TW FLs. These effects are studied in fields other than TW FL, and could be investigated and implemented for a more complete power system model. These effects were not shown to noticeably affect the signals in the measurement campaign performed on Chapter 6. The investigation and improvement of those elements were left out of the scope of this work. The studies previously referenced also neglect those elements, with a few exceptions that will be discussed in this section.

Fault inception

When lightning hits an overhead line, the behaviour of the over-voltage generated is well understood, and generally modelled using standard lightning impulse (see Section 5.1). This over-voltage might generate a breakdown of the insulator. This breakdown is usually modelled as an instantaneous switch connected to a constant resistance. This representation of the fault assumes that the arc is generated instantaneously, and has a constant resistance over time. In [36] and [50], the lightning surge is modelled as a Heidler function, and the insulator breakdown with a flashover model.

Towers

The overhead lines are mechanically supported every few hundreds of meters with the help of metallic towers. The lines are isolated from the towers with insulators. In the perfect case, the signals in the lines are then not affected by the towers. In simplified overhead lines models, the towers are therefore neglected and simply not represented. Some papers such as [49] specifically study the insulators breakdown. In this case, the towers modelling is important to the model accuracy.

Substations

In most substations, multiple elements are connected to the line of interest. All the lines reaching these substations are connected to one or more bus bars. The lines may also be connected to other elements in those substations. They can for example be connected to power transformers to change their voltage level, or to capacitor banks or shunt reactors to modify the reactive power generation or consumptions.

All these elements introduce points of discontinuity. Reflections will occur due to these discontinuities. When multiple lines are connected to the substations, the reflections are usually modelled using the different line models connected to that substation, or using a Thevenin equivalent resistance. In [36], the Power transformers are modelled as a high lumped resistance of $100k\Omega$. [13] takes into account the capacitance of each substation element such as the bus system, the generators and the transformers.

2.2 Illustration of TWs properties

2.2.1 Wave propagation and reflection

The propagation of TWs on a short cable, and their reflections on lumped elements, is modelled and illustrated using a Bergeron model. The simulation results are compared with a laboratory experiment.

Simulation model

A DC source is instantaneously connected with a switch to a cable, on which the generated waves will propagate. The cable is modelled as a Bergeron model. The attenuation and distortion on the cable are neglected.

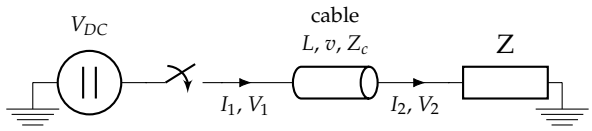

FIGURE 2.1: Simulation model used to illustrate wave propagation and reflections.

Element	Value
V_{DC}	50V
L	1km
v	300 m/ μs
Z_c	50 Ω

TABLE 2.1: Simulation model parameters.

The reflection factors at the end of the cable are illustrated for different values of the end impedance Z on Figure 2.2. With an open circuit, no current waves are recorded at the end of the cable. With a short-circuit, no voltage waves are recorded.

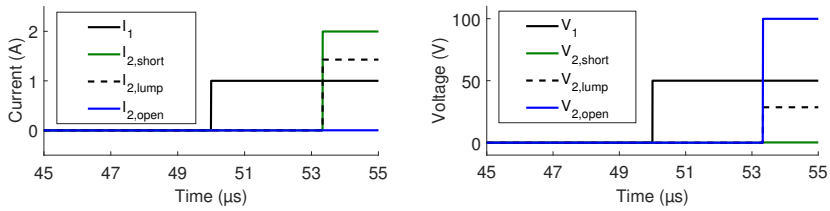

FIGURE 2.2: Simulation results. The reflection factors change with the value of the end impedance Z.

Experimental set-up

A propagation test is performed in a laboratory environment and recreated in EMTP in order to illustrate the differences that may occur between an experiment and simplified models. The situation modelled on EMTP (Figure 2.1) is recreated in a lab, with the components of Table 2.2.

Three difficulties arose when applying the propagation test experimentally: the EM noise, the impact of the measurements, and the stray inductance of the end impedance Z. The impact of the measurement and of the stray inductance were added to the simulation model (See Appendix B for

Element	Value
DC source	24 V battery
Cable	100 m coaxial cable
Propagation speed	258 m/μs
Z_c	75 Ω
Z	20 Ω
Switch	DC/DC converter
Measurement tools	See Appendix C

TABLE 2.2: Propagation lab test: components.

the model description). Figure 2.3 compares the results from the laboratory test and from the simulation.

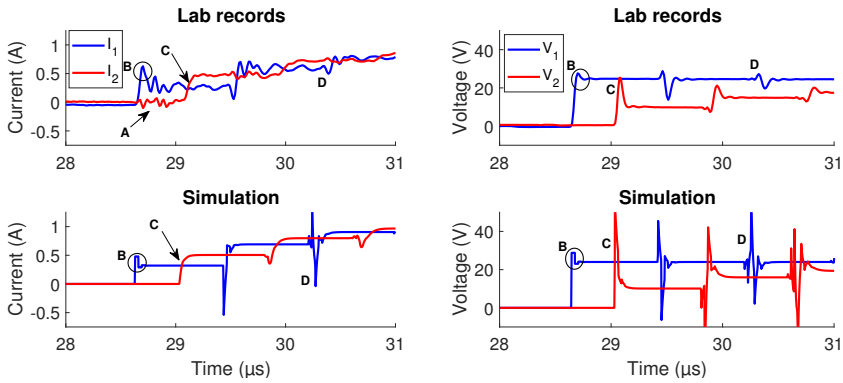

FIGURE 2.3: Currents and voltages recorded and simulated. A: EM noise, B: Reflections caused by the measurement cable, C: Effect of the stray inductance of the resistance, D: Different attenuation factors between simulations and experiment.

The EM noise affects the current recorded by the Rogowski coils (A on the Figure). This affects both I_1 and I_2, and explains why some disturbance is observed on I_2 as soon as the experiment starts, before the wave has propagated to the end of the cables.

A short 3m cable was needed to record the voltage V_1. This short cable generates small wave reflections (B on the Figure).

The end resistance Z used in the experiment contains a stray inductance. This stray inductance affects the reflection factors, as described in section 1.5.2 (C in the Figure).

The main difference between the lab records and the simulation results is that the very high frequencies (introduced by the 3m measurement cable and

by the stray inductance of the end impedance) are quickly attenuated during the propagation in the coaxial cable during the experiment (D in the Figure).

2.2.2 Attenuation and distortion

A typical overhead line is modelled with a J-marti model, using the LCC routine based on [51]. This model takes into account the frequency dependence of the parameters, which leads to attenuation and distortion of the travelling waves while they propagate. Figure 2.4 shows the incident wave, and the wave after 5 and 25km of propagation. The line data is available in Appendix B.

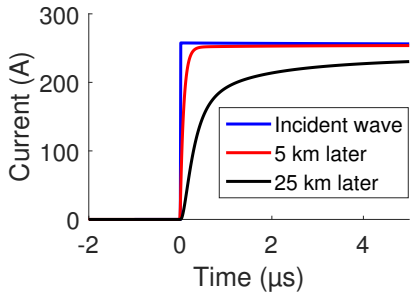

FIGURE 2.4: Attenuation and distortion of a current wave simulated using J-marti model.

2.2.3 Typical propagation speed in overhead lines

The propagation speed in overhead lines depends only on the geometry of the line and the material properties. The propagation speed for different overhead lines is investigated, and the influence of the geometry on the propagation speed is analysed.

One single line and one parallel line are modelled based on [51]. Their geometry is presented on Appendix B. Their geometries are varied, and the aerial mode propagation speed is computed at $250kHz$ for each geometry, using the LCC routine.

Figure 2.5 displays the variation of the propagation speed with the line geometry. The propagation speed in the single line does not change significantly, even when the geometry is changed. The speed difference stayed in a range of $\pm 0.2\%$.

In parallel lines, the propagation speed is lower due to the added mutual inductance between the lines. The propagation speed is heavily affected by

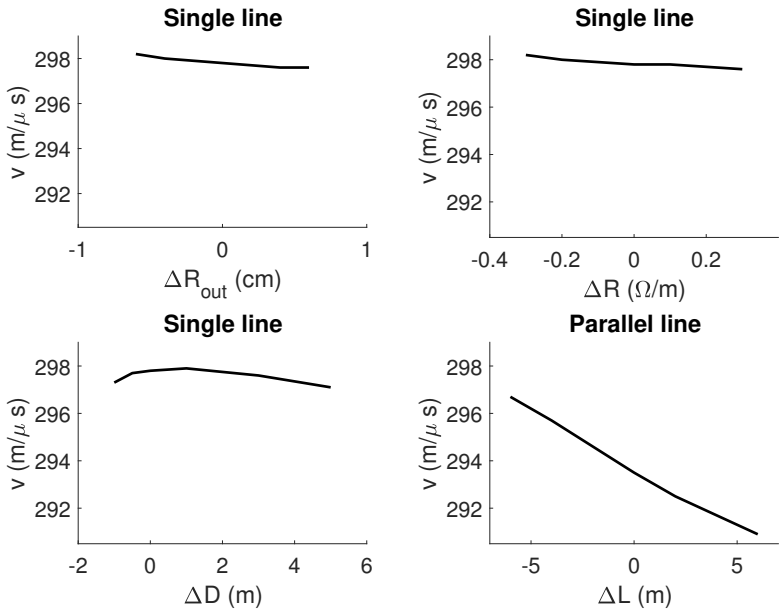

FIGURE 2.5: The geometry of the line affect the propagation in parallel lines more significantly. R_{out}: conductor radius, R: conductor resistivity, D: distance between phases, L: Distance between parallel lines. Data available in Appendix B.

distance between the parallel lines. In this case study, the propagation speed is affected by $\pm 1\%$ when the lines are moved closer or further away by 6m.

2.3 Discussion

Existing models of power systems for TWFL studies focus on overhead lines. In those lines, the propagation of waves are accurately modelled, including the attenuation and distortion that affect the waves. A given overhead line can readily be modelled based on its geometry.

These line models were used to analyse the propagation speed in overhead lines. It came out from this analysis that the propagation speed is lower in parallel lines than in single lines. In addition, the propagation speed in single lines is relatively constant when changing the geometry, while the speed in parallel lines vary more with the distance between the lines.

The most significant oversight in most simulation models are the measurement transducers. They significantly affect the shape of TWs recorded.

Few work that study and model this effect are available .This effect is investigated and implemented in simulation tools on Chapters 5, 6 and 7.

Chapter 3

Algorithms based on travelling waves

The theory of travelling waves can be used for fault location in power systems. The theoretical algorithms have been invented as early as the 1930's and classified in the 1950's based on their operating principle [7]. These operating principles are straightforward. In theory, they offer a better precision compared to impedance fault locators.

The technical challenges associated with the use of those algorithms are more complex, and only recently became economically affordable. TW FL

emerged as an alternative to impedance fault locators, and the basic FL algorithms have already been implemented in some commercialized devices [8–11].

Despite those commercialized devices, experience on such algorithms remains slim. Those algorithms operate very well on simplified simulations, where TWs are clearly observable with no other disturbance from the power system. In practice, there are a few technical challenges. In particular, it is not trivial to precisely measure the arrival times of the waves. A small error made on these measurements leads to a significant error on the fault location. New fault location algorithms based on TWs should be developed with those technical challenges in mind.

In this section, the basic TW FL algorithms are reviewed, and updated for more general cases where the line is non homogeneous. The practical challenges that should be considered when developing algorithms are then described and analysed, and solutions are proposed.

The algorithms and practical considerations presented in this section are used for developing the FL algorithm presented in chapter 4.

3.1 Fault location algorithms

Fault locators based on travelling waves are typically classified in 3 types, based on whether the method is active or passive, and for the passive method, based on whether measurements are taken in one or two substations [6, 7]. Passive methods are based on the measurement of the travelling waves generated during the fault. Active methods are based on the measurement of travelling waves generated by closing a breaker on the transmission line.

It should be noted that type B and C algorithms are similar to type D and E introduced hereunder, but differ in the time synchronization method and in the wave generation method used. They are outdated nowadays [6].

3.1.1 Passive two-ended (Type D)

Type D fault locators are based on measurements at both ends of the line. TWs are generated at the point of fault, and propagate in both directions with a certain propagation speed.

The arrival time of the first incident wave is measured at both ends with a time synchronization (Figure 3.1). The fault location D from substation 1 is computed with:

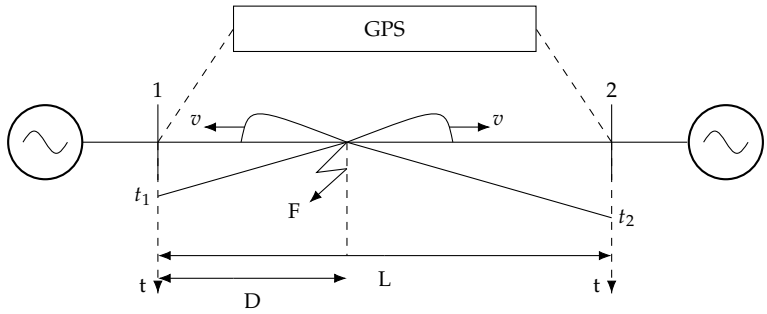

FIGURE 3.1: Type D fault locators are based on the arrival times of the first incident wave in each substation.

$$D = \frac{L + (t_1 - t_2) \cdot v}{2} \, [m] \tag{3.1}$$

Where:

- v is the TW propagation velocity in $m/\mu s$
- L is the line length in m
- t_1 and t_2 are the arrival times of the waves at each end of the line in μs

The advantage of this method is that it does not need to recognize any TW. It is based on the first incident wave arriving in each substation. The drawback is that it requires two measurement devices, and a good time synchronization between them. The precision of the time synchronization affects the fault location precision.

3.1.2 Passive single-end (Type A)

Type A fault locators are based on measurements at one end of the line only. TWs are generated at fault point, and propagate in the line. A reflection process occurs in substation 1, where part of the incident wave is reflected back into the line. A second reflection process then occurs on the fault point, where part of this wave will go back to substation 1.

The arrival time of the first incident wave is recorded at substation 1, as well as the arrival time of the wave reflected on fault point (Figure 3.2). The fault location D from substation 1 is computed with:

$$D = v \cdot \frac{t_3 - t_1}{2} \, [m] \tag{3.2}$$

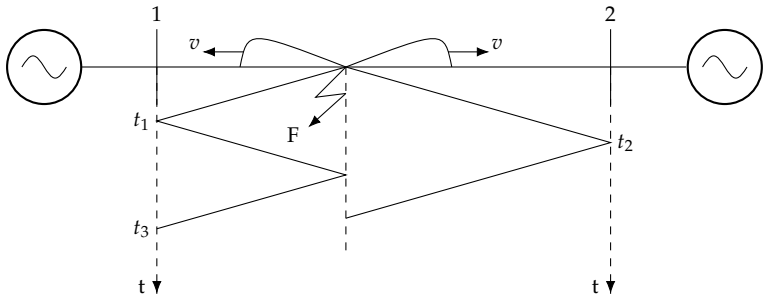

FIGURE 3.2: Type A fault locator are based on the arrival time of the first incident wave, and the first wave reflected at fault point on the same substation.

Where:

- v is the TW propagation velocity in $m/\mu s$
- t_1 is the arrival time of the first wave in substation 1 in μs
- t_3 is the arrival time of the wave reflected on fault point in μs

The advantage of the type A algorithm is that it requires only one measurement device, removing the error due to the time synchronization. The main difficulty with using it is in identifying the correct wave reflection.

The line topology must be suitable to the type A algorithm. Significant reflections must occur on substation 1, so that part of the incident wave is reflected to the fault point. When the substation does not present a significant change in characteristic impedance, these reflections will be either non-existent or too small to be detected.

The algorithm must be able to differentiate the reflections on fault point from all other reflections occurring in the power system. In practice, the waves will be reflected on many elements in the power system. In particular if the fault occurs in the second half of the line, the wave reflected on the second end will reach substation 1 before the first reflection on fault point.

3.1.3 Active single end (Type E)

Type E fault locators are active fault locators. A wave is voluntarily generated after the fault occurred on the line, by switching the breaker of the line. The wave generated in substation 1 propagates on the line and is reflected back

on the fault point (Figure 3.3). The arrival time of this reflection in substation 1 is recorded. The fault location is then evaluated with:

$$D = v \cdot \frac{t_2 - t_1}{2} \tag{3.3}$$

Where:

- t_1 is the generation time of the wave.
- t_2 is the arrival time of the wave reflected on fault point.

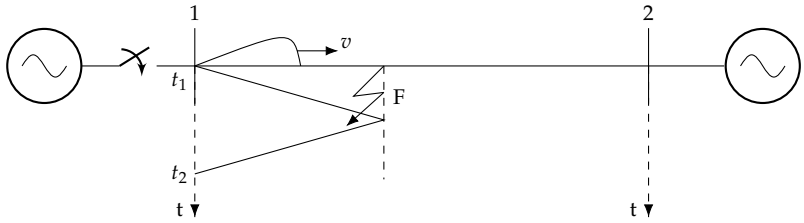

FIGURE 3.3: Type E fault locators are based on the time difference between the wave generated by switching the breaker, and the wave reflected on the fault point.

3.2 Non homogeneous lines

The classical algorithms presented are valid for any line or cable with a constant propagation speed. However, non homogeneous lines (in which the propagation speed is not constant) become more and more frequent. This might be the case for mixed overhead and cable lines, or for overhead lines on which the geometrical disposition changes somewhere in the line. This kind of lines propose a new challenge for the line protection and fault location [41, 52].

Non homogeneous lines can be divided in multiple line sections on which the propagation speed is constant. If the propagation speed in each section does not vary significantly, the speed can be assumed constant with an average propagation speed. The FL algorithms presented previously can be applied as is, introducing a small error due to this assumption.

If the propagation speed in each section differs a lot, a significant error would be made when applying the algorithms as is. In these cases, the algorithms can be updated to take the speed variations into account.

In this section, the type-D algorithm is updated for non homogeneous lines containing two distinct sections. The same development can be applied for lines containing N sections.

3.2.1 Updated type-D algorithm

Figure 3.4 shows a non homogeneous line consisting of two distinct sections. For a fault that occurred in section 1, the propagation times before reaching each substation are:

$$t_1 = \frac{D}{v_1} \tag{3.4}$$

$$t_2 = \frac{L_2}{v_2} + \frac{L_1 - D}{v_1} \tag{3.5}$$

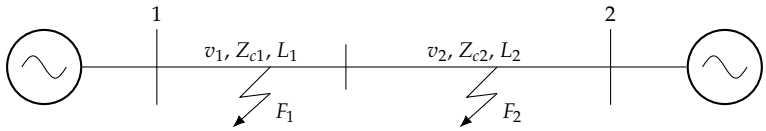

FIGURE 3.4: Non homogeneous lines have distinct sections. Those sections may have different lengths, propagation speed and characteristic impedances.

The recorded difference in arrival time is equal to:

$$\Delta t = t_1 - t_2 = \frac{2D - L_1}{v_1} - \frac{L_2}{v_2} \tag{3.6}$$

With some rearrangements, we obtain the fault location D from substation 1 as a function of Δt:

$$D = \frac{L_1 + v_1 \cdot \Delta t}{2} + \frac{v_1 \cdot L_2}{2v_2} \tag{3.7}$$

If the fault occurred in section 2, the same reasoning can be applied. By symmetry, the fault location D' from substation 2 is equal to:

$$D' = \frac{L_2 - v_2 \cdot \Delta t}{2} + \frac{v_2 \cdot L_1}{2v_1}\,[m] \tag{3.8}$$

The fault location D from substation 1 is then computed with:

$$D = L - D'\,[m] \tag{3.9}$$

$$D = L - \frac{L_2 - v_2 \cdot \Delta t}{2} - \frac{v_2 \cdot L_1}{2v_1} \, [m] \tag{3.10}$$

There is therefore a set of two equations that must be used to find the fault location, depending on the faulted line section. Depending on the recorded Δt and on the line topology, it is possible to determine the faulted line section, as will be shown in the following example.

3.2.2 Example

The line presented in Figure 3.4 is modelled using Bergeron models. The parameters are presented in Table 3.1.

Parameters	Value
L_1	20 km
L_2	30 km
v_1	280 $m/\mu s$
v_2	298 $m/\mu s$

TABLE 3.1: Parameters of the non homogeneous line modelled.

The total propagation time inside the line is equal to

$$\tau = \frac{L_1}{v_1} + \frac{L_2}{v_2} = \tau_1 + \tau_2 = 71.4 + 100.7 = 172.1 \mu s \tag{3.11}$$

where τ_1 is the propagation time in line section 1, and τ_2 is the propagation time in line section 2.

This leads to an average propagation speed of

$$v_{avg} = \frac{L_1 + L_2}{\tau} = 290.53 m/\mu s \tag{3.12}$$

If the fault occurs on the junction between each section, a time difference $\Delta t_{junction}$ will be recorded.

$$\Delta t_{junction} = \tau_1 - \tau_2 = -29.2 \mu s \tag{3.13}$$

If the Δt recorded is larger, the fault occurred in line section 2. If it is smaller, the fault occurred in line section 1. This distinction is needed to know whether equations 3.7) or (3.10) from the updated type-D algorithm will be used.

The results from the classical type D and updated type D algorithms for a 25 km fault are shown in Table 3.2. If the line had been assumed homogeneous, an error of 600m would have been introduced in the fault location.

Measurements	Value
F	25 km
t_1	93.2 μs
t_2	88.9 μs
Δt	4.3 μs
Classical type-D	25.6 km
Updated type-D	25 km

TABLE 3.2: Classical and updated type D fault location applied to the simulation model.

3.3 Practical considerations

The TWFL algorithms can provide a better precision than impedance fault locators, even for high impedance faults. However, the design and commissioning of the algorithms are more challenging. For an optimal use and precision, the practical difficulties to apply them in practice should be considered.

3.3.1 Technical requirements

The measurement requirements are more restrictive for TWFL than for typical impedance FL.

The propagation of transients is fast (close to the speed of light in overhead lines). Due to this, a good precision is needed in the measurement of their arrival time. To obtain a good precision, a high sampling frequency is required. A minimum of 1 MHz is generally applied, but higher sampling frequencies provide a better precision. This can be compared to the typical measurement equipment used in substation, which use a sampling frequency of 16 kHz.

For type D algorithms, two devices are required. These devices must communicate, and they must be time-synchronized. This synchronization is performed with GPS antenna. The precision of the synchronization affects the precision of the fault location.

3.3.2 Propagation speed

Determining the propagation speed is a constitutive part of the fault location algorithm and will affect its precision. Three options are available to set the propagation speed.

Standard value

The first option consists in using a standard value for the propagation speed in aerial lines, especially for single lines where the propagation speed only slightly differ with regards to the geometry (see Section 2.2.3). The error made for parallel line will be more important. This approach might be useful notably for short lines, where the absolute error caused by the propagation speed is small.

Simulations

The second option consists in modelling the line in order to compute the propagation speed based on its geometry. The disadvantage of this option is that it requires a case by case analysis, and the knowledge of the exact geometry of the line.

Measurement

It is possible to measure the propagation time inside a line by energizing it. Based on this total propagation time, the propagation speed is computed. The error made on this propagation speed depends on the time synchronization, and on the precision of the arrival time measurements. The shorter the line, the larger the absolute error on the propagation speed will be.

For non homogeneous lines, the situation is a more complex when recording the total propagation time. This information is not sufficient to know the propagation speed in each section. An assumption has to be made: either to consider the line as homogeneous, or to assign a propagation speed for one of the section.

3.3.3 Measurement transducers

The effect of the measurement transducers for high frequencies must be considered. For economical and practical reasons, conventional MTs already installed in substations are preferred. The literature agrees that CTs should be

used rather than VTs, since they have a good bandwidth for high frequencies. However, the secondary cable ripples will significantly affect the shape of the current waves recorded (See section 1.7).

In addition to the signal reflections on the secondary cables, the time delay between the CT and the actual substation record must be taken into account. This delay could otherwise affect the measurements of the TW arrival time and introduce an error in the fault location.

Some topology configurations are not suitable for TWFL if only the current measurements are used. When a line is ended in an open circuit, or on a power transformer, the current waves will be reflected with a reflection factor of -1, and no current waves will be recorded. In these situations, the voltage measurements should be preferred, even if they provide a less accurate representation of the voltage waves flowing in the network.

3.3.4 Signal processing

The signal processing of the records is the core of any TW FL algorithm. The aim of the signal processing is to identify the waves if necessary, and to measure their arrival time.

For type-D algorithms, there is no need to recognize TWs from one another, as only the first incident wave reaching each substation is used. In this case, the only requirement needed is the knowledge that a fault occurred, and the first wave encountered is used. When using Type-A algorithms, the challenge is to recognize the first wave reflected on fault point from all other events and reflections occurring on the power network.

When the waves of interest are identified, their arrival time must be measured. The simplest way to do it is by using a threshold. The arrival time of a wave is found when its high frequency content goes over the threshold [34]. This method is subject to errors caused by the noise, the attenuation and distortion of the waves, and most work on TWFL consists in improving the signal processing techniques to measure the arrival times.

3.3.5 In this project

The topics mentioned in this section are dealt with in the following ways in this project:

- The project studies a type-D fault location algorithm with a new signal processing 'Pattern recognition algorithm'.

- A sampling frequency of 16 MHz is used for the measurements, using a GPS for time synchronization with a precision of 100 ns.
- For field records, the propagation speed is computed based on the measurement of the total propagation time. For the non homogeneous line monitored, the propagation speed in single overhead lines is assumed with a standard value.
- The algorithm proposed in this project is analysed with both voltage and current measurements to illustrate the operating principle. A simplified version is then proposed, using only the current measurements, and is more extensively studied. This is done to reflect the fact that current waves will be used in practice due to the better bandwidth of CTs.
- The effect of the CTs secondary cabling on the currents recorded is analysed in part II and taken into account in the algorithm development and performance analysis.
- The fault detection is the task of another independent device. The fault location algorithm analysed in this project is based on the fault records provided by that fault detection device, which is out of the scope of this project.
- The difference of arrival times of the first incident waves in each substation is computed with a pattern recognition algorithm. This algorithm is presented in the following Chapter, and analysed in part II.

Chapter 4

Travelling wave fault location based on Pattern recognition

The precision of FL algorithms based on TWs depends on the measurement precision of the TWs arrival times. The simplest way to make those measurements consist in using a threshold on the high frequency component of the recorded signal. The arrival time is found when the wave amplitude crosses this threshold.

The attenuation and distortion of waves introduce an error in the measurement of arrival times when using a threshold. They cause the wave to become more elongated and to decrease in amplitude. Moreover, the threshold cannot be too small due to the expected noise that will be recorded. Because of this, there might be a time delay between the actual arrival time, and the time at which the wave amplitude reaches the threshold.

The pattern recognition algorithm has been developed to improve the measurement precision of the TWs arrival times [53]. It is based on the construction of two signals $S_1(t)$ and $S_2(t)$, each consisting of a combination of local and remote voltage and current waves. Those signals will present similar patterns, but shifted by the time Δt used in the type-D equation. The purpose of the algorithm is to determine the time shift for which the patterns are the most similar, using a least square estimation (LSE).

Some resemblance might be noted with a cross-correlation protection method presented in [54]. In this method, two signals are built at a single-end relay based on the current and voltage measurements, and will be similar for the first incident wave and for the wave reflected on fault point. As such, that method aims at identifying the first wave reflected on fault point for a type-A fault location. In contrast, the two signals $S_1(t)$ and $S_2(t)$ developed in this chapter do not aim at identifying waves, but at determining the time Δt used in the type-D fault location.

The theoretical development of the algorithm, based on the Telegrapher equations, is first proposed. The algorithm is then illustrated with a simple simulation. The practical difficulties to apply the algorithm are then discussed, and further simplifications are proposed to take them into account. The impact of the assumptions, simplifications and parameters are then discussed. Finally, a complete implementable description of the algorithm is provided.

The algorithm described in this chapter is tested on fault records and on simulations in Chapter 8.

4.1 Theoretical development

Let us consider a basic single phase line with the fault resistance R_F. This line is represented by two 4-terminal networks with constant distributed parameters connected at fault point (Figure 4.1). The assumptions of the constant distributed line models apply to the algorithm, namely the propagation

speed and the characteristic impedance are constant, and the attenuation and distortion factors are neglected.

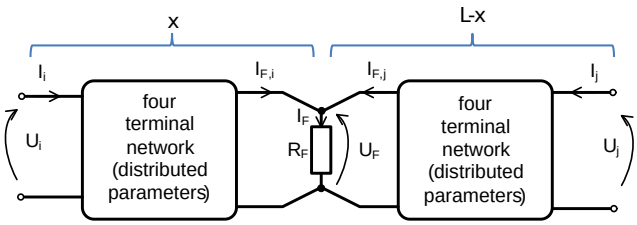

FIGURE 4.1: A line with a fault is modelled as two four-terminals networks, connected at fault point.

4.1.1 Starting equations

The voltage at fault point can be described using telegrapher's equations. An appropriate reformulation of the telegrapher's equations for each network in the Laplace domain 1.21 leads to the following equations for the voltage at fault point:

$$U(x,s) = \frac{1}{2}e^{-\gamma(s)x}\big(U_1(s) + Z_c(s)\cdot I_1(s)\big) + \frac{1}{2}e^{\gamma(s)x}\big(U_1(s) - Z_c(s)\cdot I_1(s)\big) \tag{4.1}$$

$$U(L-x,s) = \frac{1}{2}e^{-\gamma(s)(L-x)}\big(U_2(s) + Z_c(s)\cdot I_2(s)\big) + \frac{1}{2}e^{\gamma(s)(L-x)}\big(U_2(s) - Z_c(s)\cdot I_2(s)\big) \tag{4.2}$$

where:

- x is the fault location
- U_F is the voltage at the fault point
- U_i is the voltage at node i
- I_i is the current at node i

Since the voltage at the fault location x can be expressed as voltages and currents from the local and remote sides separately, the additional boundary condition can be introduced in order to find the unknown fault position x:

$$U_F = U(x,s) = U(L-x,s) \tag{4.3}$$

By combining (4.1),(4.2) and (4.3), we obtain:

$$e^{-\gamma(s)(2x-L)} S_{full,2}(s) = S_{full,1}(s) \tag{4.4}$$

We introduce $S_{full,1}$ and $S_{full,2}$, as a combination of currents and voltages measured at the local and remote line side:

$$S_{full,1}(s) \;=\; e^{-\gamma(s)L}\big(U_2(s) + Z_c(s)\cdot I_2(s)\big) - \big(U_1(s) - Z_c(s)\cdot I_1(s)\big) \tag{4.5}$$

$$S_{full,2}(s) \;=\; e^{-\gamma(s)L}\big(U_1(s) + Z_c(s)\cdot I_1(s)\big) - \big(U_2(s) - Z_c(s)\cdot I_2(s)\big) \tag{4.6}$$

The subscript "$full$" is introduced to emphasize that the complete version of signals S_1 and S_2 is used. This will be important when introducing the simplifications on S_{full} in section 4.3. For a better understanding of the effect, as well as an effective implementation of the algorithm, the signals will be converted to the time domain.

4.1.2 Building the signals

With the lossless assumption, we obtain:

$$e^{-\gamma(s)(2x-L)} = e^{-s\frac{2x-L}{v}} = e^{-s\Delta t} \tag{4.7}$$

The following relation between time domain and Laplace domain is then valid:

$$\mathcal{L}\big(S(t-\Delta t)\big) = e^{-s\Delta t} S(s) \tag{4.8}$$

Under the assumption that Z_c is constant in the evaluated frequency spectrum (4.5) and (4.6) can be formulated in the time domain:

$$S_{full,1}(t) \;=\; U_2(t - L/v) + Z_c\cdot I_2(t - L/v) - \big(U_1(t) - Z_c\cdot I_1(t)\big) \tag{4.9}$$

$$S_{full,2}(t) \;=\; U_1(t - L/v) + Z_c \cdot I_1(t - L/v) - \big(U_2(t) - Z_c \cdot I_2(t)\big) \quad (4.10)$$

The conclusions from these equations when combined with (4.4) is that the difference between $S_{full,1}(t)$ and $S_{full,2}(t)$ can be expressed as a time difference Δt dependent on the fault location x.

$$S_{full,2}(t - \Delta t) = S_{full,1}(t) \quad (4.11)$$

Each signal $S_{full,1}(t)$ and $S_{full,2}(t)$ is a combination of local data, and remote data delayed by the propagation time inside the line ($\tau = \frac{L}{v}$). For example, $S_{full,1}(t)$ combines local records at substation 1:

$$U_1(t) - Z_c \cdot I_1(t) \quad (4.12)$$

and remote records at substation 2 delayed by a time τ:

$$U_2(t - \tau) + Z_c \cdot I_2(t - \tau) \quad (4.13)$$

4.1.3 Pattern recognition

If the signal $S_{2,full}(t)$ is shifted by a time Δt, it will be exactly similar to the signal $S_{1,full}(t)$ under the assumptions made. The objective of the algorithm is to use a pattern recognition algorithm for different time shifts of S_2. The time shift at which the pattern recognition is largest is then used to find the fault location with a type-D fault location equation.

$$\Delta t = \frac{(2x - L)}{v} \quad (4.14)$$

The pattern recognition algorithm used is a least square estimation (LSE) (4.15). The LSE computes the squared discrepancies between the two signals [55] in the given time window T_F, and will be minimal when the two signals are the most similar. The difference in arrival time of the travelling waves Δt is found when the LSE is minimum.

$$Q_{S_1S_2}(y) = \int_{t_0}^{t_0+T_F} [S_1(t) - S_2(t + y)]^2 \, dt \quad (4.15)$$

$$\Delta t = min_y\big(Q_{S_1S_2}(y)\big) \quad (4.16)$$

Other pattern recognition algorithms could be used instead; the point is to determine when the similarity between the signals is maximum.

4.2 Basic principle illustration

The algorithm is illustrated with a simple simulation performed using EMTP. A Bergeron line model is used, which satisfies the assumptions made for the algorithm development (lossless line, constant parameters, no attenuation or distortion).

Figure 4.2 shows the topology of the 65 km line modelled. Node 2 is directly connected to a source impedance that will create a reflection factor for the waves. Node 1 is connected to a short 5 km external line. No reflection will occur immediately, since the line is extended by another line with comparable line parameters, but the reflections at the end of this short external line will be observed on node 1. The fault occurs 15 km from node 1.

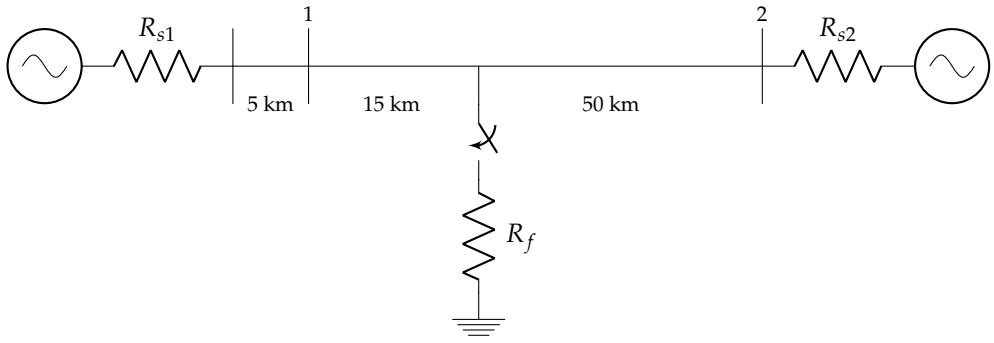

FIGURE 4.2: Topology of the Bergeron line model. $R_{s1} = 400\Omega$, $R_{s2} = 100\Omega$, $Rf = 0.1\Omega$, $Z_c = 250\Omega$, $v = 297m/\mu s$

Figure 4.3 shows the simulated currents and voltages at each end of the line, and the signals $S_{1,full}(t)$ and $S_{2,full}(t)$ built based on them. Despite different reflections occurring at both ends of the line on voltage and current waves, the signals S_{full} are exactly similar, with a time shift.

Figure 4.4 shows the result of the LSE performed for different time shifts of $S_{2,full}(t)$. The minimum is found when the signals are the most similar and is the sought time-shift. The minimum of the LSE is found for a time-shift of $117.8\mu s$. Using (4.14), the fault location is computed at $15004m$.

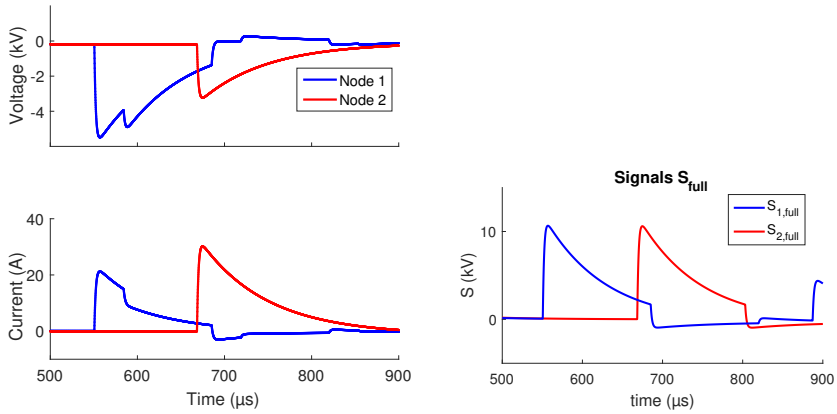

(A) Currents and voltages at each node.

(B) Signals $S_{1,full}$ and $S_{2,full}$.

FIGURE 4.3: Signals $S_{1,full}$ and $S_{2,full}$ build based on the currents and voltages at each node.

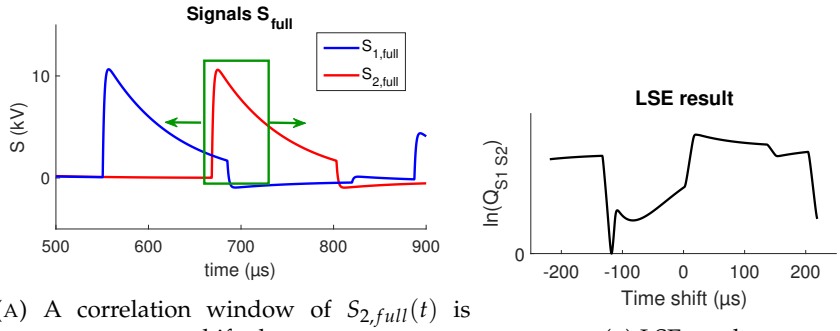

(A) A correlation window of $S_{2,full}(t)$ is shifted.

(B) LSE result

FIGURE 4.4: A LSE is performed for different time shifts of $S_{2,full}(t)$.

4.3 Practical challenges and solutions

The pattern recognition provides a very good precision on Bergeron line models. However, the assumptions made for those models are unrealistic. There are some challenges to apply this algorithm as-is on real transmission lines, both due to those assumptions and to practical measurement limitations. Those challenges are listed here, and solutions and simplifications of the algorithm are proposed to overcome those difficulties.

4.3.1 Big data transfer - $S_{Reduced}$

The signals $S_{full}(t)$ are computed by combining local and remote data. The data exchanged can be significant, and complicate the practical implementation of the algorithm. A first simplification proposed is to neglect the data from the remote end (4.13). Equation (4.11) reduces to:

$$e^{-s\frac{(2x-L)}{v}}\left[-\left(U_2(s)-Z_c(s)\cdot I_2(s)\right)\right] \approx \left[-\left(U_1(s)-Z_c(s)\cdot I_1(s)\right)\right] \quad (4.17)$$

$$e^{-s\frac{(2x-L)}{v}} S_{2,reduced}(s) \approx S_{1,reduced}(s) \quad (4.18)$$

As seen in the reduced equations (4.17), the terms removed are delayed by τ, the total travel time in the line. The simplification therefore remains exactly correct for $t < \tau$, starting from fault time. For $t > \tau$, the equality is no longer correct (Figure 4.5).

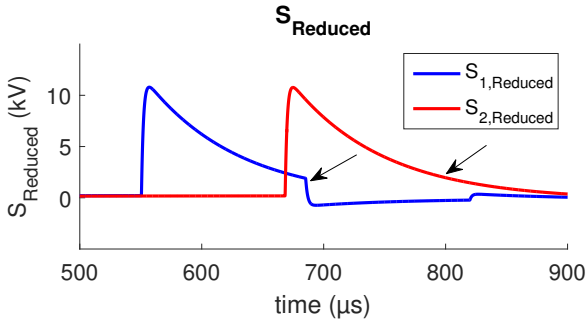

FIGURE 4.5: Signals $S_{1,reduced}$ and $S_{2,reduced}$ differ when $t > \tau$.

4.3.2 Unreliable voltages - S_I

The pattern recognition algorithm is based on building two similar signals from the currents and voltages measurements. However, we saw in Section 1.7.1 that VTs provide unreliable measurements. It is therefore not practically possible to build the two signals $S_{1,full}(t)$ and $S_{2,full}(t)$.

As seen in (4.17), the signal $S_{reduced}$ is a linear combination of voltages and currents. The progression of voltages and currents can therefore be considered individually. The second simplification proposed is to only look at the current waves and to remove the voltage wave terms from the equations. These equations reduce to:

$$e^{-s\frac{(2x-L)}{v}} I_2(s) \cong I_1(s) \tag{4.19}$$

$$e^{-s\frac{(2x-L)}{v}} S_{2,I}(s) \cong S_{1,I}(s) \tag{4.20}$$

This simplification assumes a constant Z_c, and does not take into account the fact that voltages and current waves can be reflected with a different reflection factor at the measurement point (which affects the signal amplitude), or on elements external to the line (which affects the shape of the signals) (Figure 4.6).

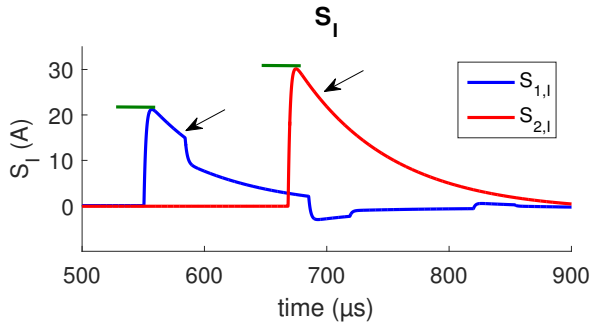

FIGURE 4.6: Signals $S_{1,I}$ and $S_{2,I}$ have different amplitudes. Their shapes differ when outside reflections occur.

4.3.3 Attenuation and reflections - Correction factor

Due to attenuation, the amplitude of $S_1(t)$ and $S_2(t)$ will change. Due to different reflection factors at measurement points, the amplitude of $S_I(t)$ also changes (but not the amplitude of $S_{full}(t)$ or $S_{Reduced}(t)$). The amplitudes of the signals built will therefore differ, while their shapes are not affected. To help the pattern recognition, a correction factor is applied as in (4.21) to compare signals of similar amplitudes (Figure 4.7).

$$S'_{I,2} = \frac{max(S_{I,1})}{max(S_{I,2})} \cdot S_{I,2} \tag{4.21}$$

4.3.4 Secondary cable ringing - notch filter

We saw in section 1.7.2 that the secondary-side cabling of CTs disturbs the current waves measurements by introducing fast reflections. These reflections are device-specific, and differ from substation to substation. The signals

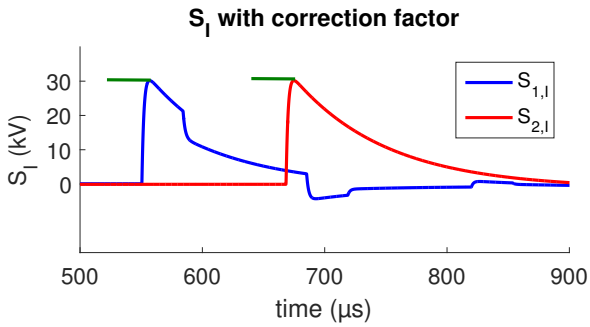

FIGURE 4.7: Signals $S_{1,I}$ and $S_{2,I}$ have the same amplitude with the correction factor. Their shape still differ when outside reflections occur.

$S(t)$ are affected, and the equalities (4.11), (4.17) or (4.20) are not correct anymore.

To correct the effect of the secondary cables, we propose the use of notch filters. Notch filters are special kinds of band stop filters. Band stop filters pass all frequencies with the exception of those within a specified stop band which are attenuated. A notch filter is a band stop filter with a narrow stop band. A perfect notch filter would only remove a specific frequency f_c [56] (Figure 4.8).

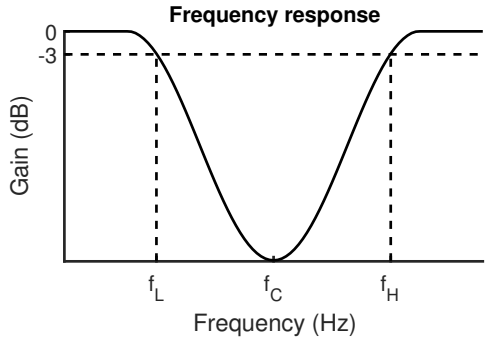

FIGURE 4.8: Frequency response of a notch filter. The frequencies between f_L and f_H are attenuated.

If the frequency introduced by the secondary cables of a specific current transformer is known, a notch filter can be designed to filter them out. The two parameters of a notch filter are the frequency to be removed f_C, and the quality factor Q, which determines the width of the stop band bw. This stop band is the range between the low frequency cut-off f_L and the high frequency cut-off f_H. Both cut-off frequencies are attenuated by a ratio $3dB$.

$$bw = f_H - f_L \tag{4.22}$$

$$Q = \frac{Q}{bw} \tag{4.23}$$

4.3.5 Line parameters knowledge

Building the signals $S_{full}(t)$ and $S_{reduced}(t)$ requires the knowledge of the characteristic impedance Z_c. For simulation models this impedance can be readily known. For real lines, it needs to be computed based on the line geometry, or assumed. This is not a problem when using the signals $S_I(t)$.

The knowledge of the propagation speed inside the line also influences the precision of the FL algorithm. However, this error is inherent to the TW FL algorithms, and not to the pattern recognition algorithm as a wave detection algorithm.

4.3.6 Distortion

The lossless assumption, needed for the transformation to the time domain, implies a distortion-less line. In practice, distortion will affect S_1 and S_2, slightly changing their shapes (Figure 4.9). This will introduce an error in the pattern recognition.

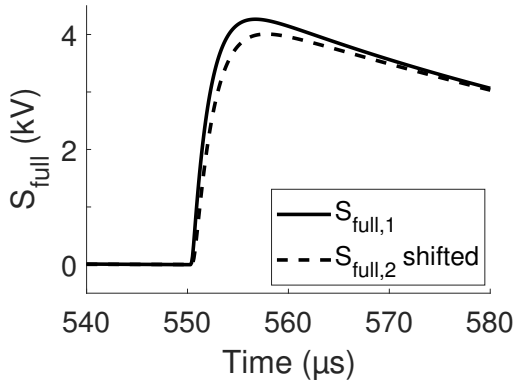

FIGURE 4.9: Signals $S_{1,full}$ and $S_{2,full}$ have different amplitudes and shapes due to the attenuation and distortion of the J-Marti line model.

We do not propose a solution for this error, which is inherent to the algorithm. The analysis carried out in Part II shows that the error caused by the

distortion is relatively small and does not affect the algorithm precision in a significant way.

4.4 Algorithm description

The algorithm proposed is based on the analysis of the currents and voltages recorded during a fault. Therefore, we assume that the task of the fault protection and signals recording (including the trigger) is handled by a separate algorithm.

4.4.1 Pre-computations

The following quantities must be computed or introduced in the algorithm prior to the fault location. They are dependent on the geometry and topology of the monitored line, and on the measurement equipment.

- The sampling frequency S_f
- The line length L
- The propagation velocity v
- The characteristic impedance Z_c (only needed for S_{full} and $S_{Reduced}$)
- The total propagation time in the line τ
- The propagation time in the secondary cables in each substation
- The frequency of the secondary cable ripples in each substation

4.4.2 Define the value of the parameters

The following parameters will affect the precision of the pattern recognition algorithm. Their values must be defined before applying the fault location algorithm. Those parameters are analysed and discussed in Chapter 8.

- The threshold used to determine the approximate arrival time of the first wave at one end of the line, t_x
- The length of the correlation window that will be shifted, on which the LSE will be applied. This correlation window will be surrounding t_x as in: $[t_x - t_a; t_x + t_b]$

- The signals S that will be build (S_{full}, $S_{Reduced}$, S_I)
- The band-pass filter used to remove the power frequency as well as the high frequency noises.
- The notch filters used to remove the secondary ripples in each substation

4.4.3 Apply the pattern recognition algorithm

Once all the parameters are defined, the algorithm proceeds as follow:

- The bandpass filter and notch filters are applied to the signals recorded.
- A Clarke transform is applied on the voltage and current records.
- The aerial mode with the biggest wave energy is selected for the fault location algorithm.
- The signals $S_1(t)$ and $S_2(t)$ are computed based on the modal currents and voltages, and the correction factor is applied as in (4.21).
- The approximated arrival time t_x of the first wave on $S_2(t)$ is found using a threshold.
- The window $[t_x - t_a; t_x + t_b]$ of $S_2(t)$ is shifted from $-\tau$ to τ with increments of one sample.
- For each time shift of $S_2(t - x)$, the LSE $Q_{S_1S2}(x)$ between the shifted signal and $S_1(t)$ is computed.
- The time shift x for which the LSE $Q_{S_1S2}(x)$ is minimum is the difference in arrival times Δt.
- The fault location is computed as in (4.14).

4.5 Discussion

The pattern recognition algorithm presented in this chapter is based on building two signals $S_1(t)$ and $S_2(t)$. Those signals are exactly similar for the set of assumptions made. When those assumptions are correct, the algorithm provides a perfect fault location.

Because those assumptions are unrealistic, and due to the practical limitations of recording the voltages and currents in substations, errors are introduced in the fault location. This error will depend on the line topology and on the algorithm parameters.

The algorithm is applied to simulation and fault records in Chapter 8, in order to assess its performance and determine the effect of the topology and algorithm parameters.

Part II

Results

The second part of this report focuses on the results from the practical tests and simulations performed.

In Chapter 5, the effect of substation MTs on the recorded TWs is tested in a high voltage laboratory. The set-up of an actual substation is reproduced, and an impulse test is generated to reproduce the wave generated during a fault.

In Chapter 6, the results of the measurement campaign performed in Elia (the Belgian TSO) are presented. A two-ended record of TWs generated during a lightning fault was recorded. This record is extensively analysed, and it is used to illustrate all the characteristics presented before as well as the FL algorithm described in part I.

In Chapter 7, the substation set-up tested in the previous chapter is implemented in EMTP. The model performance is compared with the lab records, and is added to the complete power system model. A set of case studies are then presented to study the FL algorithm.

In Chapter 8, the pattern recognition algorithm is applied and studied with the case studies. The different sources of error and the effect of the algorithm parameters are highlighted. The algorithm performance is assessed with the complete power system models and with the fault record.

Chapter 5

Substation measurements

Substation measurements significantly affect the shapes of the current waves recorded (see Section 1.7). The literature agrees on their qualitative effects, but actual transfer functions of measurement systems for high frequencies are rare, especially when including the secondary cables.

The effect of substation measurements on the waves recorded needs to be better understood and quantified. Algorithms based on TWs depend on the waves actually recorded. Any alteration on those recorded waves has the potential to invalidate the algorithms, or otherwise decrease their precision.

A substation measurement system was reproduced and tested in a high voltage laboratory by generating a lightning impulse. This impulse reproduces the current waves that are generated when lightning strikes on an overhead line.

This chapter first presents and defines the lightning impulse standard, and the practical ways to generate them in a laboratory. The generator circuit used in our tests, and the substation reproduced, are then described. The results of the laboratory tests are analysed, and a solution to cancel the effect of the measurement system using notch filters is proposed and tested.

The tests show that the main effect of the measurement system is a clear resonance frequency. This resonance frequency is caused by the secondary cables. These cables introduce fast reflections on the measurements which are quickly attenuated. Because those reflections have a fixed frequency for a specific substation configuration, notch filters can be designed to filter out the effect of the measurement system.

It comes out from this analysis that algorithms based on TWs can efficiently correct the effect of measurement substations. If the resonance frequency introduced by a specific substation is known, which is doable by analysing any TW record from the substation, an adequate notch filter can be designed.

5.1 Lightning impulse

The lightning impulse voltage standard was created to simulate the transient voltages generated during a lightning stroke on the power network. They can be generated inside a laboratory by charging and discharging capacitors.

Single-stage circuits are based on the charging of a single capacitor. Multi-stage circuits are more complex: they charge multiple capacitors in series, and are more practical to generate high voltage impulses. The tests presented in the next section use such a multi-stage circuit generator.

5.1.1 Definition

A lightning impulse voltage is defined as an unidirectional voltage which rises rapidly to a peak value, and then decays more slowly to zero. The impulse is characterized by its peak value V_p, its front time T_1, and its tail time T_2 (Figure 5.1)][35, 57–59].

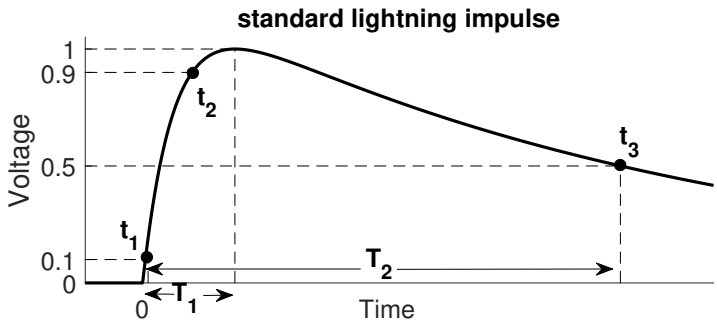

FIGURE 5.1: Standard lighting impulse voltage [60].

The front time T_1 is the time to reach the maximum value from zero. It is difficult in practice to determine the start and peak points of the wave. The front time is then expressed as 1.25 times $(t_2 - t_1)$, where t_1, the nominal starting point, is the time to reach 10%, and t_2 is the time to reach 90% of the peak value.

The tail time T_2 is the time between the nominal starting point t_1 and the point on the wave tail where the voltage is 50 % of the peak value [35].

The standard lightning impulse, representing the shape of the transients generated during a lightning stroke on the power system, is the so-called 1.2/50 impulse [59]. This 1.2/50 impulse has a front time of 1.2 μs and a tail time of 50 μs. In general, the specifications permit a large tolerance on those parameters, due to the difficulty to precisely design generator circuits. According to [61], the recommended times are $1.2\mu s \pm 30\%$ and $50\mu s \pm 20\%$.

5.1.2 Single stage generator circuit

The wave-shape of a lightning impulse can be composed by the superposition of two exponential functions. This can be done in practice with the discharging of energy stored in capacitors. Two main circuits exist to do so, varying in the disposition of the earthing resistance R_2. Figure 5.2. shows one of those basic single-stage impulse generator circuits.

In a single stage circuit, a capacitor C_1 is slowly charged from a DC source until the spark gap G breaks down. The impulse voltage is recorded across the load capacitor C_2. The values of the resistors R_1 and R_2, and of the capacitances C_1 and C_2 control the wave shape. [59] provides assumptions to compute the front and tail times with:

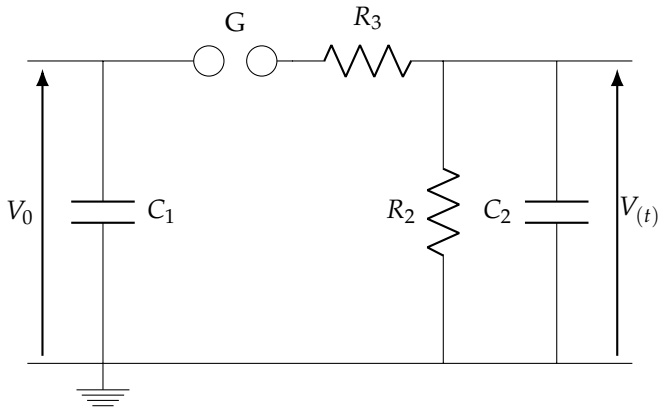

FIGURE 5.2: Single stage impulse generator circuit.

$$T_1 \approx 2.96\, R_1 \frac{C_1 C_2}{C_1 + C_2} \tag{5.1}$$

$$T_2 \approx 0.73\, (R_1 + R_2)(C_1 + C_2) \tag{5.2}$$

The basic circuit shown on Figure 5.2 neglects the stray capacitances and inductances of the circuit elements. Those stray capacitances and inductances are in practice impossible to remove completely. They will affect the time constants, and they may introduce oscillations and overshoot on the voltage impulse (Figure 5.3).

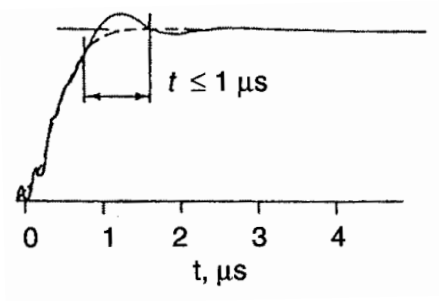

FIGURE 5.3: Example of oscillations and overshoot recorded during a lightning impulse [57].

The permissible tolerances for T_1 and T_2 are necessary. The design of a standard impulse is difficult to achieve in practice for two reasons [59]: it requires the use of precisely dimensioned resistances which is expensive, and

the stray capacitance and inductance of the system significantly affect the time constants.

The oscillations and overshoot that may occur are generally accepted if they remain under a certain level. The overshoot at the crest of the impulse should remain under $1\mu s$. The oscillations on the front of the impulse, below 50% of the crest value, should have a peak amplitude of maximum 25% [59]. Those tolerances include the differences between the recorded signal and the actual impulse.

When oscillations and overshoot occur, a 'mean curve' should be drawn through the curve. This mean curve is used to determine the peak value, front and tail times of the impulse [59].

5.1.3 Multi-stage generator circuit

It is practically and economically inconvenient to design single-stage generator circuits for high peak voltage for three reasons:

- The physical size of the circuit becomes large
- A high DC charging voltage is required
- Switching of very high voltage with spark gaps is difficult

To overcome those difficulties, Marx designed multi-stage generator circuits in which multiple capacitors are charged in parallel and discharged in series through multiple spark gaps [59]. Figure 5.4 shows an example of a three-stage circuit.

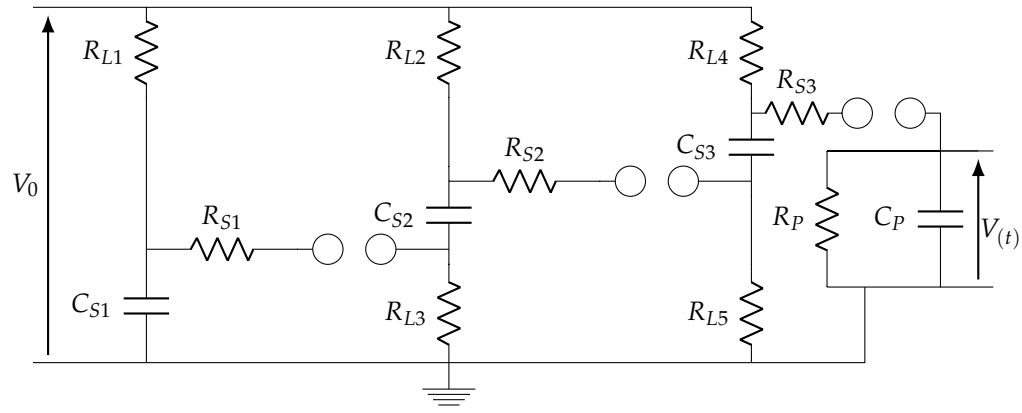

FIGURE 5.4: Three-stage impulse generator circuit.

The loading resistances R_L are significantly larger than the resistances R_S, and are seen as an open circuit once the spark gaps have fired. When those spark gaps fire, we can therefore simplify the circuit to the single stage circuit of Figure 5.2 [59]. The total discharge capacitance C_1 of this specific circuit is computed with:

$$\frac{1}{C_1} = \frac{1}{C_{S1} + C_{S2} + C_{S3}} \tag{5.3}$$

The front resistance R_1 is computed with

$$R_1 = R_{S1} + R_{S2} + R_{S3} \tag{5.4}$$

And the earthing resistance R_2 with

$$R_2 = R_P \tag{5.5}$$

5.1.4 Current impulse

An associated current impulse is generated during a voltage impulse test. It flows inside the earthing resistor R_2 (Figure 5.2). If that resistance was purely resistive, the impulse would be a perfect image of the voltage impulse.

The time constants of the current impulse may differ from the voltage impulse due to the stray inductance of this earthing resistance [57].

Most laboratory, including the laboratory used for these tests, are designed to record voltage impulses. This leads to impractical current impulse measurements, which are affected by the EM noise and the stray inductances.

5.2 Test set-up

Two test set-ups are used for the tests (Figure 5.5). In both set-ups, the current generated during a lightning stroke is reproduced with a current lightning impulse.

In the first set-up, the CT is short-circuited and the currents are recorded inside the HV laboratory to observe the effect of the CT itself. The second set-up simulates a substation in which the currents are recorded 100m away from the CT, to observe the effect of the full system. The following elements are reproduced :

- The current waves generated during a lightning stroke are represented with a current lightning impulse.

- A medium voltage (MV) CT is used to reduce the currents before their measurements.
- 2 times $100m$ of cables are used to carry the secondary current from the CT to the measurement point.
- The termination burden of the secondary cables, present in the substations, is taken into account by placing a protection relay at the end of the $100m$ cable.

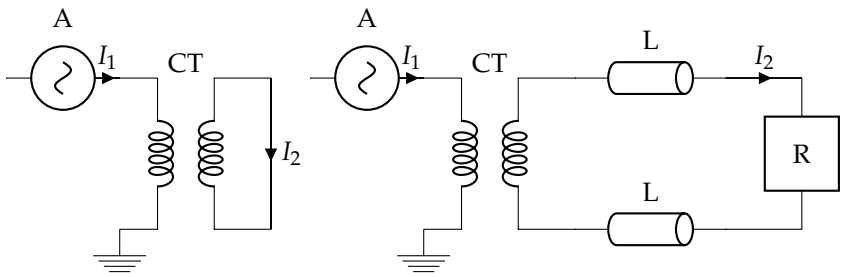

(A) Set-up 1 (B) Set-up 2

FIGURE 5.5: Lightning impulse test set-up. A: current impulse, CT: current transformer, L: 100m secondary cables, R: protection relay.

5.2.1 Lightning current impulse generator

The three-stage circuit represented on Figure 5.4 is used to generate a 26 kV voltage impulse, and an associated 50 A current impulse. The values of the circuit elements are available on Table 5.1. The impulse current is recorded flowing in the resistance R_P.

Element	Value
R_{S1}	$105\,\Omega$
R_{S2}	$80\,\Omega$
R_{S3}	$47\,\Omega$
R_{L1}	$10^6\,\Omega$
R_P	$528\,\Omega$
C_P	$0.003\,\mu F$
$C_{S1} = C_{S2} = C_{S3}$	$0.26\,\mu F$
$R_{L2} = R_{L3} = R_{L3} = R_{L5}$	$0.5\,10^6\,\Omega$

TABLE 5.1: Elements of the lightning impulse generator circuit.

Using (5.3), (5.4) and (5.5), this three-stage generator can be reduced to the single stage generator of Figure 5.2 with:

$$R_1 = R_{S1} + R_{S2} + R_{S3} + R_{S4} + R_{S5} = 202\,\Omega \tag{5.6}$$

$$R_2 = R_P = 528\,\Omega \tag{5.7}$$

$$C_1 = \frac{C_S}{3} = 0.087\,\mu F \tag{5.8}$$

$$C_2 = C_P = 0.003\,\mu F \tag{5.9}$$

The expected front and tail times are therefore estimated with (5.1) and (5.2) as:

$$T_1 \approx 1.73\,\mu s \tag{5.10}$$

$$T_2 \approx 48\,\mu s \tag{5.11}$$

5.2.2 Equipment description

The equipment used to represent a substation is described in Appendix C. Its main characteristics are:

Current transformer

The current impulse is reduced using a conventional iron-cored MV CT with the following characteristics:

- Transformation ratio: 125/5
- Nominal voltage: $7.2\,kV$
- Maximum peak voltage: $28\,kV$

Secondary cables

The secondary cables used in the second set-up were chosen based on the cables used by Elia in their substations (see measurement campaign, Chapter 6). Those cables have the following characteristics [62]:

- Length: 2 times 100 m
- Conductor: Solid copper, $4mm^2$ section
- Isolator: PVC, 0.8 mm thickness

Secondary cable burden

Multiple devices are installed in substations at the end of the secondary cables, such as fault recorders and protection relays. In the second set-up, the secondary cables are connected to a protection device "Siprotec 5" [63].

Measurement equipment

The currents are recorded using the following measurement equipment:

- A digital oscilloscope "Picoscope 4824" with a bandwidth up to 20 MHz. Sampling frequency: 80 MHz [64].
- Rogowski coil current probes "CWT1N" with a bandwidth [25 Hz - 10 MHz] and a sensitivity of 20 mV / A [65].
- A Faraday cage is used to record the currents inside the high voltage lab (set-up 1). This cage is needed to decrease the effect of the EM noise.

5.3 Test results

5.3.1 Records

Primary current I_1

The primary current recorded during the lightning impulse test is seen in Figure 5.6. Clear oscillations and overshoot are present on the front side of the impulse. Those oscillations will not disturb the results of the laboratory tests. The frequency response of the two measurement system set-ups will be evaluated by taking these oscillations into account.

The front and tail times are computed with (5.1) and (5.2), using the recorded times t_1, t_2 and t_3:

$$T_1 = 1.42\,\mu s$$

$$T_2 = 42.2\,\mu s$$

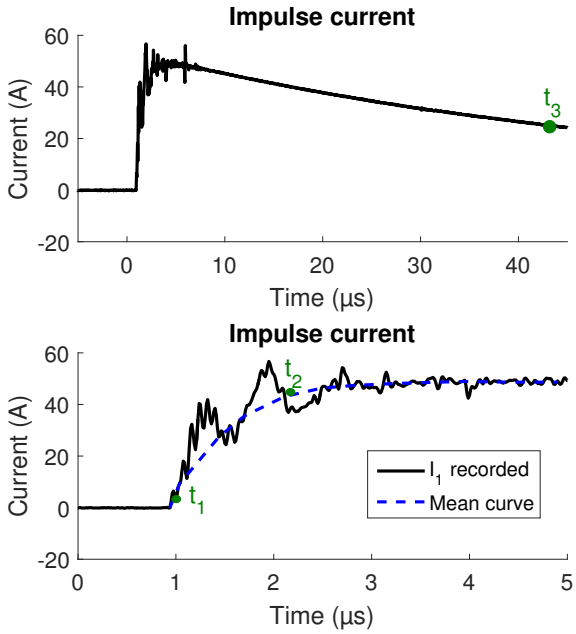

FIGURE 5.6: Lightning impulse current generated in the HV lab: primary current recorded.

The small difference compared to the estimations made in section 5.2.1 ($T_1 \approx 1.73\mu s$, $T_2 \approx 48\mu s$) were expected, and are explained with the stray capacitances and inductances of the physical circuit.

Secondary current inside the HV lab (setup 1)

During the experiments with set-up 1, the primary and secondary currents are recorded simultaneously (Figure 5.7). Because the secondary measurements are taken close to the experiment, they are sensitive to the EM noise. This high frequency noise is clearly visible on the figure.

The secondary currents closely follows the primary current for the lower frequencies. Due to the EM noise, the highest frequencies will not be analysed as the noise-to-signal ratio is too high.

Secondary current 100m from experiment (setup 2)

The secondary currents recorded 100 m away from the experiment are not affected by the EM noise. In these experiments, the primary and secondary currents are not recorded simultaneously for practical reasons. They are synchronized with the other curves in post-processing, which explains why there

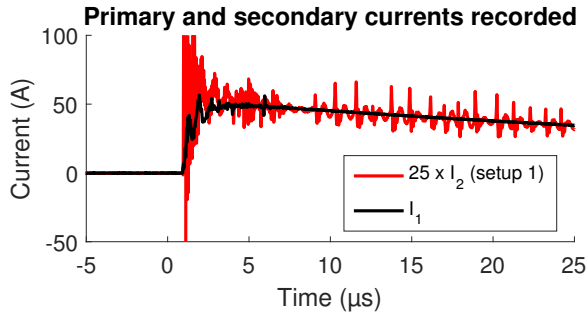

FIGURE 5.7: Primary current and secondary current recorded inside the HV lab.

is no delay between the primary current and the secondary currents recorded 100 m further (Figure 5.8).

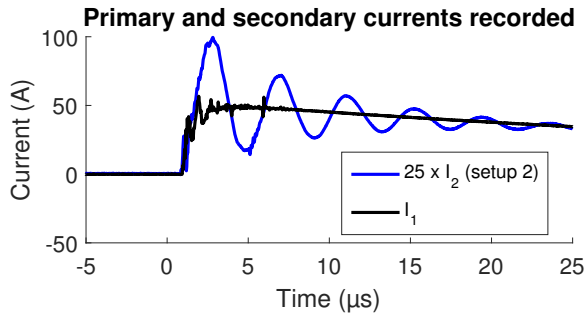

FIGURE 5.8: The secondary current recorded 100m away from the HV lab shows reflections occurring on the secondary cables.

The secondary current also follows closely the primary current, but with the additional reflections on the 100 m cables. Those reflections are clearly observed on the records, and were expected based on the literature review. They are quickly attenuated.

5.3.2 CT transfer function

The measurement system transfer functions of each set-up are shown on Figure 5.9. Those transfer functions are computed using an average of fast fourier transforms (FFTs) computed on records from 6 distinct experiments.

The bandwidth of the system set-up 1 (recorded inside the lab) is somewhat flat until 100 kHz. The gain then slightly increases and the results are not significant for higher frequencies, due to the EM noise affecting the records.

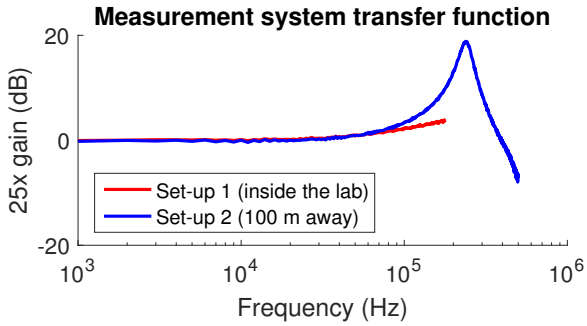

FIGURE 5.9: Transfer function of each measurement system set-up, averaged over 6 records. Extended version available in D.

System set-up 2 (with 100m secondary cables) presents a flat bandwidth, with a clear resonance peak at 238 kHz. This behaviour is expected from all the analysis previously made on the subject. The 100 m of cable introduce reflections on the recorded currents. The frequency of those reflections depend on the propagation speed on these cables, and on the cables length.

These tests show that the MV CT tested has a sufficient bandwidth for recording TWs (up to 100 kHz). The tests also show that including long secondary cables significantly affect the shape of the waves recorded by introducing a clear resonance frequency due to the fast reflections. This is the situation that can be expected from records performed in substations.

5.4 Notch filter

We propose to cancel the effect of the secondary reflections with the use of a notch filter (defined in Section 4.3.4). These kind of filters pass all frequencies without altering the signals, with the exception of a narrow stop band which is attenuated. This allows us to filter out the resonance frequency introduced by the secondary cables without affecting the rest of the signal.

The notch filter is efficient at decreasing the effect of this measurement system set-up. Its design depends on the quality factor, which determines the bandwidth to be attenuated. If the quality factor is chosen too big, the stop band is too narrow: the secondary reflections are not correctly attenuated. If the quality factor is chosen too small, the stop band is too wide: the travelling wave itself is distorted.

5.4.1 Notch filter design

The bandwidth to be attenuated is defined in the notch filter as $[f_l\, f_h]$, centered around the frequency to be removed f_c. The low and high cut-off frequencies f_L and f_H are attenuated by $-3\,dB$.

The quality factor Q determines the length of the bandwidth to be attenuated bw, as in 5.13. For a high quality factor, a narrow bandwidth will be attenuated.

$$Q = \frac{f_C}{bw} \tag{5.12}$$

$$bw = f_H - f_L \tag{5.13}$$

We design the notch filter based on the transfer function recorded (Figure 5.10). The lowest frequency of the peak resonance at 3 dB is f_L = 94 kHz. With the peak of the resonance frequencies located at f_c = 238 kHz, the notch filter is chosen with the following parameters:

- f_C = 238 kHz
- bw = $2(f_C - f_L)$ = 258 kHz
- Q = $\frac{f_C}{bw}$=0.82

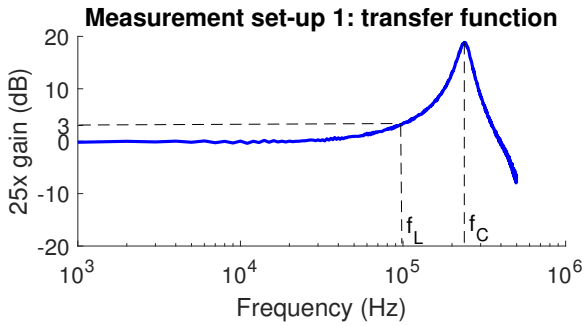

FIGURE 5.10: The cut off frequencies to design the notch filter are measured on the measurement system transfer function.

5.4.2 Results

Figure 5.11 shows the results when applying the notch filter. The oscillations created by the reflections in the secondary cables are greatly attenuated.

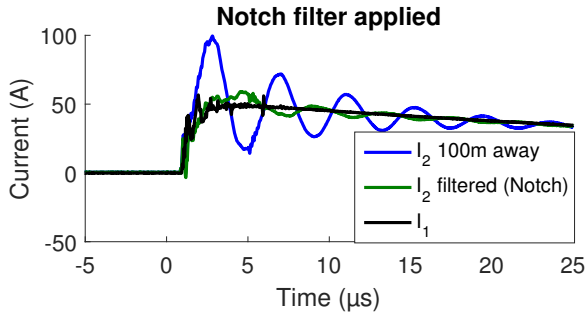

FIGURE 5.11: The notch filter decreases the effect of the reflections occurring on the secondary cables.

If the quality factor is not chosen correctly, the output of the notch filter will be greatly affected (Figure 5.12). If it is too high, the attenuated bandwidth will be too narrow, and the oscillations will not be well attenuated. If it is too small, the attenuated bandwidth will be too big and the TW itself will be distorted by the filter.

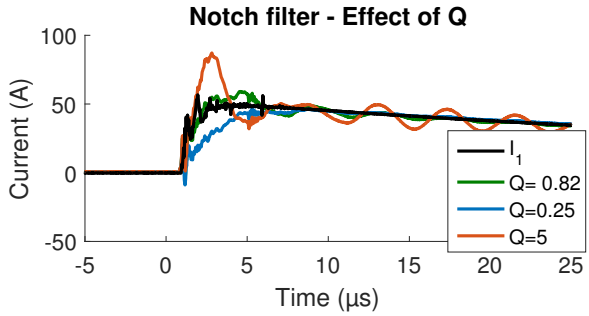

FIGURE 5.12: The quality factor is an important parameter that determines the effect of the notch filter.

It is simple to design a suitable notch filter when the transfer function of the measurement system is available. For measurement substation, this is not the case, and assumptions must be made when deciding on the quality factor. This question is analysed in the next chapter, with fault records acquired in the Belgian transmission network.

5.5 Discussion

The MV CT tested provided a bandwidth suitable for TW studies. When long cables are connected on the secondary side of the CT, the effect on the current

recorded appears like a resonance frequency. Those reflections are attenuated in about 25 μs as shown in Figure 5.8.

The CT tested in this chapter is a medium votlage CT, both due to availability and suitability with the HV lab. The results obtained cannot be generalised to any HV CT; It is however expected, based on the literature, that they will behave in a similar way.

Notch filters were shown to efficiently reduce the measurement substations effect when well designed. When the transfer function of the measurement system is known, we showed that the design of this filter is straightforward. In practical applications, the transfer function of a substation will not be known, and the filter design is more complex.

The resonance frequency of the system can be measured based on any TW records made in the substation. This can be a fault record or an energizing record. Energizing records will be preferred in practice, as they can be performed during commissioning.

The solution proposed and used in the rest of this document consists in using the same quality factor obtained in this laboratory test (Q=0.82). This quality factor is coupled with the cut-off frequency f_c computed on the energizing or on fault record of the substation of interest.

Chapter 6

Measurement campaign

Records of TWs generated during a fault are difficult to acquire, even if some TW FL devices are already commercialized. Recording TWs requires a high sampling frequency compared to the measurement devices typically installed in substations. This is expensive, and the owner of those records generally has little incentive to share them.

The lack of actual records of TWs generated during a fault in overhead lines hinders research on the subject. Those records are useful to improve

the understanding of the TWs behaviour in the power system, and the effect of the substation measurements. This effect of the substation measurements, analysed in chapter 5, can affect the precision of TW FL algorithms.

Fault records are also important to test and validate algorithms on real cases. Without this, the development of algorithms must be based on simulations only.

A measurement campaign has been performed in the transmission network with the agreement of the Belgium TSO. It aimed at acquiring records suitable to the TW FL studies during faults, and during the energizing of a line. Those records must be two-ended with a good time synchronization, and have high sampling frequencies.

The campaign included a preparation time during which the equipment was tested in laboratory. These tests were needed to develop an equipment both suitable for TW recording, and satisfying to the TSO requirements. After the installation, it took a little over one year to record a two-ended, synchronized fault record.

This chapter first describes the measurement campaign, the topology of the line monitored, and the measurement equipment used. The useful records acquired are then listed, described and illustrated. The propagation speed in the monitored line is computed with the help of the energizing records, and the fault records are analysed in detail.

The analysis performed illustrates the type-D algorithm updated for non homogeneous lines. It also shows that the type A algorithm can be used to validate and improve the fault location precision, but that recognizing the first reflection on fault point from other events in the network is difficult.

The analysis also confirmed and illustrated the effect of MTs. Notch filters were successfully designed to cancel their unwanted effects on the current records, but are not trivial to design.

It comes out from this analysis that current measurements are more suitable to TW FL algorithms. It also comes out that CTs significantly affect the shape of the current waves recorded, and should be taken into account in the design of TW FL algorithms.

These findings are used to improve the simulation tools in the following chapter, by modelling the current measurement systems. The synchronized fault acquired is then used in Chapter 8 to validate the FL algorithm with a real case.

The results from this measurement campaign and the following analysis from Part II has led to the development of prototypes to be installed. The

analysis from this measurement campaign will be continued based on the records from those prototypes.

6.1 Measurement campaign description

6.1.1 Monitored line

A 70kV overhead line was monitored during the measurement campaign. It has a particular topology, displayed in Figure 6.1. The measurements are taken at both ends of the line, in substations A and B. The currents are recorded flowing inside the line.

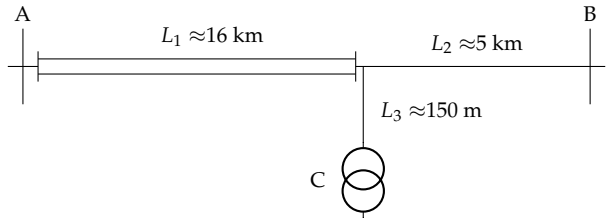

FIGURE 6.1: Topology of the 70kV line monitored during the measurement campaign in the Belgian transmission system. L_1 =15.882 km, L_2 =5.284 km, L_3 =165 m.

The line contains a T-junction. The additional line connected at this junction is very short (165 m) and is connected to a power transformer in C, which acts as an open circuit for TWs. In addition, the line is non homogeneous. The first section of the line is a parallel line, while the second section consists in a single line. The propagation speed in each line section is therefore different, which affects the fault location (see Section 2.2.3.

The line choice was done purely for statistical reasons. This line is the Belgian transmission line which has the highest fault rate, with an average of 4/year. The unique topology was therefore not part of the decision process, but provided an interesting additional challenge.

Substation equipment

The following MTs are used in each substation to reduce the signals levels:

- Inductive voltage transformers. Ratio: $70kV/110V$.
- Iron-core current transformers. Ratio 800/1.

- Secondary cables 'H07V-U4mm' [62] connected to the CTs.

Non-available information

It is not possible to model the line precisely because the following information is not available:

- The geometry of each line section
- The length of the secondary cables in each substation

6.1.2 Measurement systems

Two measurement systems were installed in parallel in each substation. They are redundant, which improves the reliability to record the faults occurring on the line. Due to their different trigger mechanisms, all events were not recorded with both systems. The systems were chosen so that they satisfy the requirements to record TWs, and the constraints associated with the use of the TSO substations (Table 6.1).

Requirements
Sampling frequency: higher than 1MHz
Time synchronization: 1 μs precision or better
Suitable trigger

Constraints
Non-intrusive probes
Storable or remotely accessible data

TABLE 6.1: Measurement systems requirements and constraints.

The first measurement system is based on a digital oscilloscope, the Picoscope 4824 [64]. It is triggered by the substation fault recorder.

The second measurement system is a commercialized TWFL designed by ISA, the TFS2100E [10]. It triggers when the high frequency components of the recorded signals exceeds a pre-set threshold, and doesn't require the use of an external trigger.

Picoscope system

The Picoscope measurement system is displayed in Figure 6.2, and the devices characteristics are provided in Table 6.2. The equipment is synchronized using GPS antenna, and the trigger is provided by the substation fault

recorder. This means that the equipment is dependent on the operation of the fault recorder to record events occurring on the line.

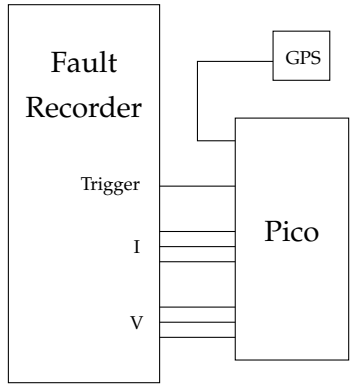

FIGURE 6.2: The Picoscope measurement system depends on the fault recorder for the trigger.

Records	1s window 16 MHz sampling frequency
Picoscope 4824	20MHz bandwidth
Current probe CWT1N	25Hz - 10MHz bandwidth
Voltage probe TT SI9001	DC-25 MHz bandwidth
GPS antenna	100 *ns* precision

TABLE 6.2: Picoscope equipment characteristics.

TFS2100E system

The characteristics of the TFS measurement system is displayed in Table 6.3. The three voltages and currents are recorded, and synchronized with the same GPS antenna than the Picoscope system.

The device triggers directly on the high frequency component of the recorded signals. Four factors affect the shape of the waves recorded:

- An internal bandwidth
- The current records of phase A are sometimes incorrect due to a defect in the device.

- The magnitude of the waves recorded is not available
- Saturation is present on the records

Due to these unwanted effects, this system is not used to analyse the wave shapes, but to record the arrival times of TWs only.

Records	4ms window
	6 MHz records
	Internal HF trigger
	Unknown measurement tools
Limitations	Internal bandpass filter
	Incompatible simultaneous V and I records
	Unknown measurement values
	Measurement saturation

TABLE 6.3: TFS equipment characteristics.

6.1.3 Useful records acquired

An overview of the records illustrated and analysed in the following sections is provided in table 6.4. More records were acquired and analysed during the campaign. Those records, along with a small description of the practical and technical challenges that occurred during the campaign, are presented in Appendix D.

Event	Description	Station A	Station B	devices
1	Line energizing	X	X	TFS
2	Line energizing	X	X	TFS
3	Fault	X	X	Both
4	Fault	X		Pico

TABLE 6.4: 4 events recorded during the measurement campaign are analysed in this chapter.

The line energizing events cannot be recorded with the Picoscope systems, because the fault recorder does not provide a trigger for these events. The equipment from substation B was removed when event 4 occurred. This event was therefore only recorded in substation A.

6.2 Records

In this section, the records are illustrated with figures highlighting the important parts of the records. The complete Figures of the records are displayed in Appendix D.

6.2.1 Event 1: Line energizing of substation A

Event 1 is the re-energization of the line in substation A after a fault occurred. It was recorded by the TFS systems. The voltage measurements were not taken in substation A, and the current waves are not observable in substation B due to the reflections on the open circuit.

During the energization, all phases are not closed simultaneously. In this event, only the waves generated during the closing of phase C are distinguishable due to the measurement saturation. Figure 6.3 shows the propagation of those waves.

Event 1 description
TFS records
2-ended, time-synchronised
Switching operation
Unavailable substation A voltages
Unavailable substation B currents

TABLE 6.5: Characteristics of the records from event 1.

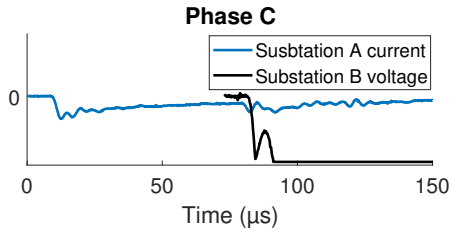

FIGURE 6.3: Propagation of waves generated during the closing of phase C. Event 1, unknown magnitudes.

This record, together with event 2, is used to compute the propagation speed in each line section of the monitored line in Section 6.3.

6.2.2 Event 2: Line energizing of substation B

Event 2 is the intentional energization of the line made by the TSO in substation B. It was recorded with the TFS systems. The voltage measurements in substation B are saturated, and the current waves are not observable in substation A due to the reflections on the open circuit.

The waves generated during the successive closing of all three phases are observable in this event. This record, together with event 1, is used to compute the propagation speed in each line section of the monitored line in Section 6.3.

Event 2 description
TFS records
2-ended, time-synchronised
Switching operation
Unavailable substation A currents
Unusable substation B voltages

TABLE 6.6: Characteristics of the records from event 2.

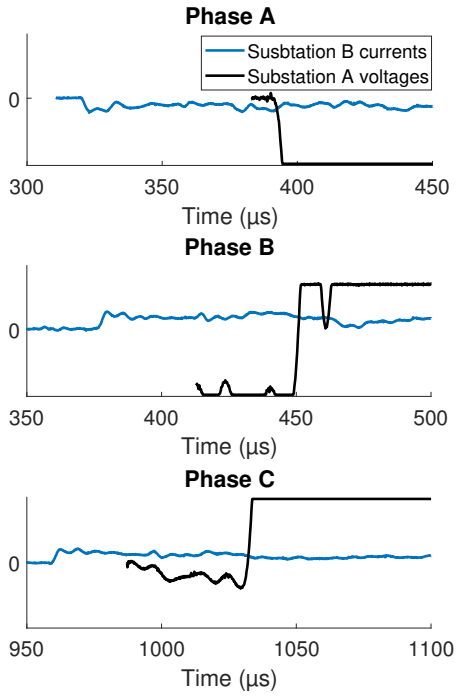

FIGURE 6.4: Propagation of waves generated during the closing of each phase. Event 2, unknown magnitudes.

6.2.3 Event 3: Single phase to ground fault (2-ended)

Event 3 is a single phase to ground fault that occurred in the monitored line. It was recorded by both Picoscope systems, and by the TFS device in substation A. The analysis provided by the TSO (based on the 50Hz impedance [1]) is available on table 6.7. The approximative fault location is displayed in Figure 6.5, and the fault records are available on Figure 6.6.

This record is analysed in Section 6.4. It is also used to compare the same event recorded with each measurement system in Appendix D. It is then used in Section 7.2 to validate the simulation tool, and in Section 8.2 to apply the fault location algorithm.

Event 3 description
Synchronized Pico records
Phase A to ground fault
Fault location: 8.18 $\pm$ 1.63 km
Fault impedance: 1.17 Ω

TABLE 6.7: Characteristics of the records from event 3.

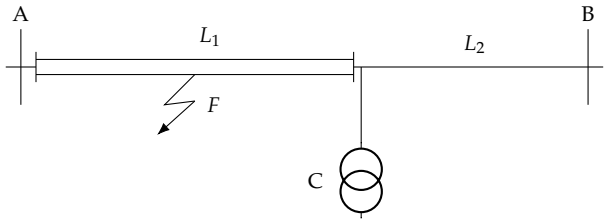

FIGURE 6.5: Approximative fault location of event 3.

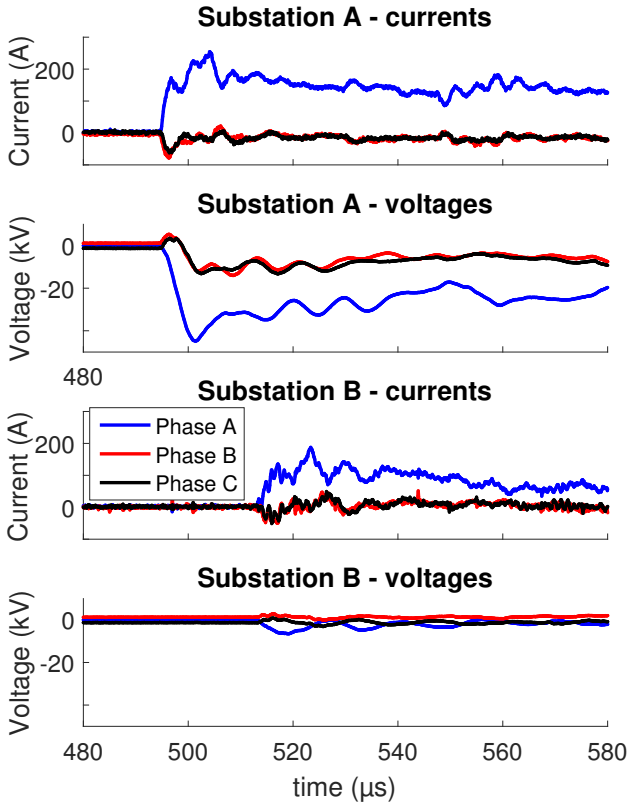

FIGURE 6.6: Signals recorded by the Picoscope systems during a single phase to ground fault (event 3).

6.2.4 Event 4: Single phase to ground fault (1-ended)

Event 4 is a single phase to ground fault that occurred in the monitored line. It was recorded with both measurement systems in substation A only. The substation B equipment was not installed at this time due to constraints from the TSO. The analysis provided by the TSO is available in Table 6.8.

Because event 4 is only a one-ended record, it cannot be analysed as extensively as event 3. It is used in Section 6.4 to compare the records of successive events in the same substation.

Event 4 description
Substation A Pico and TFS records
Phase C to ground fault
Fault location: 9.56 $\pm$ 2.42 km
Fault impedance: 0.77 Ω

TABLE 6.8: Characteristics of the records from event 4.

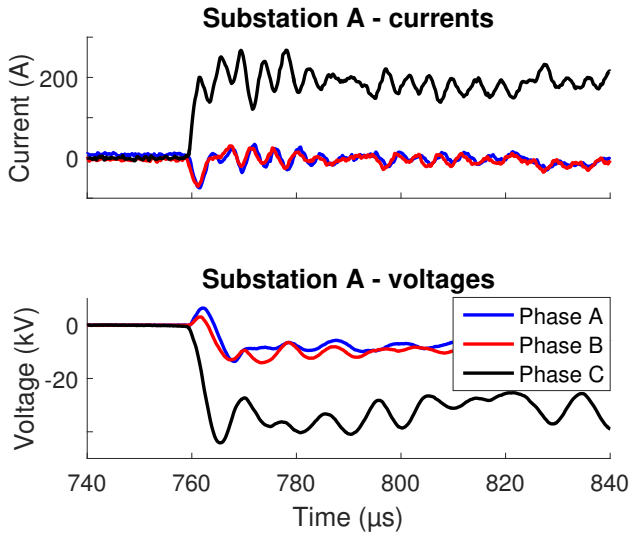

FIGURE 6.7: Event 4: Signals recorded by the Pycoscope system in substation A during a single phase to ground fault.

6.3 Propagation speed

The line energizing records acquired (events 1 and 2) are used to compute the propagation speed inside each section of the monitored line. Because the line is non homogeneous, it is not trivial to determine the propagation speed in each line section. The methodology proposed in Section 3.3.2 is used: the propagation speed in one line section is assumed. Due to the low variability of v in single overhead lines (see Section 2.2.3), the propagation speed in this line section is assumed with a standard value.

Total propagation time

The total propagation time was measured 4 times. Three distinct waves are generated and observed in event 2, when the phases are closed non-simultaneously. Only one phase is usable with event 1, due to the saturation present on the records. The total propagation times measured are available in Table 6.9.

Event	Total propagation time (μs)
Phase C (event 1)	71.8
Phase A (event 2)	72.3
Phase B (event 2)	71.9
Phase C (event 2)	72.5
Average	72.125

TABLE 6.9: Total propagation time measured on the energizing records using a visual inspection.

The total propagation time is averaged as 72.125 μs, with a 0.38 μs range of error on the propagation speed. It is subject to errors caused by the time synchronization, the sag of the line, and measurement errors.

Propagation speeds

If the line is assumed homogeneous, the average propagation speed inside the line is:

$$v_{avg} = \frac{L_1 + L_2}{\tau} = 293.5 m/\mu s \tag{6.1}$$

A 0.38 μs error on the propagation time leads to an precision of $\pm 1.6 m/\mu s$ on the propagation speed. For a medium length line (such as the 20 km monitored line), an error on the total propagation speed measurement significantly

affects the propagation speed computed. The absolute error on the propagation speed measured with regard to the propagation time error is inversely proportional to the line length. To reduce the error on the propagation time measurement, it is preferable to measure this propagation time as an average over multiple energizing records.

If the line is considered as non homogeneous, we must make an additional assumption. We saw in Section 2.2.3 that the propagation speed in single overhead lines do not vary significantly with the geometry. The propagation speed in the single line section is then assumed as a standard value from a typical overhead line [51]:

$$v_2 = 297.8 m/\mu s \tag{6.2}$$

The propagation speed inside the parallel line section is computed with:

$$v_1 = \frac{L_1}{t_{prop} - \frac{L_2}{v_2}} = 292 m/\mu s \tag{6.3}$$

The speed difference in both line sections are not far apart. This is a situation where using the fault location updated for non homogeneous lines (3.7) will improve the precision, but assuming an homogeneous line will not introduce a significant error. For this particular fault, the difference between the two algorithms was estimated at 40m in Section 6.4.4.

6.4 Fault record analysis

The records from event 3 allow a clear observation of the TWs generated during a lightning fault, and recorded in substations. A detailed analysis of the fault records is presented in this section, including an application of TW FL equations [66].

6.4.1 Impact of the voltage transformers

We expect from literature (Section 1.7.1) that the inductive VTs significantly affect the TWs recorded.

In our records, we found that the voltage waves were detectable in substation A, but more distorted than their associated current waves. In substation B, the voltage waves are an order of magnitude lower and even more distorted.

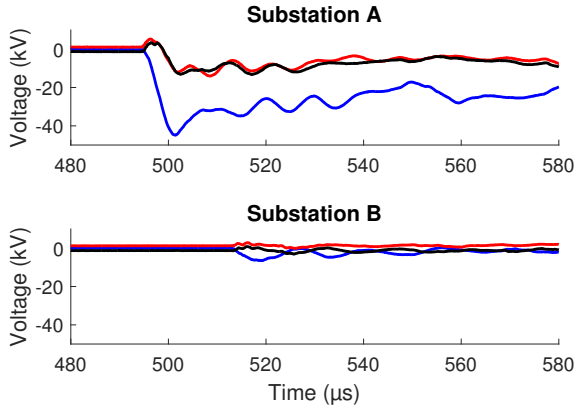

FIGURE 6.8: Voltages recorded in both substation.

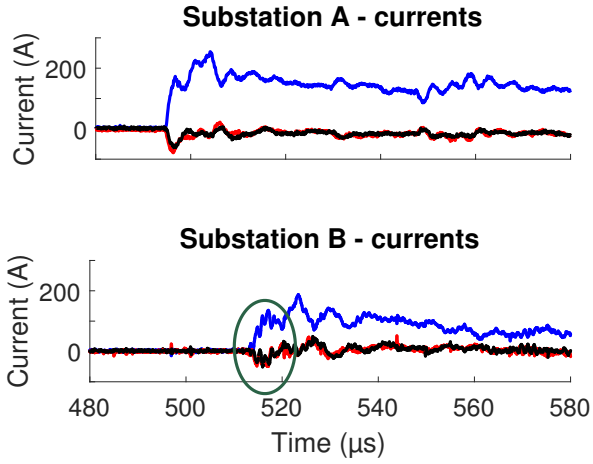

(A) Current waves recorded in both substations.

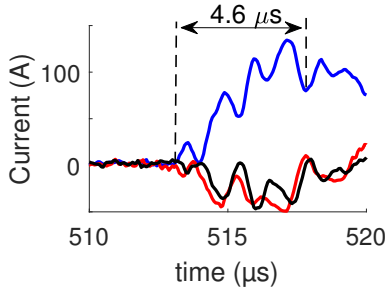

(B) Zoom on the fast reflections caused by the T-junction.

FIGURE 6.9: Effect of the T-junction on the current waves.

The difference in voltage waves in each substation, and the different oscillations present, are not explained by the line topology. We conclude from this that the VTs significantly affect the voltage waves recorded. The VTs bandwidths are different in each substation, which explains the different waves recorded. The rest of the analysis will focus on the currents only.

6.4.2 Reflections on the T-junction

Fast reflections occur on the T-Junction, between the junction and the power transformer in C. These fast reflections are only observable on the records in substation B (Figure 6.9). This is because the fault occurred in section 1 of the line (see Figure 6.5). The first current wave reaching substation A does not go through the junction. The first wave reaching substation B does go through the junction, and its effect are therefore noticeable there.

The reflection period recorded is measured at 1.15 μs (4.6 μs for 4 reflections). With the propagation speed v_2 computed previously, the expected reflection time on the small line section is equal to:

$$T = 2\frac{L_3}{v_2} = 1.11\mu s \tag{6.4}$$

6.4.3 Reflections on the CT secondary cabling

We saw in the literature review (Section 1.7) and during the laboratory tests (Chapter 5) that CTs have a good bandwidth for TWs, but that they introduce fast reflections because of their secondary cabling. These fast reflections are observed on the records (Figure 6.10).

The secondary cable set-up is different in each substation. The reflection periods are therefore also different. However, for two successive events recorded in the same substation, the set-up is the same. The reflections periods are equal (Figure 6.11).

In the records for two successive events, even if the reflection period is the same, the amplitude of the oscillations and their attenuation differ. With just those two records to analyse, we do not have an explanation for those differences.

6.4.4 Fault location

The fault location can be computed using the type-D TWFL equation. When the fault location D is found, the expected arrival time of the first reflection

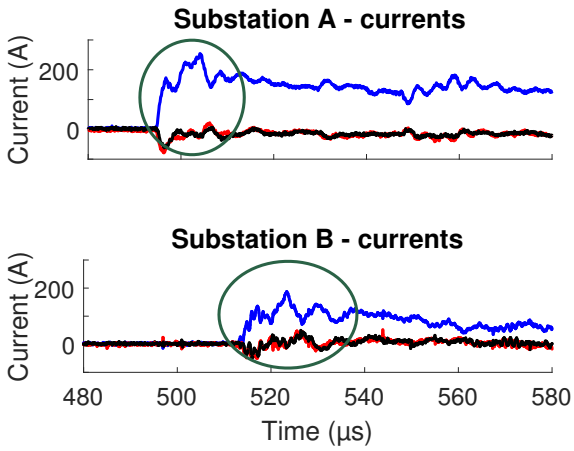

(A) Current waves recorded in both substations.

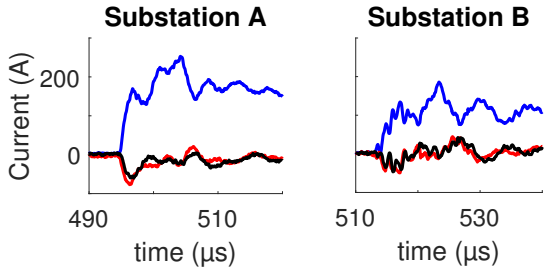

(B) Zoom on the reflections occurring on the CTs secondary side.

FIGURE 6.10: Effect of the current transformers.

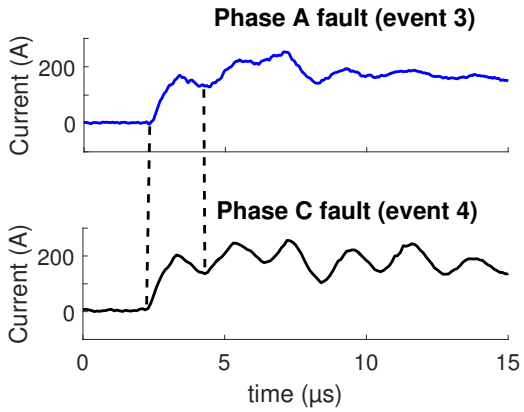

FIGURE 6.11: The reflections on the secondary cables have the same period for successive events, but different amplitudes and attenuations.

can be computed. This reflection is normally hard to recognize, but it can be done based on its expected arrival time. The type A TWFL equation can then be used. This improves and validates the fault location, because the type A equation do not depend on the time synchronization.

Type D equation

The fault location is computed with the type-D equation based on the measurement of Δt, the difference in arrival times of the first TW in each substation (Figure 6.12). If the line is assumed homogeneous, the classical type-D equation can be used:

$$D = \frac{L + \Delta t \cdot v_{avg}}{2} \tag{6.5}$$

Otherwise, the updated equation for non homogeneous lines can be used:

$$D = \frac{L_1 + v_1 \cdot \Delta t}{2} + \frac{v_1 \cdot L_2}{2v_2} \tag{6.6}$$

Those equations are explained in Section 3.1.

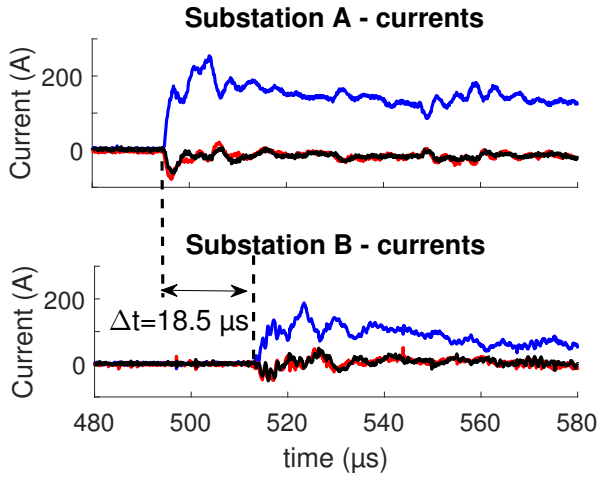

FIGURE 6.12: Type D algorithm applied to the records from event 3.

Table 6.10 shows the result of the fault location using a visual inspection to find the TW arrival times. A correction of 40m is applied when using the updated type-D algorithm for non homogeneous lines.

The correction of 40m might seem like a small value. This is because the speed difference is small, and the fault did not occur close to the junction.

Type D fault location	
TSO fault location	8.18 ± 1.63 km
Δt	$18.5 \mu s$
Type-D	7.87 km
Updated type D	7.83 km

TABLE 6.10: Type D FL equations applied to the fault record.

Type A equation

The fault is computed with the type A equation to remove the time synchronization error. The expected arrival time of the first TW reflected on fault point in substation A is computed with:

$$t_3 = t_1 + 2\frac{D}{v_1} \tag{6.7}$$

Where D is the fault location from substation A, and t_1 is the arrival time of the first wave at substation A.

Type A fault location	
t_1	494.7 μs
Expected t_3	$548.3 \mu s$
Measured t_3	$547.6 \mu s$
Type A FL	7.72 km
Correction	110 m

TABLE 6.11: Type A FL equation applied to the fault record.

In substation A, this reflection can be detected on the currents (Figure 6.13). It is challenging to recognize this reflection from all the other events occurring on the signals, but its arrival time can be used as a validation of the type-D algorithm. The first reflection is not observed on the measurements from substation B. This is due to all the reflections that will occur on the T-junction before the first reflection on fault point is reaching substation B.

The result from the type A equation is presented on Table 6.11. A correction of 110m is applied to the type D fault location.

6.4.5 Notch filter

Notch filters can be designed to remove the effect of the CTs as shown in Section 5.4. The frequency introduced by each CT can be measured on the fault

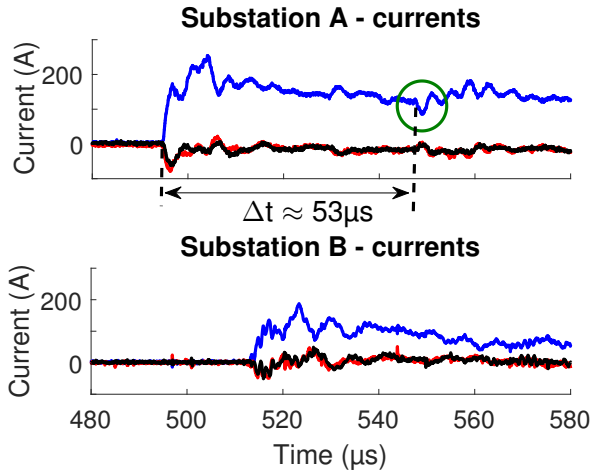

(A) Current waves recorded in both substations.

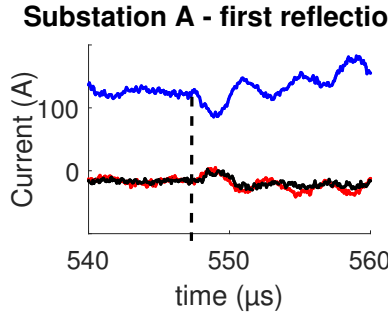

(B) Zoom on the first reflection on fault point.

FIGURE 6.13: Type D algorithm applied to the records from event 3.

records. In our particular case, the reflections introduced by the T-junction can also be measured. They are displayed on Table 6.12.

The design of the notch filter depends on the quality factor Q. We illustrated in Section 5.4 that if this quality factor is too large, the TW itself will be distorted by the notch filter. If it is too small, the oscillations generated by the measurement system will not be attenuated enough.

It is not trivial to design correctly the notch filter without the transfer function of the measurement system. We propose as a solution to this problem to approximate the quality factor Q. It is chosen similarly to the measurement set-up tested in Section 5 (Q=0.82).

Figures 6.14, 6.15 and 6.16 show the result of the notch filters on the recorded

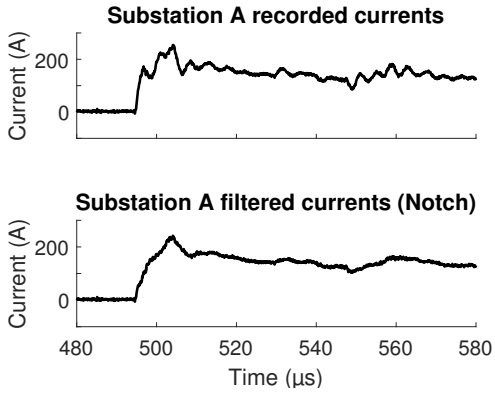

FIGURE 6.14: Notch filter applied to event 3 records

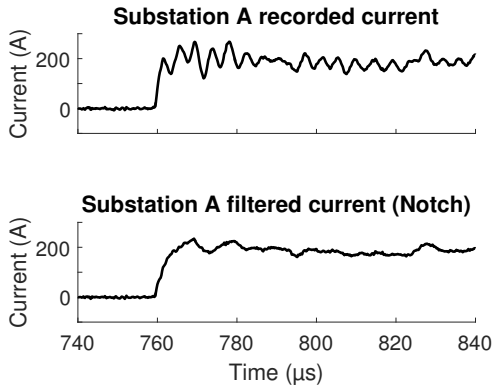

FIGURE 6.15: Notch filter applied to event 4 records.

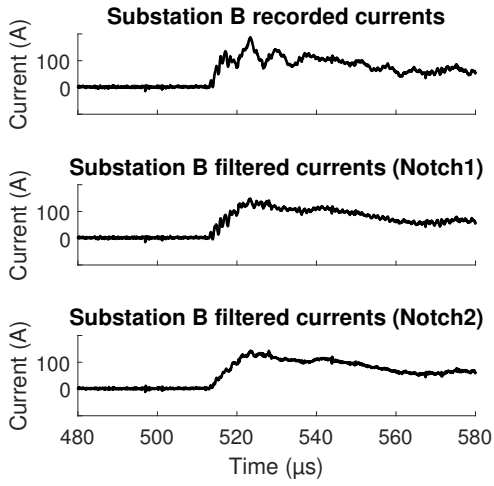

FIGURE 6.16: Notch filters applied to event 3 records.

Substation A CT	240 kHz
Substation B CT	137 kHz
T-junction	851 kHz

TABLE 6.12: Frequencies introduced by the CTs secondary cabling and by the T-junction.

currents for the fault records. The filters reduce the effect of the secondary cable reflections, and slightly distort the incident wave. Figure 6.16 also includes a notch filter to remove the reflections on the T-junction.

6.5 Discussion

The energizing records are used to measure the propagation time, and to compute the propagation speed in each line section. Based on this propagation speed, the fault location is found.

For this particular medium-length line, the error on the propagation time leads to a significant error on the propagation speed. This error, in practice, will be reduced for longer line, or if the propagation time is recorded multiple times.

Even if the monitored line is non homogeneous, the updated type D fault location does not provide a significant correction (40 m). This is caused by the small propagation speed difference in the line sections. The type A algorithm removed the time synchronization error and provided a correction of 110m to the type D algorithm.

The choice of the quality factor is not trivial when designing a notch filter for a given substation. We illustrated that using a standard value for Q, coupled with the measurement of f_c on the records, provides a good first approximation. The filters designed this way reduce the effect of the measurement system.

The records are used to improve and compare the simulation tools in the following Chapter, by modelling the current measurement systems. The synchronized fault record is then used in Chapter 8 to validate the FL algorithm.

Chapter 7

Simulation models

Simulation tools for fast transient studies accurately represent the waves propagation in overhead lines. They often neglect or simplify other elements of the power system, such as the effect of substation measurements (see Chapter 2).

Simulation tools that accurately represent the reality inside a substation are necessary to efficiently study algorithms. In particular, we saw in Chapter 5 that current measurement systems have a significant impact on the records. If those measurement systems are not modelled, the simulation tools will not represent the signals actually recorded in the substation.

The measurement system tested in a laboratory in Chapter 5 is modelled on EMTP, and the model accuracy is assessed with the help of the lab records. This model is included in the complete power system model. The accuracy

of the power system model is also assessed with the help of the fault record acquired in the measurement campaign.

The measurement system model is first presented in this section and compared with the laboratory records. The effect of the model parameters is discussed. The model of the line monitored during the measurement campaign is then presented and compared with the fault record acquired. A select number of case studies are then described. Those case studies have increasing complex topologies and TW effects included, up to two complete models based on line topologies from the Belgian transmission network.

The models analysis shows that the model of the measurement system reproduces the fast reflections occurring on the CT secondary cables. The output of the model, in term of reflection periods and attenuation, is sensitive to its parameters. It is not practically possible to exactly reproduce the effect of a specific substation.

When the substation measurements are added to the model of the complete power system, the simulation tool provides current signals that approach those recorded during the measurement campaign. The overall shape of the TWs are similar, even if small differences are observed.

The power system model does not perfectly reproduce the currents recorded in substations, but provides a better representation when the models of the substations are included. These models will be the subject of further research, based on the fault records that will be acquired by the prototypes from Siemens.

The case studies and the complete power system models presented in this section are used to analyse the pattern recognition algorithm in the following chapter.

7.1 Current measurement system

The current measurement system tested in Chapter 5 is modelled on EMTP, and the results are compared with the lab records. The measurement system can be modelled as a black box (using the transfer function measured), or by modelling each element separately.

The blackbox model is efficient for reproducing a specific substation configuration for which the transfer function has been measured. However, it does not readily allow the modelling of different substation configurations, for which the transfer function would have to be recorded. This is not an easy task to perform on a substation.

The second method is preferred, on which each element is modelled separately. This readily allows the modelling of different substations by changing the parameters of those elements.

7.1.1 EMTP model

The laboratory test set-up is modelled on EMTP (Figure 7.1). The current impulse is modelled as an empirical source. With this empirical source, each sample of the primary current recorded during the laboratory test is input and simulated. This method makes sure that the primary current modelled is the same than the primary current recorded in the lab, removing the error made when modelling the lightning impulse generator.

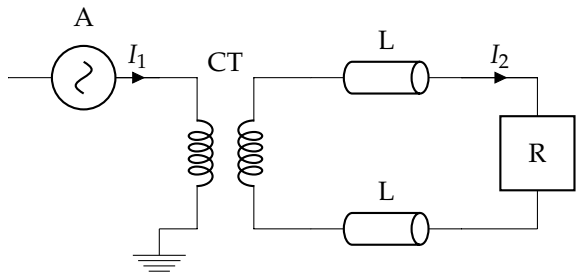

FIGURE 7.1: Simulation model of the lightning impulse test. A: current impulse, CT: current transformer, L: 100m secondary cables, R: protection relay.

We saw in the laboratory tests that the CT itself, when connected to short secondary cables, has a flat bandwidth up to a few 100 kHz. The CT is thus modelled as a perfect 125/5 transform ratio. This ratio will not affect the shape of the current impulse.

The secondary cable is modelled based on its properties and geometry. Table 7.1 displays the parameters used for this model.

The protection relay is modelled as a shunt impedance. The resistance is measured as 0.2 Ω, and a stray inductance of 20 μH is arbitrarily added.

Figure 7.2 compares the model output with the current recorded in the laboratory. The reflections occurring on the secondary cable are reproduced, but the exact reflection period as well as the attenuation of those reflections are not similar.

Parameter	Value
Length	100m
$R_{conductor}$	0.11284 cm
R_{total}	0.19284 cm
Cable Resistivity	$1.6810^{-8}\Omega m$
Insulator relative permeability μ	1
insulator relative permittivity ϵ	3.9
Ground resistivity ρ_0	200 Ωm
Vertical positions	0.19284 cm
Horizontal position (cable 1)	0
Horizontal position (cable 2)	5 cm

TABLE 7.1: Parameters of the secondary cable models - base case.

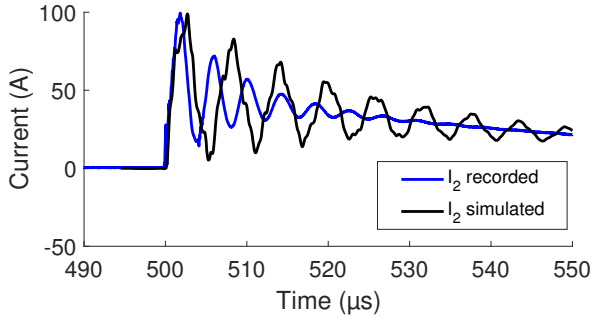

FIGURE 7.2: Simulated currents compared with the recorded currents.

7.1.2 Parameters sensitivity

Three parameters affect the simulation results: the resistance R_{end} and inductance L_{end} of the termination burden, and the physical disposition of the cables.

Figure 7.3 shows the impact of the termination burden resistance. A bigger resistance at the cable end impacts the reflection factors for the current waves. When the reflection factor decreases, it leads to an effective faster attenuation of the oscillations.

Figure 7.4 shows the impact of the stray inductance of the termination burden. Due to this stray inductance, the end of the cable is initially seen as an open circuit, which transitions into an 'almost' short circuit, depending on R_{end} (see Section 1.5.2). Because the stray inductance is small, this transition is fast. When the stray inductance increases, this transition is slower and the current takes more time to rise. This delays the propagation to the second half

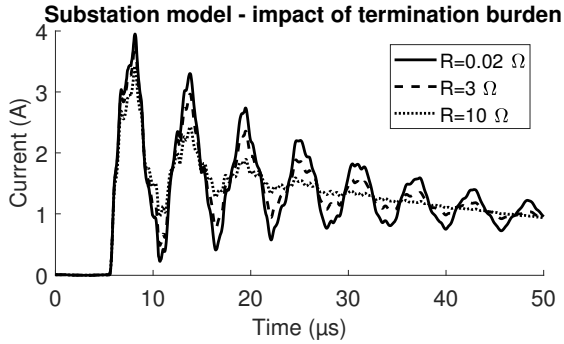

FIGURE 7.3: Simulated secondary currents compared with the recorded currents: impact of R.

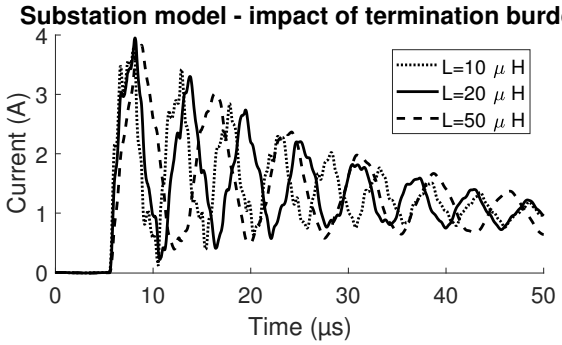

FIGURE 7.4: Simulated secondary currents compared with the recorded currents: impact of L.

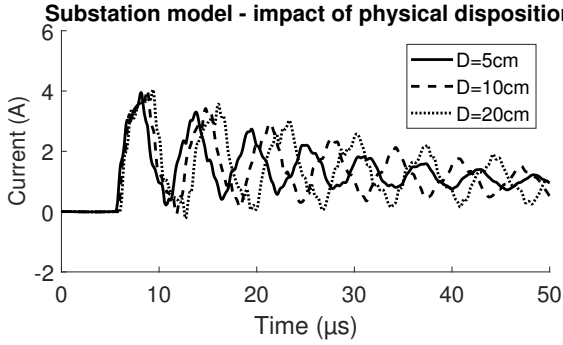

FIGURE 7.5: Simulated secondary currents compared with the recorded currents: impact of D.

of the cable, which leads to an effective slower oscillation of the secondary currents.

Figure 7.5 shows the impact of the physical disposition of the cables. The propagation speed and the attenuation of the oscillations are affected by the distance between the two cables connecting the CT and the protection relay.

7.1.3 Discussion

The fast reflections that occur on the secondary cables, including the attenuation during the propagation and the reflections on the termination burden, are represented with the simulation model.

It is not easy to obtain an exact model of one particular substation. This would require the knowledge of the exact geometrical disposition of the cable (which may not be constant) and a precise measurement of the termination burden. Both of those parameters are shown to strongly affect the propagation speed and the attenuation of the reflections in the simulation model. In addition, the CT model should be investigated. The approximated perfect CT model used affect both the wave propagation in the secondary cables, and the reflection factors on the CT.

It comes out from this analysis that the secondary cable ripples can be qualitatively modelled. With it, the simulation models provide current signals similar in shape to what is actually recorded in a substation. The parameters of the substation models can arbitrarily be changed so that the reflection periods and attenuations differ in each substation.

7.2 Power system

The power system is modelled based on the literature review described in Chapter 2, and improved by adding the substations model presented in the previous section. The focus is put on the current measurements, and the voltage measurement systems are not included in this model.

7.2.1 Model

The topology of the line monitored during the measurement campaign is reproduced, and the simulation results are compared with the fault records acquired. Figure 7.6 displays the topology of the line and each element modelled in EMTP.

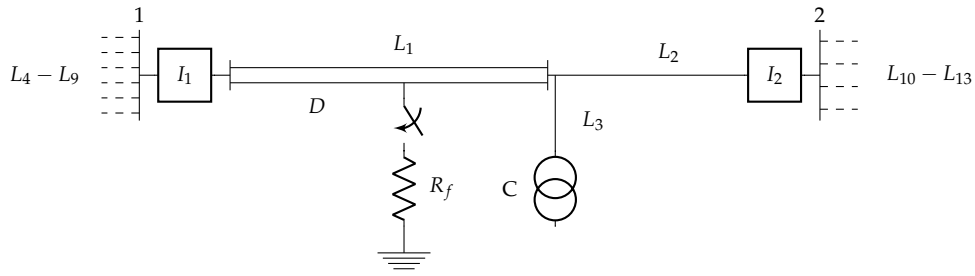

FIGURE 7.6: Model of the line monitored during the measurement campaign.

Line section 1 is a parallel line, and line sections 2 and 3 are single lines. Their geometry was not provided by the TSO. The parameters used for the single and parallel line models are available in Appendix B. The lengths of each line and line section are presented in Tables 7.2 and 7.3.

The fault is modelled as an instantaneous switch to a constant resistance $R_f = 0.1\Omega$. The power transformer in C is modelled as an open circuit. The external lines connected to substations 1 and 2 are terminated with a lumped resistance of 50Ω.

Line	Length (km)	type
L1	16.1	parallel line
L2	5.3	single line
L3	0.165	single line

TABLE 7.2: Lengths of the different line sections.

	L4	L5	L6	L7	L8	L9
Length (km)	3.3	12.1	13.2	16.1	16.1	22.5

	L10	L11	L12	L13
Length (km)	20.9	9.8	9.9	9.9

TABLE 7.3: Lengths of the external lines connected to the monitored line.

The substation measurements I_1 and I_2 are modelled as presented in Table 7.1. The parameters used in each substation are available in Table 7.4. A longer length is chosen for substation 2, to reflect the longer reflection periods recorded on this substation during the measurement campaign.

Element	Value
CT ratio	400/1
R_{cond}	1.1284 cm
R_{tot}	1.9284 cm
Resistivity	$1.6810^{-8}\Omega m$
μ_{ins}	1
ϵ_{ins}	3.9
phase distance	5 cm
R_{burden}	10Ω
L_{burden}	$20\mu H$
Length (station A)	50 m
Length (station B)	75 m

TABLE 7.4: Parameters of the CT and secondary cables modelled.

7.2.2 Results

The results are presented in Figure 7.7, and compared with the fault record. Two main differences are observed between the records and the simulation results.

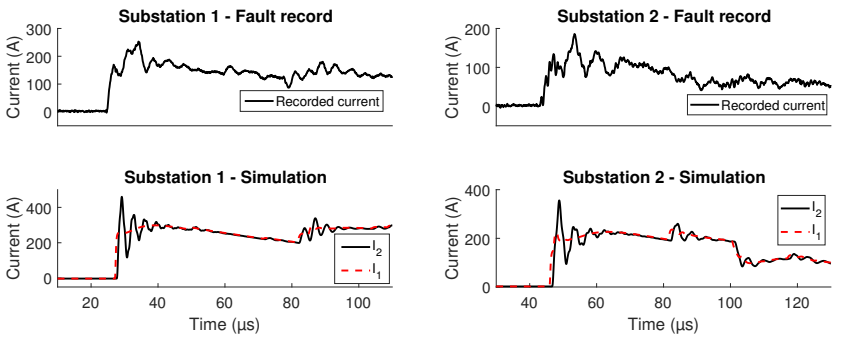

FIGURE 7.7: Comparison of the faulted phase recorded and simulated.

The first difference concerns the secondary cable ripples. In the fault records, the first reflection occurring on the CT secondary cables reaches a higher amplitude than the incident waves. This is not observed in the laboratory tests, and does not occur with the simulation tool. This difference is currently not explained. A similar discrepency between simulation and field records is observed, but not discussed, on the fault record presented in [13]. This effect however does not appear in the energizing record from [23] (see Section 1.7.2).

The second difference concerns the reflection factors in the power system. These reflection factors on the substations and on the T-Junction differ in the model from the real system. The lines are modelled using a typical geometry from the literature, and differ from the actual lines. Due to this, the polarity of the reflections are not similar. Additionally, the reflections on the small 165m line connected to the T-Junction are less significants and do not disturb the substation 2 signals in the model.

Aside from these differences, the model better approaches the shape of the current waves recorded in a substation, compared to the primary signals when the measurement systems are ignored. They offer a suitable way to test FL algorithms for different lines and situations.

7.3 Case studies

Different case studies are used to analyse the pattern recognition algorithm. They include increasingly complex topologies and TW properties. They are described in this section, and used in the following chapter to study the pattern recognition algorithm. All models are simulated with a time step of 0.0625 μs, representing a sampling frequency of 16 MHz. The key models parameters necessary to understand the wave shapes are provided in this section. A complete description of the models (including the lines geomtery) is available in Appendix B

7.3.1 Effect of topology - Bergeron models

The first set of models use the Bergeron line models, which do not take attenuation and distortion into account. They are used to analyse the effect of the line topologies only.

Model 1: Reflections on lumped Thevenin resistance

In the first model, the reflections on each substation are modelled with a Thevenin equivalent. The substation signals are therefore not disturbed by any event outside of the monitored line.

In model 1a, the end resistances have the same value as the characteristic impedance of the line. The line behaves as if no reflections occurred in the substations. This model represents the ideal situation, and will be used as a base case for the algorithm.

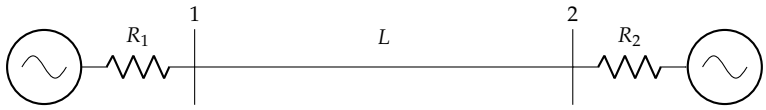

FIGURE 7.8: Model 1: topology.

In model 1b, the end resistances are different in each substations. This leads to different reflection factors in each substation. This model is used to analyse the impact of the wave reflections between the substations and the fault point.

Model 2: Including an external line

In the second model, an external line L_2 is connected to the monitored line L_1 (Figure 7.9). It is used to analyse the impact of the reflections that occur at the end of this external line and disturb the substation signals.

FIGURE 7.9: Model 2: topology.

Model 3:Including a T-Junction

The third model includes a T-Junction inside the line. The reflections on the junction, and at the end of the line connected to this junction, will affect the signals reaching the substations. This model is used to analyse the impact of this junction on the algorithm.

7.3.2 Effect of wave properties - No outside reflections

The second set of models is used to analyse the effect of the wave properties and measurement systems on the algorithm precision. To avoid any effect of the elements outside of the monitored line, the reflections on each substations are modelled with Thevenin equivalent resistances.

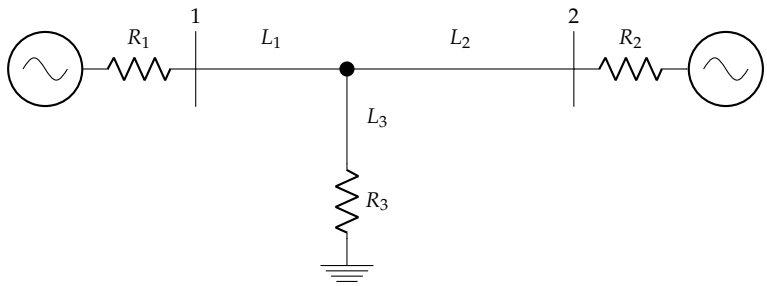

FIGURE 7.10: Model 3: topology.

Model 4: Including substation measurements

Model 4 includes the current measurements inside the substations. It uses the same topology and parameters as model 1a, with the added substation models.

The substation parameters are displayed in Table 7.8. They are chosen such that the measurement systems have a different effect in each substations: the cables length and termination burdens are different.

This model is used to study the impact of the measurement systems on the algorithm precision, and to assess the benefit of using notch filters.

Model 5: Attenuation and distortion

Model 5 uses the same line topology as model 1 (Figure 7.8). A J-marti model is used to represent the line. This introduces attenuation and distortion in the model. The model is used to analyse the impact of the distortion on the algorithm precision.

7.3.3 Complete overhead lines

The last set of models include all the effect previously mentioned. They intend to reproduce real overhead lines, including the current measurement systems. They are based on the topology of two lines from the Belgian transmission network. Those models are used to test the algorithm precision for a complete model, including all the sources of error previously mentioned.

Model 6: Long homogeneous line

Model 6 is a long homogeneous line (Figure 7.11). The important information are displayed in table 7.10.

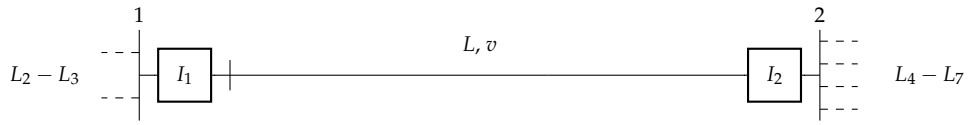

FIGURE 7.11: Model 6: topology.

Model 7: Medium non-homogeneous line

Model 7 is based on the line monitored during the measurement campaign. The T-junction has been removed from the model, and the difference in substation measurement systems have been increased.

The important information are recapped in Table 7.11, and the line topology is shown on Figure 7.12.

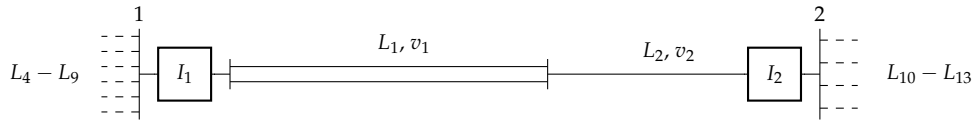

FIGURE 7.12: Model 7: topology.

	Fixed data			Model 1a		Model 1b	
Element	L	v	Z_c	R_1	R_2	R_1	R_2
Value	65km	297 $m/\mu s$	250Ω	250Ω	250Ω	400Ω	100Ω

TABLE 7.5: Model 1 parameters

	Model 2 data					
Element	L_1	L_2	v	Z_c	R_1	R_2
Value	65km	2km	297 $m/\mu s$	250Ω	400Ω	100Ω

TABLE 7.6: Model 2 parameters

	Model 3 data							
Element	L_1	L_2	L_3	v	Z_c	R_1	R_2	R_3
Value	25km	40km	5km	297 $m/\mu s$	250Ω	400Ω	100Ω	600Ω

TABLE 7.7: Model 3 parameters

	Substation 1			Substation 2		
Element	Cable length	R_{end}	L_{end}	Cable length	R_{end}	L_{end}
Value	50m	10Ω	$20\mu H$	100m	3Ω	$40\mu H$

TABLE 7.8: Substations parameters. Used in models 4, 6 and 7. Cables information available in Table 7.1.

	Model 5 data		
Element	L	R_1	R_2
Value	65km	250Ω	250Ω

TABLE 7.9: Model 5 parameters.

	Model 6 data	
Element	L	v
Value	70.9km	297.35 $\frac{m}{\mu s}$

TABLE 7.10: Model 6 parameters.

	Model 7 data			
Element	L_1	L_2	v_1	v_2
Value	15.9km	5.3km	297.35 $\frac{m}{\mu s}$	287 $\frac{m}{\mu s}$

TABLE 7.11: Model 7 parameters.

7.4 Discussion

The substation model presented in this chapter provides a way to qualitatively model the reflections that occurs on the secondary cables of the CTs. The model parameters (termination burden and geometrical disposition) affect the reflection periods and their attenuation.

When the substation measurements are included in the model of the power system, the simulation output better approaches the shape of the current waves recorded during the measurement campaign. The substation parameters are varied so that the measurement effects are different in each substation.

The set of 7 case studies presented in this section include increasingly complex topologies and TW properties, up to two complete power system models based on Belgian transmission lines. They are used in the following Chapter to study the pattern recognition algorithm.

Chapter 8

Pattern recognition algorithm

The fault location algorithm based on pattern recognition was developed and presented in Chapter 4. It is based on building two signals $S_1(t)$ and $S_2(t)$, and assessing their similarities for different time shifts using a LSE. These signals will be exactly similar under specific assumptions. Those assumptions are not realistic for real overhead lines. In practice, different factors (such as distortion and substation measurements) affect the shape of the signals built. Because the signals will not be exactly similar, the LSE introduces an error in the fault location.

The precision of the algorithm is impacted by different sources of error and by the algorithm parameters. To assess and optimize the algorithm's performance, it is necessary to analyse its precision in relation to those sources of error and parameters.

In this section, the pattern recognition algorithm is tested on case studies modelled on EMTP [67]. These case studies include, progressively, the different sources of error influencing the shapes of the signals built. The impact of the parameters for the different situations are highlighted.

Based on this analysis, a set of parameters to use for general situations are proposed. This set of parameters takes into account the practical limitations to record TWs by using the current waves observed at the secondary side of the CTs only. The algorithm is applied to the models of two Belgian transmission lines, and to the fault records acquired during the measurement campaign.

The analysis performed shows that the fault location algorithm has a good precision, even when all the sources of error are taken into account. The largest error arise, on the complete simulation models, for faults located close to one substation. This error is caused by the fast reflections between the substation and the fault point. It appears due to the simplifications applied to the algorithm when the voltage measurements are not available.

When the algorithm is applied to the fault record acquired, it provides the fault location with a precision of 110m.

It comes from the analysis that the pattern recognition algorithm is a good alternative to the FL algorithm based on thresholds. It provides a good precision and removes the need for a small threshold when distortion affects the travelling waves.

The main source of error when using the pattern recognition algorithm comes from the actual limitations when recording TWs in substations. If and when those limitations cease to exist, and perfect measurements of current and voltage TWs are available, the complete algorithm using S_{full} can be applied. This would remove the error introduced by the waves reflected on fault point and on elements external to the line.

While those measurement limitations exist, the algorithm must be based on the current waves only. The algorithm proposed in this project will be further investigated to optimize the parameters, and to compare the performances with other TW FL algorithms. This analysis will be based on the fault records that will be acquired by the prototypes from Siemens.

8.1 Algorithm parameters

The pattern recognition algorithm is applied to the case studies presented in section 7.3. We recall the algorithm parameters:

- The signals that are built (S_{full}, $S_{Reduced}$ or S_I).
- The threshold ϵ used to determine the approximate arrival time of the first wave at one end of the line, t_x.

- The length of the correlation window that will be shifted, on which the LSE will be applied. This correlation window will be surrounding t_x as in: $[t_x - t_a; t_x + t_b]$.
- The band-pass filter used to remove the power frequency as well as the high frequency noises. The filter used in this analysis has cut-off frequencies of 1 kHz and 2 MHz.
- The notch filters used to remove the secondary ripples at each substation

This chapter aims at analysing an algorithm readily applicable to existing substations. The focus is put on studying the algorithm based on the currents only, using the signals S_I with the correction factor. This correction factor, illustrated in section 4.3.3, compensates the effect of the attenuation and reflection factors, so that two signals of similar amplitudes are correlated.

The impact of using the current waves only is first analysed in this section. The different sources of error and the choice of the remaining parameters are then discussed.

8.1.1 Impact of using S_I

Base case

Figure 8.1a shows the signals S_{full}, $S_{reduced}$ and S_I built for the base case. When the algorithm is applied to a simple model, where there is no attenuation, distortion or reflection, the signals S_1 and S_2 are exactly similar, regardless of the assumptions made to build S_I.

Because the signals are similar, the algorithm provides a perfect fault location (Table 8.1). This precision does not depend on the parameters, and is only limited by the sampling frequency, regardless of the parameters.

model 1a - 15 km fault			
	S_{full}	$S_{Reduced}$	S_I
Error:	4m	4m	4m

TABLE 8.1: Fault location error applied to a base case (model 1a).

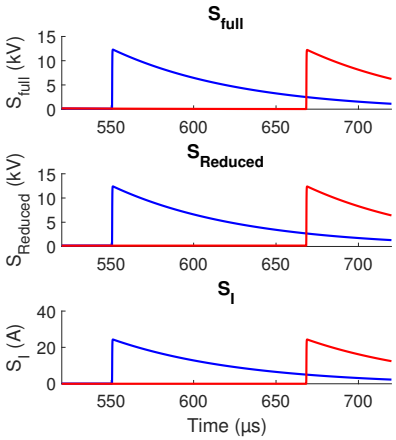

(A) Base case (Model 1a, 15km fault).

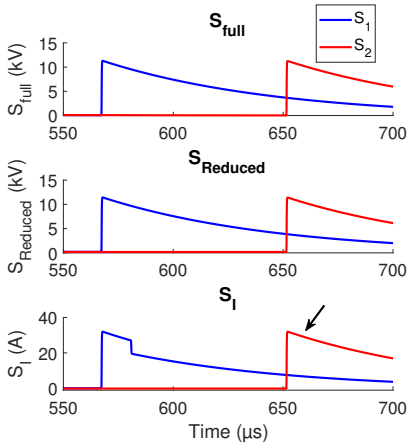

(B) Reflection on external lines impact signals S_I (model 2, 15 km fault).

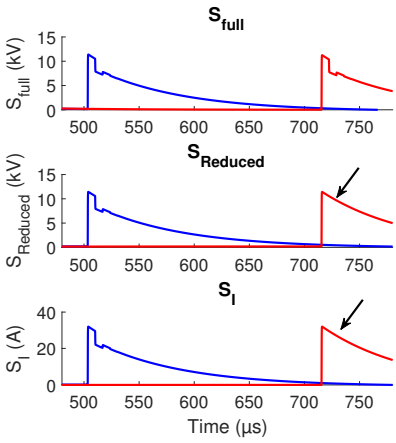

(C) Reflections on fault point impact $S_{reduced}$ and S_I (model 1b, 1km fault).

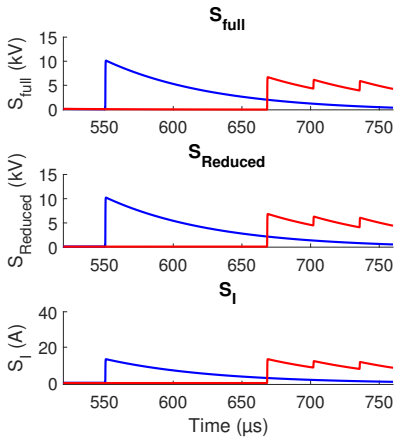

(D) A T-junction inside the line impacts all signals (model 3, 15km fault).

FIGURE 8.1: The signals S_1 and S_2 are affected by the topology and fault location.

Wave reflections

Due to the assumptions made, reflections on elements external to the line affect the signals S_I, and reflections on fault point affect the signals S_I and $S_{reduced}$ (Figures 8.1b and 8.1c). This is explained in Section 4.2.

When the correlation window includes a reflection that affects the signals $S_{Reduced}$ or S_I, two different signals are correlated with the LSE. This introduces an error in the fault location (Tables 8.2 and 8.3). This error depends on the reflection factors in the substations and fault point (if the reflections are smaller, the error introduced will also be smaller).

Model 2 - 15 km fault			
Time window	S_{full}	$S_{Reduced}$	S_I
10 μs	3 m	3 m	3 m
20 μs	3 m	3 m	22 m
30 μs	3 m	3 m	22 m

TABLE 8.2: Fault location error when the waves are reflected on short external lines.

Model 1b - 1 km fault			
Time window	S_{full}	$S_{Reduced}$	S_I
10 μs	3 m	3 m	3 m
20 μs	3 m	12 m	12 m
50 μs	3 m	27 m	27 m
70 μs	3 m	41 m	41 m

TABLE 8.3: Fault location error for a fault close to one substation.

T-Junction

The pattern recognition algorithm was developed by modelling the line as a 4-terminal network. When a T-Junction is included inside the line, this condition is not respected. All the reflections occurring on the junction affect even the signals S_{full} (Figure 8.1d).

Similarly to the previous cases, when the correlation window includes the reflections on the extra line connected to the T-Junction, an error is introduced in the fault location (Table 8.4). In this situation, even the signals S_{full} are affected.

Model 3 - 15 km fault			
Time window	S_{full}	$S_{Reduced}$	S_I
30 μs	7 m	7 m	7 m
50 μs	8 m	8 m	8 m
100 μs	53 m	53 m	53 m

TABLE 8.4: Fault location error when there is a T-junction inside the line.

It should be noted that if the measurements at the third end of the line are available, it is possible to develop and compute new signals $S_1(t)$, $S_2(t)$ and $S_3(t)$ that will be similar but shifted.

Distortion

The algorithm was developed by assuming a distortionless line. In practice, distortion alters the waves. If the fault doesn't occur exactly at the middle of the line, the waves propagate longer to reach one of the substations, on which the distortion will be more pronounced. Due to this, the signals S_1 and S_2 differ (Figure 8.2). This distortion similarly affects the signals S_{full} , $S_{Reduced}$ and S_I.

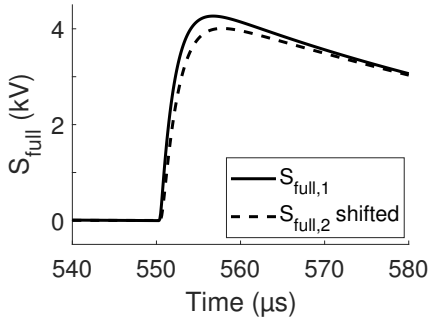

FIGURE 8.2: The signals $S_{full,1}$ and $S_{full,2}$ differ when distortion affects the travelling waves.

The difference between $S_1(t)$ and $S_2(t)$ introduces an error in the fault location. This error is analysed in the following section.

8.1.2 Impact of the correlation window

The correlation window surrounds the approximated arrival time t_x. It is defined by the two times t_a and t_b as in [t_x - t_a ; t_x + t_b].

When there is no distortion, the threshold determines the arrival times t_x precisely. There is no need to start the correlation window long before t_x, and t_b could be very small, because the signals S_1 and S_2 are similar. Of course in this situation, there would be no interest in using the pattern recognition algorithm at all, since the threshold already provides a precise arrival time.

When distortion is included, the threshold only provides an approximated arrival time (Figure 8.3). This impacts the precision of the fault location if the arrival times are determined with a threshold. The precision of the fault location depends on the threshold level (Table 8.5). A small threshold is difficult to apply in practice due to the noise, but provides a better precision.

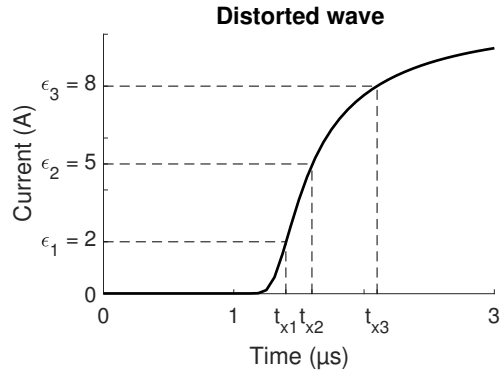

FIGURE 8.3: The error on the arrival times detected with a threshold depends on this threshold value.

Model 4 - 5 km fault				
Threshold level (A)	2	5	8	10
Error (m)	23	66	146	347

TABLE 8.5: Distortion introduces an error in the fault location based on a threshold.

The distortion of the waves introduces a new constraint on the parameters t_a and t_b. If either of those parameters is too small, the error caused by the distortion will be larger. The reason for those constraints is illustrated in Figure 8.4.

If t_a is too small, the correlation window might not include the rising edge of the wave. This introduces a significant error on the fault location.

If t_b is too small only the distorted rising edge of the wave will be correlated with the LSE. The error on the fault location is then larger than if the

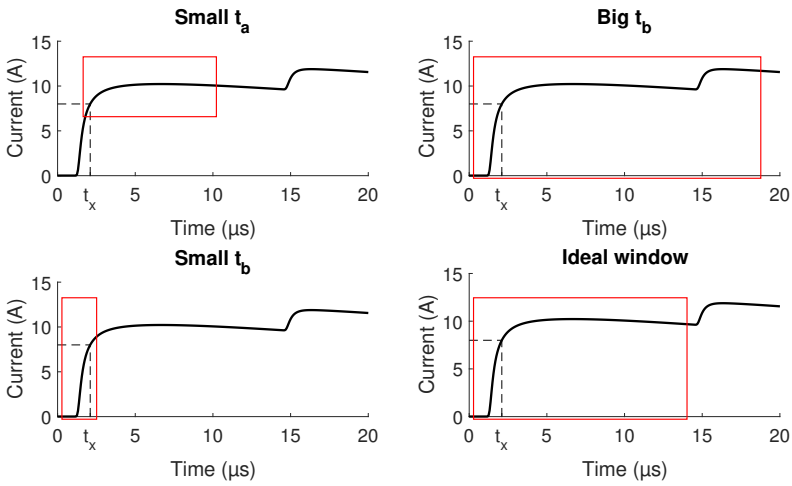

FIGURE 8.4: The choice of the correlation window is affected by the distortion.

rest of the wave is also correlated. If t_b is too big and includes reflections, an additional error is also introduced, as described in the previous section.

The choice of the time window is therefore a trade-off. If the window is larger, the error caused by the distortion is reduced. If the window is too big and includes the reflections on fault point or on external lines, another error is introduced.

Table 8.6 shows the fault location result when distortion is included, for different correlation windows. The reflections do not affect the signals in this model.

		$t_b = 15\mu s$			
t_a	$0\mu s$	$1\mu s$	$2\mu s$	$3\mu s$	$4\mu s$
	167m	105m	49m	49m	49m
		$t_a = 5\mu s$			
t_b	$2\mu s$	$5\mu s$	$10\mu s$	$20\mu s$	$30\mu s$
	67m	61m	49m	49m	49m

TABLE 8.6: Error introduced by the distortion for different correlation window. Model 4, 5 km fault, $\epsilon = 8A$.

Table 8.7 shows the precision of the pattern recognition algorithm for different threshold ϵ, for a well designed time window. The algorithm has a good precision even when distortion is present, and this precision does not depend on the threshold level.

Model 4 - 5 km fault				
Threshold level (A)	2	5	8	10
Error (m)	49	49	49	49

TABLE 8.7: The error of the pattern recognition algorithm does not depend on the threshold. $t_a = 5\mu s$, $t_b = 15\mu s$.

8.1.3 Impact of the measurement system and notch filter

The analysis up to now assumed a perfect measurement of the primary currents. The current measurement systems have two impacts on the signals recorded:

- A time delay is introduced while the waves propagate between the CT and the measurement system.
- The signals $S_{I,1}$ and $S_{I,2}$ are affected differently by each substation.

In model 5, the current waves take 0.5 μs to propagate inside the substation 1 cables, and 1 μs in substation 2. This time difference must be subtracted from the Δt computed by the algorithm. Otherwise, this is added as a source of error in the fault location.

Figure 8.5a shows the result from the LSE on signals $S_{I,1}$ and $S_{I,2}$ when the substation models are included. The reflections on the secondary cables are different in each substation, and an error is made with the LSE.

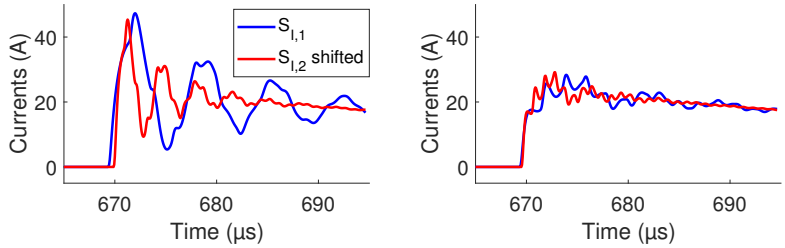

(A) Without notch filters. (B) With notch filters.

FIGURE 8.5: The error introduced in the LSE by the measurement systems is reduced with the use of notch filters.

Notch filters were presented in Section 4.3.4 as a way to decrease the impact of the substation measurements on the current signals. They are used to remove a specific frequency from the signals. They are designed for this model as explained in Section 6.4.5 (Table 8.8).

Parameter	Value
f_{c1}	282 kHz
f_{c2}	144 kHz
Q	0.82

TABLE 8.8: Notch filters applied to the simulation records.

Figure 8.5b shows the result from the LSE when notch filters are applied. The notch filters decrease the impact of the measurement systems, and the fault location precision is improved.

Table 8.9 displays the fault location error caused by the measurement system. The error due to the different propagation times on each substation is completely compensated by the time correction. For very short correlation window, the error introduced by the substation measurements is minimal. This is because the reflections (which are different in each substation) are not correlated. For longer windows, an error is introduced in the fault location. The notch filters efficiently decrease this error.

Model 5 - 15 km fault				
	1 μs	5 μs	15 μs	25 μs
Without time correction	88	227	162	162
With time correction	14	144	79	79
With time correction and notch filter	14	23	23	23

TABLE 8.9: Fault location error when the substation measurements are included.

8.1.4 Discussion

When the different sources of error affecting the pattern recognition algorithm are analysed one by one, the error introduced remains relatively small. We obtained a fault location precision better than 300 m in the worst case from these case studies. When those sources of error are combined, the expected error will increase. For this reason, the investigation on the effect of the parameters is important.

The analysis from this section provides a qualitative feeling of the impact of the parameters. The results from this parameter analysis, for an optimal precision when using the signals $S_I(t)$, can be summarized as:

- The time t_a used to define the correlation window should be large enough to include the start of the wave.

- The time t_b used to define the correlation window should be as long as possible, without including the wave reflections on fault point or on external lines.
- The threshold ϵ does not impact the algorithm precision. It should be small enough to detect the TW.
- The difference in propagation time in each substation should be compensated to remove the error introduced in the measurement of Δt.
- Notch filters designed to reduce the effect of substation measurements improve the precision of the algorithm.

The choice of the algorithm parameters for a particular line will depend on the line topology, on the expected waves amplitudes, and on the substations.

The choice of t_a is simple, since there is no drawback in using a larger value. It should be chosen so that the rising edge of the wave is included in the correlation window. Based on all the records and simulation results presented in this report, we suggest that a value of $5\mu s$ will be sufficient to include this rising edge in the worst cases of distortion on overhead lines.

The choice of t_b depends on the line topology. If a short external line is connected to one of the substations, and significant reflections occur on this line, t_b should be chosen so that those reflections are not included in the correlation window.

The conflict in chosing t_b concerns distortion and reflections on fault point. A larger t_b reduces the error from the distortion, but when the reflections on fault point are included in the correlation window, the error increases. When the fault occurs close to one end, these reflections occur rapidly. In this project, we chose $t_b = 15\mu s$. This value ensures that the correlation will include more than just the rising edge of the wave. With this decision, we must accept an increased fault location error for faults located close to the end of the line.

We propose two solutions to answer the loss of precision for faults located close to the end of the line, which are not studied in this project. The approximated arrival times of the waves at each end of the line (t_{x1}, t_{x2}) are first found with a threshold. Based on them, an expected fault location is computed with a type-D equation. The first proposal is to use this fault location as the output of the algorithm when it is too close to a line end. 'Too close' in this case must be defined in the algorithm. The second proposal consist in choosing the value of t_b based on this approximated fault location.

The notch filters and time correction must be chosen in a case by case analysis, based on the substations. The design of a notch filter for a particular substation was explained in Section 6.4.5. The time correction depends on the length and propagation speed of the secondary cables. These values are easy to know for simulation models. In practical cases, they should be estimated based on the cable lengths.

8.2 Algorithm performance

This section presents the results of the pattern recognition algorithm applied to the complete power system models (case studies 6 and 7), and to the fault record acquired during the measurement campaign (event 3). The parameters, chosen based on the previous analysis, are listed in Table 8.10.

Algorithm parameters	
Threshold	100 A
t_a	5 μs
t_b	15 μs
Signals	$S_I(t)$
Band-pass filter bandwidth	[20 kHz - 2 MHz]
Notch filters	case-by-case
Time correction	case-by-case

TABLE 8.10: Pattern recognition algorithm parameters.

8.2.1 Complete simulation models

The algorithm is applied to case studies 6 and 7 for different fault locations. The algorithm parameters linked to the substations (similar in both models) are available in Table 8.11.

Substation parameters - case studies	
Notch filter substation 1	$f_c = 282$kHz
Notch filter substation 2	$f_c = 144$kHz
Quality factors	Q=0.82
Time correction	0.5 μs

TABLE 8.11: Algorithm parameters relative to case studies 6 and 7.

The FL error of the algorithm, for different fault locations, is presented on Figure 8.6. The fault location of model 7 is determined with the updated type-D equations for non homogeneous lines. The algorithm provides an overall good precision on the fault location, even when all the sources of error are included. For those two case studies, the maximum error on the fault location was lower than 250m.

The largest errors occur for faults located close to one end of the line. This error is caused by the fast reflections between the fault point and the substation. Due to the choice of parameters t_b, those reflections are included in the correlation window and introduce an error in the LSE.

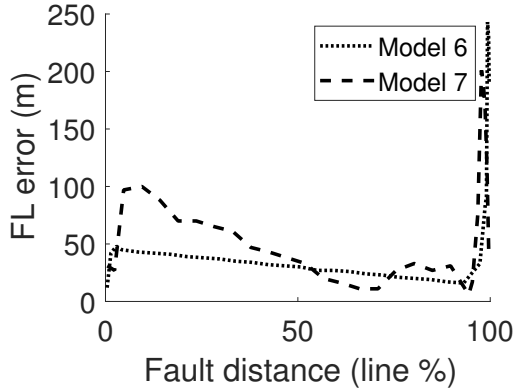

FIGURE 8.6: Error of the FL algorithm applied to case studies 6 and 7.

8.2.2 Application to the fault record

The algorithm is applied to the fault record acquired during the measurement campaign. The algorithm parameters linked to the substations are available in Table 8.12. No information is available on the secondary cable length. Therefore, no time correction is applied to Δt.

Substation parameters - case studies	
Notch filter substation 1	$f_c = 240$kHz
Notch filter substation 2	$f_c = 137$kHz
Quality factors	Q=0.82
Time correction	0 μs

TABLE 8.12: Algorithm parameters relative to the fault record.

The results are shown on Table 8.13. The algorithm introduces an error of 0.75μs in the measurement of Δt compared to a visual inspection, which corresponds to a disparity of 110m in the fault location. Figure 8.7 shows the signals $S_{I,1}(t)$, and $S_{I,2}(t)$ shifted by the algorithm result. The impact of the T-junction on the fault location error is clearly observable.

Algorithm result		
Algorithm	Δt	19.25μs
	FL	7.72 km
Visual inspection	Δt	18.5μs
	FL	7.83 km

TABLE 8.13: Fault location determined with the PRA and with a visual inspection of the field records.

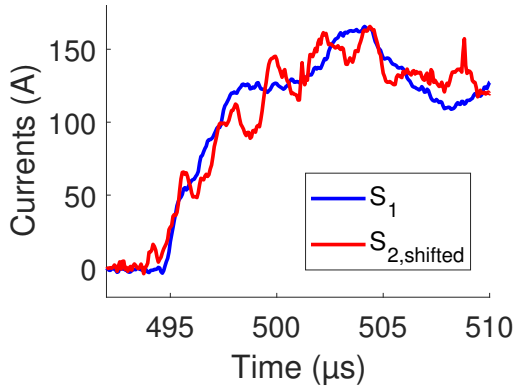

FIGURE 8.7: signals $S_{I,1}(t)$, and $S_{I,2}(t)$ shifted by the algorithm result (fault record - event 3).

8.3 Discussion

The analysis of the pattern recognition algorithm displayed a good overall precision with the proposed set of parameters. The error of the algorithm depends on the line topology. When the line contains a T-junction or short external lines with big reflection factors, the algorithm error is more important.

When all the sources of error are included in the simulation models, the algorithm precision was better than 250m. The biggest errors are obtained

for faults located close to one end of the line. When the algorithm is applied to the fault record, it provides a disparity of 110m for the fault location compared to a visual fault location.

The algorithm error discussed in this chapter relates to the error of the algorithm when computing Δt. In practice, the fault location will contain more sources of error:

- The sampling frequency limits the precision of the algorithm.
- The error on the propagation velocity, discussed in Section 6.3, adds an error in the fault location.
- The error of the time synchronization directly impacts the Δt computed.
- The different propagation times in the substations was discussed. This time difference is not readily available in actual substations. Any assumptions on this time difference introduces an error in Δt.

The pattern recognition algorithm provides a good overall precision, but requires more work during commissioning than a simple threshold algorithm. This is due to the effect of substation measurements on the current waves, which disturbs the LSE. An energizing record on each substation is necessary to measure the frequencies introduced by the secondary cables, and apply the correct notch filter.

The decision to use the current waves only limits the use of the algorithm. For certain topologies, the current waves are not detectable at the end of the line due to the reflection factors. This will be the case when the line is terminated in an open circuit, in a power transformer or with a shunt reactor.

The analysis of the pattern recognition algorithm will be continued. This analysis will be based on the fault records acquired by the prototypes. With more fault records available, the impact of the algorithm parameters should be investigated, and the complete algorithm compared with other FL algorithms.

Conclusion

The work performed is first summarized and related to the project objectives, and the conclusions and contributions are emphasized. Suggestions for further work on the subject are then proposed, on the basis that prototypes are installed and will record faults in different power systems.

Work summary and contributions

The overall focus of this project was to study travelling wave fault locators. The work has been supported by Siemens, with the hope of developing future devices based on the results from this project.

The first objective was to review the subject of TW FLs, and acquire experience in the practical side of TWs and the effect of their measurements. An emphasis was put on the limitations and difficulties to apply TWFL algorithms in practice. The second objective of the project was to use the experience acquired to improve simulation models and study a new wave detection method: the pattern recognition algorithm.

The practical experience was acquired based on a measurement campaign performed with the agreement of the Belgian TSO, and based on experiments performed in a high-voltage laboratory. Records of travelling waves generated during lightning faults were recorded during the measurement campaign, including one 2-ended, time synchronized record. Those kind of records are difficult to come by in the literature, due to the high sampling frequencies and time synchronization needed.

Actual fault records are important to understand the difference between simulation models and substation records of TWs. The records acquired were illustrated and deeply analysed in this report. Each phenomenon observed on the signals recorded was explained based on the line topology and on the literature review. All of the phenomena, except for two, could be explained. The two unexplained phenomena could be investigated with the help of more fault records, and will be mentioned in the following section.

The field records showed, in agreement with the literature, that the CTs have a better bandwidth and are more suitable for recording TWs than VTs. They also showed that a topic seldom discussed in the literature significantly affects the current waves recorded: the secondary cables ringing. The cables connected at the secondary side of the CTs introduce fast reflections on the current waves that are recorded.

Laboratory tests were performed in a high voltage laboratory to reproduce and characterize the secondary cable ringing, and compare the laboratory results with simulation models. Those tests were performed with a medium voltage CT. They show that the impact of adding secondary cables to the CT is a clear resonance frequency introduced in the records.

Based on the laboratory tests, we proposed a solution to reduce the effect of the CTs on the current waves recorded by using notch filters. Those filters were shown to efficiently remove the reflection frequency introduced by the CTs. Their design should be done in a case-by-case analysis for each substation. The study demonstrated that this design is not trivial. A badly designed filter will either not attenuate sufficiently the secondary cables ringing, or distort the travelling wave itself.

The measurement campaign proposed a new challenge due to the monitored line, which is non homogeneous. The typical type-D fault location algorithm was updated for non homogeneous lines. To do so, the propagation speed in different types of overhead lines was analysed. It came out of this analysis that the propagation speed is relatively constant for single lines, but can vary significantly for parallel lines depending on their geometry. The updated algorithm was shown to provide significant improvement on the fault location precision when the propagation speed difference in each line section is important.

The simulation tools were improved by adding the models of the current measurements systems. Those models do not provide a way to precisely model a specific measurement system. They do however provide a qualitative representation of the secondary cable ripples. The inclusion of those measurement systems was shown to improve the performance of the complete simulation tool.

The pattern recognition algorithm was mathematically developed to detect the arrival times of the waves, and tested on the simulation tools and on the fault record acquired. Different sources of error are caused by the assumptions made when developing the algorithm. They were highlighted with different case studies.

The practical considerations when applying this algorithm to real records were discussed. Based on this analysis, a suitable set of parameters was proposed. This set of parameters takes into account the algorithm limitations and the difficulties to record TWs in substations.

When the algorithm is applied to the simulation tools with the proposed set of parameters, it provides a fault location with a precision better than 300m. When applied to the fault record, it provides a fault location with a precision of 110m compared to a visual fault location.

The largest error on the fault location was obtained, on the simulation tools, when the fault is located close to one end of the line. This limitation is directly linked to the choice of the parameters.

Limitations and further work

Although the objectives of the project were reached, it is important to discuss the limitations of the work performed and the possible improvements that can be reached with further work on the subject.

Most of the future proceedings to continue the work of this project is proposed based on the acquisition of more field records. Fault locator prototypes have been developed and installed by Siemens with the intention of recording such fault records. They will offer a good basis to continue the analysis suggested in this section.

The first important point to mention is that most of the present work was either based on, or compared with, the fault records acquired and the laboratory tests. They provide a solid basis to justify our choices, validate the models, and test the algorithm. However, because only two fault records were acquired (including only one 2-ended synchronized record), and only one CT was tested, the knowledge acquired remains somewhat limited.

The CT tested in the laboratory is a medium voltage CT. It is not wise to generalise the results acquired for any type of CTs, including high voltage CTs. More laboratory experiments to test different CTs and different substation configurations would provide an interesting way to quantify the variations in secondary cables ringing that can occur in different substations. It is however expected, based on the fault records acquired and on the literature review, that different types of conventional CTs will provide similar results.

The fault records were acquired for a line with a particular topology. This topology added an interesting challenge, but also introduced a source of error in the fault location. Due to this, the algorithm was not tested for more classical topologies.

In addition to this, because only two records were acquired, and for the same topology, two phenomena occurring on the records were not identified. Namely, the fact that the first reflection on the CT secondary cables reaches a higher amplitude than the incident wave, and the fact that for two successive events, the attenuation of those reflections is not similar. It is possible that the change in attenuation between both events was caused by a change of secondary cable burdens in the substation. More fault records, for different topologies, will help interpreting those effects.

The second point to mention concerns the accuracy of the simulation tool presented. Adding the current measurements to these simulation tools improved their accuracy. However, they do not provide a perfect fit with the fault records, mainly due to the two phenomena previously mentioned. The acquisition of more fault records will also provide a good basis to improve the simulation tools.

Finally, the last point to discuss concerns the performance of the pattern recognition algorithm. The algorithm used with our proposed set of parameters provided a good fault location precision. We showed that it provided one advantage compared to a classical algorithm based on thresholds, which is that the precision does not depend on the threshold value. It was correctly applied to the fault record. The analysis of this algorithm can be continued on three axis:

- Investigate the proposals to improve the algorithm precision when a fault is located close to a line end by using a variable correlation window.
- Test the algorithm for more fault records, and once a significant amount of records are available, investigate the choice of parameters.
- Compare the algorithm performance with different wave detection algorithms, and determine for which situations this algorithm is preferable.

Appendix A

List of reports and publications

Travelling waves theory	November 2013
First simulation results	February 2014
Simulation report	June 2014
First year progress report	September 2014
Susbtation and laboratory measurements (v1)	December 2014
Susbtation and laboratory measurements (v2)	May 2015
Measurement equipment testing	June 2015
Second year progress report	September 2015
Events and algorithm analysis	March 2016
Events and algorithm analysis (update)	July 2016
Third year progress report	October 2016
Powertech 2017 paper [53]	February 2017
IPST 2017 paper [66]	April 2017
PACWORLD 2017 paper [67]	May 2017

Appendix B

Simulation models

In this Appendix, the data used for the simulation models are listed . Figure B.1 shows an example of specified geometry for a line modelled using the LCC routine of EMTP. The type of material used for the conductors is taken into account in the DC resistance. The AC resistance and the other parameters are computed based on the geometry input.

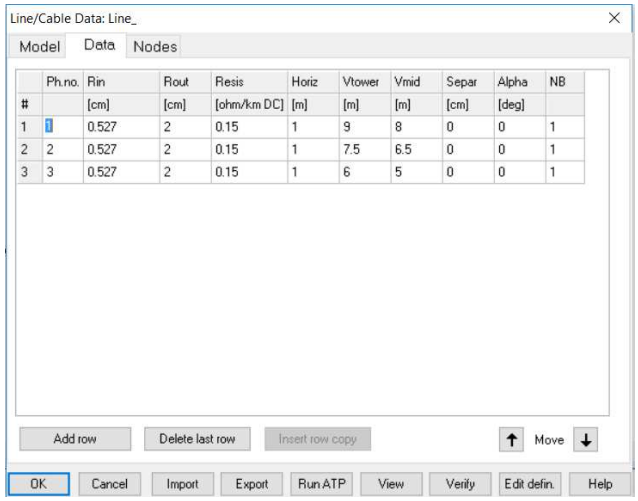

FIGURE B.1: The LCC routine of EMTP computes the line parameters based on the geometry input.

The different lines modelled in this report are based on typical overhead lines found in the literature; their geometry are displayed in Tables B.1 and B.2. They are modelled as fully transposed lines.

A parameter that affects the ground mode propagation is the ground resistivity. Since it doesn't significantly affect the aerial mode propagation used

in this project, this effect was not deeply analysed. The ground resistivity is chosen as 200 Ωm for the overhead lines presented here.

In a Bergeron model, the line parameters are computed at a frequency set by the user; those parameters are assumed constant. In J-Marti models, the parameters are fitted in a frequency range. The modal transform is computed at a dominant frequency set by the user. Due to the frequency dependence of the ground mode parameters, this will mainly affect the ground mode propagation. The modal transform matrix is computed at 250 kHz in the models presented in this section.

Conductors	R_{in} (cm)	R_{out} (cm)	DC resistance (Ω/km)
Overhead line 1	0.218	1.335	0.319
Overhead line 2	0.527	2	0.15
Overhead line 3	0.35	1.06	0.122
Overhead line 4	0.527	2	0.15

TABLE B.1: Conductors specifications of the lines modelled on EMTP. [45, 51]

	Phase	Horizontal (m)	Vertical (m)
Overhead line 1	a	1.75	10
(Single line)	b	0	10
	c	-1.75	10
Overhead line 2	a	1	9
(Single line)	b	1	7.5
	c	1	6
Overhead line 3	a1	2.925	10.35
(Parallel line)	b1	3.5	13.45
	c1	2.675	16.85
	a2	-2.925	10.35
	b2	-3.5	13.45
	c2	-2.675	16.85
Overhead line 4	a1	4.5	9
(Parallel line)	b1	4.5	7.5
	c1	4.5	6
	a2	- 4.5	9
	b2	- 4.5	7.5
	c2	- 4.5	6

TABLE B.2: Geometric disposition of the lines modelled on EMTP. [45, 51]

Frequency-dependent parameters

The analysis of the frequency dependence of overhead line parameters (Section 1.2.4 and 1.6) was performed on the model of 'overhead line 1'. The numeric values are provided in Tables B.3 and B.4.

f	50	200	500	750	1000	2500	7000
R_0 (Ω/km)	0.3	0.73	1.6	2.34	3	7.24	19
R_p (Ω/km)	0.15	0.156	0.183	0.21	0.24	0.37	0.59
L_0 (mH/km)	4.8	4.5	4.2	4.1	4	3.7	3.4
L_p (mH/km)	0.96	0.95	0.95	0.95	0.94	0.93	0.92
v_0 $(m/\mu s)$	195	204	210	214	216	224	233
v_p $(m/\mu s)$	282	290	291.1	291.7	292.3	295	295.9
α_0 (dB/km)	0.0013	0.0035	0.0079	0.0116	0.015	0.038	0.1
α_p (dB/km)	0.0023	0.0024	0.0029	0.0033	0.0038	0.0059	0.0094

TABLE B.3: Line parameters computed at different frequencies.

f	10.000	25.000	70.000	100.000	200.000	350.000	500.000
R_0 (Ω/km)	26.4	61	152	205	364	567	744
R_p (Ω/km)	0.7	1.1	1.88	2.2	3.4	4.87	6.1
L_0 (mH/km)	3.3	3.1	2.8	2.8	2.6	2.5	2.5
L_p (mH/km)	0.92	0.92	0.91	0.91	0.91	0.91	0.91
v_0 $(m/\mu s)$	237	246	256	260	266	272	275
v_p $(m/\mu s)$	296.5	297	297.5	297.6	297.8	297.8	297.9
α_0 (dB/km)	0.145	0.35	0.9	1.24	2.25	3.57	4.73
α_p (dB/km)	0.011	0.0176	0.03	0.037	0.055	0.078	0.01

TABLE B.4: Line parameters computed at different frequencies (part 2).

Attenuation, distortion and speed variability

The analysis performed on Chapter 2 were performed on the model of 'overhead line 1' for the single line, and on the model of 'overhead line 3' for the parallel line. The speed was computed at 250 kHz for the different geometry disposition. The numeric values used to plot the Figures are provided in Tables B.5 and B.6.

ΔR_{out} (cm)	-0.6	-0.4	-0.2	0	+0.2	+0.4	+0.6
v	298.2	298	297.9	297.8	297.7	297.6	297.6
ΔResis (Ω/km)	-0.3	-0.2	-0.1	0	+0.1	+0.2	+0.3
v	298.2	298	297.9	297.8	297.8	297.7	297.6
ΔD (m)	-1	-0.5	0	1	3	5	
v	297.3	297.7	297.8	297.9	297.6	297.1	

TABLE B.5: Variation of the propagation speed with the geometry of 'overhead line 1'.

ΔL (m)	-6	-4	-2	0	2	4	6
v	296.7	295.7	294.6	293.5	292.5	291.7	290.9

TABLE B.6: Variation of the propagation speed with the geometry of 'overhead line 3'.

Substation models

The parameters of the cable used in the laboratory test (Chapter 5) are presented on Table B.7. Those cables are used in the different substation models (Chapters 5 and 7). The length and termination burden specific to the base case from Chapter 5 are presented in Table B.8.

Monitored line and case studies

The monitored line and the case studies use the models of 'overhead lines 2' and 'overhead lines 4'. Their propagation speed was computed at 250 kHz to imput in the fault location algorithm. The specifics for each substation are presented on Tables B.9 and B.10.

Parameter	Value
$R_{conductor}$	0.11284 cm
R_{total}	0.19284 cm
Cable Resistivity	$1.6810^{-8}\Omega m$
Insulator relative permeability μ	1
insulator relative permittivity ϵ	3.9
Ground resistivity ρ_0	200 Ωm
Vertical positions	0.19284 cm
Horizontal position (cable 1)	0
Horizontal position (cable 2)	5 cm

TABLE B.7: Secondary cable parameters - common to all models [62]

Parameter	Value
Length	100m
R_end	0.2 Ω
L_end	20 μH

TABLE B.8: Parameters used in the base case from Chapter 5

Parameter	Value
Length 1	50m
Length 2	75m
$R_{end,1}$	10 Ω
$L_{end,1}$	20 μH
$R_{end,2}$	10 Ω
$L_{end,2}$	20 μH

TABLE B.9: Parameters used for the substations for the monitored line presented in Chapter 7

Parameter	Value
Length 1	50m
Length 2	100m
$R_{end,1}$	10 Ω
$L_{end,1}$	20 μH
$R_{end,2}$	3 Ω
$L_{end,2}$	40 μH

TABLE B.10: Parameters used for the substations for the case studies presented in Chapter 7

Propagation laboratory test

The simulation model used to reproduce the laboratory propagation test of Section 2.2.1 is presented on Figure B.2 and on Table B.11.

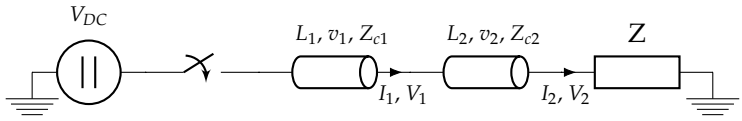

FIGURE B.2: Simulation model used to reproduce the laboratory propagation test.

Element	Value
V_{DC}	50V
L_1	3 m
v_1	200 m/ μs
Z_{c1}	50 Ω
L_2	100 m
v_2	258 m/ μs
Z_{c2}	75 Ω
R_{end}	20 Ω
R_{end}	2.9 μH

TABLE B.11: Simulation model parameters.

Appendix C

Measurement tools

This Appendix describes the measurement equipment used during this thesis. During the measurement campaign (Chapter 6), two independent equipment were installed in parallel to increase the reliability of the records: The TFS device and the Picoscope device. The devices have different trigger mechanisms.

Both systems were continuously connected to a computer, which was remotely controlled via a screen-sharing software. The computer was connected to a 3G hotspot, allowing this remote connection. Each element of the installation was connected to a UPS to ensure a continuous operation of the computer and of the measurement devices.

The laboratory tests presented in Sections 2.2.1 and 5 use the digital oscilloscope 'Picoscope' with the Rogowski current probes 'CWT1N' described under the 'Picoscope device' section.

TFS

The TFS2100E device from ISA is designed to record TWs and find the fault location based on those records [10]. The acquisition unit (TDU 100E) continuously samples the secondary voltages and currents in a circular memory. After trigger, the buffer is sent to the computer. The acquisition unit is time-synchronized by receiving a GPS signal from an antenna (Figure C.1). The equipment triggers on the high frequency component of the current.

The current measurements are taken with small split-core CTs (Figure C.1). Those CTs characteristics are not known, but laboratory tests displayed a flat bandwidth up to the MHz. The acquisition unit itself contains a band-pass bandwidth not specified by the manual.

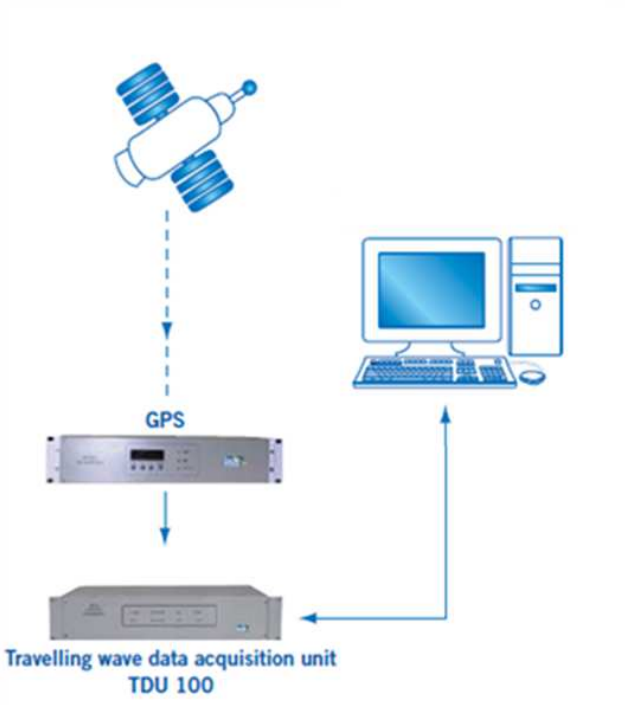

FIGURE C.1: TFS2100E system configuration.

FIGURE C.2: Current measurement CT used by the TFS system.

Picoscope

The Picoscope is an 8-channel digital oscilloscope with computer interface [64]. The equipment is synchronized using GPS antenna, and the trigger is provided by the substation fault recorder on one of the channel. This means that the equipment is dependent on the operation of the fault recorder to record events occurring on the line.

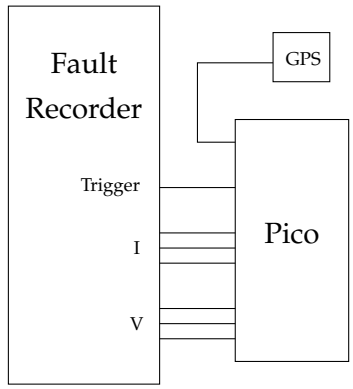

FIGURE C.3: The Picoscope measurement system depends on the fault recorder for the trigger.

FIGURE C.4: Picoscope 4824.

Picoscope

This 12 bits oscilloscope requires a computer to operate. It has a buffer memory of 256M samples. The curves and the values of the samples are directly available on the computer. The user interface as well as the alimentation of the Picoscope goes through the USB cable that connects it to the computer. The Picoscope must therefore continuously be connected to a computer. An alarm system present on the Picoscope interface allows the measurements to be stored in the computer. The measurements are stored as soon as the Picoscope triggers, which introduces a delay of around 1s between two trigger (the time during which the measurements are stored in the computer)

Bandwidth	Input range	Input characteristic	Maximum sampling rate
DC to 20MHz	$\pm 10mV$ to $\pm 5V$	$1M\Omega$	40 MHz

TABLE C.1: Picoscope 4824 characteristics [64].

FIGURE C.5: CWT 1N current probes.

Type	Sensitivity (mV/A)	Peak current (kA)	Peak di/dt (kA/µS)	Noise max[1] ($mV_{pk\text{-}pk}$)	Droop typ. (%/ ms)	LF (3dB) bandwidth typ. (Hz) f_L	Phase lead at 50Hz typ. (deg)	HF (3dB) bandwidth typ. (MHz) f_H [2]	
								Coil Length 300mm	Coil Length 700mm
CWT1N	20.0	0.3	2.0	2.0	20	25	1.9 @ 1kHz	10	5

FIGURE C.6: CWT 1N characteristics [65].

Current probe

The measurement equipment has to be non-intrusive in order to be installed at Elia. A high bandwidth current probe has been selected to perform the current measurements. The CWT1N probe is a Rogowski coil that allows the measurement of both the high frequencies and the 50Hz component. Its sensitivity is not optimal for measurements of the small currents available in the substation, but the tests showed that this sensitivity was sufficient for our needs.

Voltage probe

The voltage measurements are taken with TT-SI9001 voltage probes. Those probes have a bandwidth and a sensitivity suitable for substation measurements.

GPS antenna

The GPS antenna used is included in the TFS package. It has a a precision of 100 ns [10].

FIGURE C.7: TT-SI9001 voltage probes.

Bandwidth	Attenuation ratio	Input voltage	Accuracy
DC to 25MHz	1:10 / 1:100	70V / 700V	$\pm 2\%$

TABLE C.2: TT SI9001 characteristics [68].

Comparison between both equipment

The TFS device has multiple limitations:

- There is an incompatibility between recording both voltage and current waves.
- The measurement values are unavailable
- Saturation is present on the measurements
- An internal bandpass filter limits the high frequencies

Due to these effects, these devices are not used to analyse the wave shapes, but rather to record the TW arrival times. Thanks to its internal trigger based on the HF, this device is able to record the energizing tests. The Picoscope was not able to record them, as the fault recorder does not provide a trigger for those events.

Figure C.8 compares the records acquired for event 4 with each equipment. A band-pass filter (first order butterworth filter, $f_L = 2kHz$, $f_H = 50kHz$) was applied to the Picoscope records to approach the TFS internal filter. This comparison confirms that the both devices correctly record the waves, and the effect of the TFS internal filter.

The incompatibility between current and voltage simultaneous records was not known by ISA, and lead to TW records that could not be understood. This incompatibility was tested a posteriori (Figure C.9).

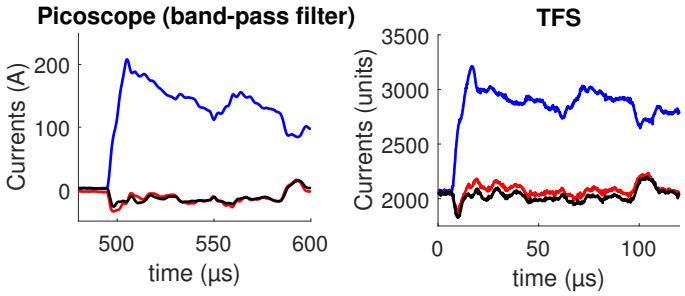

FIGURE C.8: Comparison of records from the TFS device, and from the Picoscope equipment with a band-pass filter applied.

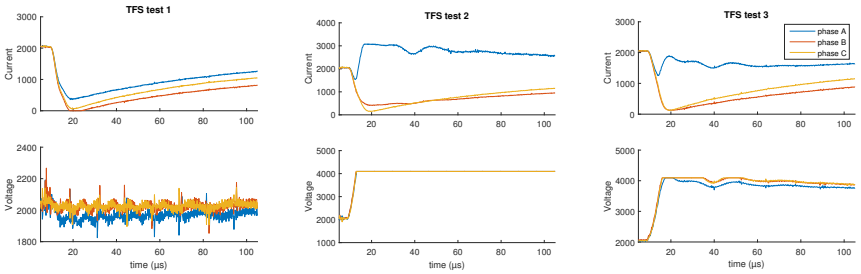

(A) When no voltage is recorded, a very small error is present in I_a.

(B) When a voltage wave is recorded, a big error occurs on I_a.

(C) If the recorded voltage wave is smaller, the error on I_a decreases.

FIGURE C.9: Currents and voltages recorded by the TFS for different tests.

Appendix D

Measurement campaign and lab tests

D.1 Measurement campaign description

The measurement campaign concluded with the fault records presented in the report in Chapter 6. Even if only 4 events were presented, the campaign was a long process that required preparation, testing, installation, waiting times and corrections of unforeseen problems. This section provides a short overview of the complete process.

Planning

Due to the cost of launching the measurement campaign, the first step consisted in securing the possibility to install measurement equipments before designing and acquiring them. After some discussion with Elia, including a decision time on their part, they allowed us to perform a preliminary installation with devices already owned by the ULB.

The preliminary installation was performed in September 2014, with a simplified version of the Picoscope equipment recording only one phase current. After this first experience, where a fault was successfully recorded, Elia agreed to let us install measurement devices in two of their substations. The line chosen was the one with the highest fault rate, at 4/year in average.

Elia gave us some constraints on the devices that we could install in the substations, as well as some external help:

- The device must be non-intrusive.

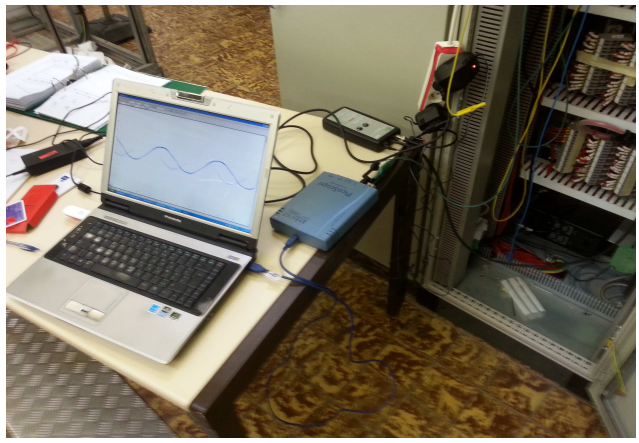

FIGURE D.1: Preliminary installation at Elia (September 2014).

- The device must be able to operate for a long time without human intervention.
- The output from the Fault recorder can be used as a Trigger.
- If a time stamp of the record is available, the event analysis from Elia will be available.

Equipment design and testing

The equipment was chosen and designed to satisfy the request from Elia, as well as the requirements for TWs recording. The equipment is presented in Appendix C.

The installation equipment was tested in a laboratory with the following objectives:

- Ensure the correct operation and the robustness of the equipment
- Test the quality of the measures for small secondary currents
- Verify the time synchronization precision
- Test the remote connection solution using a 3G hotspot
- Verify the trigger mechanisms

Installation and set-backs

Due to the busy schedule of Elia technicians, every trip to the substation required an appointment $\approx$ 2 weeks in advance. A few set-backs delayed significantly the acquisition of fault records:

- The lack of 3G data going through the substation removed our ability to monitor the correct functioning of the devices, leaving us 'in the dark'.
- Some technical problems with the equipment computer delayed the complete installation for a few weeks.
- We discovered during the installation that the TFS device could not record both the voltage and the current waves together, which lead to wrong current measurements for some records.
- The two-ended equipment was first installed in August 2015. No fault occurred during the first 5 months of the installation.
- Elia required the equipment to be removed from one substation for a duration of two weeks; A fault unfortunately occurred exactly the day after the removal and was recorded at one end only.

Many records acquired during the installation were either due to noise or to events outside of the line which did not generate TWs. Their analysis were not useful to the conclusions of this report. The useful records taken during the second part of the campaign are listed on the following table. In addition, 7 records were provided by ISA. The usefulness of those records were limited due to the fact that no information was available on the events nor on the line topology, but provided us, at the time, with a first example of TWs records.

Figures

All Figures presented in the report are the results of a band-pass filter applied to the records acquired. Those filters are used to remove the power frequencies and the lower the noise. It is a first order butterworth filter with a low cut-off frequency of 1 kHz, and a high cut-off frequency of 2MHz.

The line energizing Figures presented in the report are edited to improve their understanding. Full, non-edited versions are presented on Figures D.2 and D.3.

Date	Event	Type of records	Devices
14/01/2016	Line energizing	2-ended	TFS
20/01/2016	fault on the line	1-ended	both
04/06/2016	fault on the line	2-ended	Pico
04/06/2016	Line energizing	2-ended	TFS
06/06/2016	fault on the line	1-ended	TFS
22/07/2016	Fault on another line	1-ended	Pico
Unknown	Fault on the line	2-ended	TFS (ISA)
Unknown	Fault on the line	2-ended	TFS (ISA)
Unknown	Fault on the line	2-ended	TFS (ISA)
Unknown	Breaker operation	2-ended	TFS (ISA)
Unknown	Breaker operation	2-ended	TFS (ISA)
Unknown	Lightning surge	2-ended	TFS (ISA)
Unknown	Lightning surge	2-ended	TFS (ISA)

TABLE D.1: TW records acquired during the project.

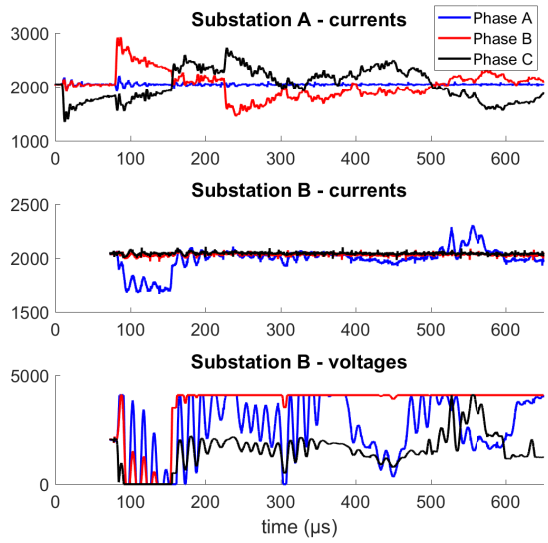

FIGURE D.2: TW records for event 1.

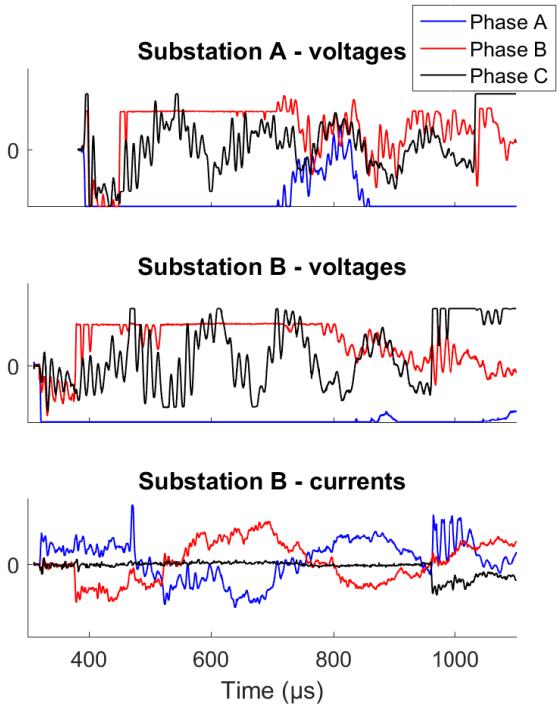

FIGURE D.3: TW records for event 2.

D.2 HV laboratory tests

The laboratory test presented in this report was the conclusion of a longer laboratory session. The results acquired did not consist in a simple, straightforward test. Some intermediate results or challenges did not lead to new conclusions for the project, namely:

- A flashover test was performed in parallel to the lightning impulse test. An increasing voltage was applied to a spark gap, in order to generate a fast transient. These tests did not result in useful records, due to the high EM noise and to the relatively small current generated.
- The tests were performed for different current probes and shunt resistances to compare the results of less accurate probes. Those tests were not conclusive.
- The EM noise also affected the results for the lightning impulse test. It was especially important for the secondary current recorded inside the laboratory, where the noise-to-signal ratio was too important. It took many laboratory session and iteration of Faraday cages to acquire the transfer function presented in this report.

The transfer function presented in Section 5.3.2 was deliberately limited to the frequencies considered significant with regard to the EM noise. The complete transfer function computed is presented on Figure D.4.

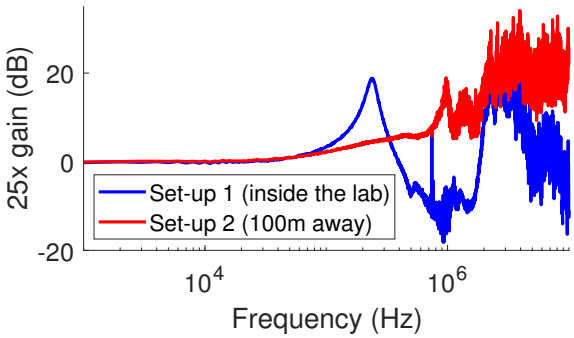

FIGURE D.4: Complete transfer functions computed for the HV laboratory test.

FIGURE D.5: Lightning impulse generator used in the laboratory tests.

FIGURE D.6: MV CT tested during the tests.

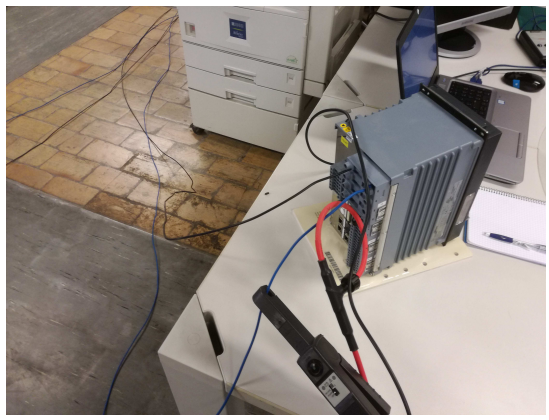

FIGURE D.7: Current measurement taken 100m away from the experiment, at the protection relay.

Bibliography

[1] L. Phillipot. "Parameter estimation and error estimation for line fault location and distance protection in power transmission systems". PhD thesis. Université Libre de Bruxelles, 1996.

[2] L. Van der Sluis. *Transients in Power Systems*. Vol. 6. 2001. ISBN: 0471486396.

[3] A. Greenwood. "Travelling waves and other transients on transmission lines". In: *Electrical Transients in Power Systems*. John Wiley & Sons Ltd, 1991, pp. 233–299.

[4] M. Bollen. "On travelling-wave-based protection of high-voltage networks". PhD thesis. Technische Universiteit Eindhoven, 1989.

[5] L. V. Bewley. "Traveling waves on electric power systems". In: *Bulletin of the American Mathematical Society* 48.8 (1942), pp. 527–539. ISSN: 0002-9904. DOI: 10.1090/S0002-9904-1942-07721-4.

[6] G. Krzysztof et al. "Traveling wave fault location in power transmission systems: an overview". In: *J. Electrical Systems* 3.7 (2011), pp. 287–296.

[7] P. F. Gale et al. "fault location based on travelling waves". In: *IEE DPSP conference*. 1993.

[8] *SEL-411L Guideform Specification*.

[9] D. Cole, M. Diamond, and A. Kulshrestha. *Fault Location & System Restoration*. 2012.

[10] ISA. *TFS-2100 Traveling Wave Fault Location*. 2010.

[11] Alstom. *Reason RPV311*. 2014.

[12] P. F. Gale, P. Naidoo, and C. Hitchins. "Travelling wave fault locator experience on Eskom's transmission network". In: *Developments in Power System Protection, 2001, Seventh International Conference on (IEE)*. 2001, pp. 1–4.

[13] Stephen Marx et al. "Traveling Wave Fault Location in Protective Relays : Design , Testing , and Results". In: *16th Annual Georgia Tech Fault and Disturbance Analysis Conference*. Georgia, 2013, pp. 1–14.

[14] P.F. Gale, J Stokoe, and P A Crossley. "practical experience with travelling wave fault locators on scottish power 227 & 400 kV transmission system". In: *IEEE- DPSP*. 1997.

[15] H Mustafa and D W P Thomas. "Comparison of Simulated and Recorded Transients for Travelling Wave Fault Location". In: *Bologna PowerTech Conference* (2003), pp. 8–11.

[16] H.W. Dommel. "Overhead line parameters from handbook formulas and computer programs". In: *IEEE Transaction on Power Apparatus and Systems* 104.2 (1985), pp. 366–372.

[17] O.P. Hevia. *Alternative Transients Program - Comparison of transmission line models*.

[18] J.R. Marti. "Accurate modelling of frequency-dependent transmission lines in electromagnetic transient simulations". In: *IEEE Transactions on Power Apparatus and systems* 101.I (1982), pp. 147–157.

[19] A. Elhaffar. "ATP/EMTP Transmission Line Model". PhD thesis. Helsinki university of technology, 2008, pp. 51–56. ISBN: 9789512292448.

[20] D.A. Douglass. "Current transformer accuracy with asymmetric and high frequency fault currents". In: *IEEE Transactions on power apparatus and systems* PAS-100.3 (1981), pp. 1006–1012.

[21] A. Elhaffar and M. Lehtonen. "Effect of current transformer transient models on the detection of traveling waves". In: *LESCOPE'06: 2006 Large Engineering Systems Conference on Power Engineering - Conference Proceedings* (2007), pp. 158–161. DOI: 10.1109/LESCPE.2006.280380.

[22] M. A. Redfern et al. "A Laboratory Investigation into the use of MV Current Transformers for Transient Based Protection". In: *International Conference on Power systems Transients*. 2003.

[23] D.J. Spoor, J. Zhu, and P. Nichols. "Filtering effects of substation secondary circuits on power system traveling wave transients". In: *2005 International Conference on Electrical Machines and Systems*. Ieee, 2005, 2360–2365 Vol. 3. ISBN: 7-5062-7407-8. DOI: 10.1109/ICEMS.2005.202992.

[24] G. Zhang, H. Shu, and Y. Liao. "Automated double-ended traveling wave record correlation for transmission line disturbance analysis". In: *Electric Power Systems Research* 136 (2016), pp. 242–250. ISSN: 03787796. DOI: 10.1016/j.epsr.2016.02.023.

[25] A. Abur and F.H Magnago. "Use of time delays between modal components in wavelet based fault location". In: *International Journal of Electrical Power & Energy Systems* 22.6 (2000), pp. 397–403. ISSN: 01420615. DOI: 10.1016/S0142-0615(00)00010-7.

[26] O. Altay, E. Gursoy, and O. Kalenderli. "Single end travelling wave fault location on transmission systems using wavelet analysis". In: *2014 ICHVE International Conference on High Voltage Engineering and Application* (2014), pp. 1–4. DOI: 10.1109/ICHVE.2014.7035486.

[27] M. da Silva, M. Oleskovicz, and D. V. Coury. "A hybrid fault locator for three-terminal lines based on wavelet transforms". In: *Electric Power Systems Research* 78.11 (2008), pp. 1980–1988. ISSN: 03787796. DOI: 10.1016/j.epsr.2008.03.027.

[28] J. Guo et al. "Global-Sensitivity-Based Theoretical Analysis and Fast Prediction of Traveling Waves With Respect to Fault Resistance on HVDC Transmission Lines." In: *IEEE Transactions on Power Delivery* 30.4 (2015), pp. 2007–2016. ISSN: 08858977.

[29] Aoyu Lei et al. "A Novel Current Travelling Wave Based Single- ended Fault Location Method for Locating Single- phase-to-ground Fault of Transmission line". In: (2015), pp. 0–5.

[30] Haike Liu et al. "Improved traveling wave based fault location scheme for transmission line". In: *Electric utility deregulation and restructuring and power technologies*. 2015, pp. 5–10. ISBN: 9781467371063.

[31] Yadong Liu et al. "A Traveling Wave Fault Location Method for Earth Faults Based on Mode Propagation Time Delays of Multi-measuring Points". In: *Electrical Review* 3 (2012), pp. 254–258.

[32] F. V. Lopes and W. L. A. Neves. "Fault Location on Transmission Lines Based on Travelling Waves". In: *International Conference on Power systems Transients*. Delf, 2011.

[33] J.a.P. Moutinho et al. "Traveling wave fault location applied to high impedance events". In: *12th IET International Conference on Developments in Power System Protection (DPSP 2014)* (2014), pp. 6.2.4–6.2.4. DOI: 10.1049/cp.2014.0047.

[34] E.O. Schweitzer et al. *Locating Faults by the Traveling Waves They Launch*.

[35] C.L. Wadhwa. "Transients in Power Systems and Insulation Co-ordination". In: *High voltage engineering*. New age international (P) Limited, 1994, pp. 208–266. ISBN: 81-224-0613-0.

[36] R. Razzaghi et al. “Locating Lightning-Originated Flashovers in Power Networks using Electromagnetic Time Reversal”. In: *International Conference on Power Systems Transients*. 2017.

[37] J C Maun. *Surtension (lecture notes)*.

[38] W.S. Meyer. “Overhead transmission lines”. In: *EMTP theory book*. 1981, pp. 4–72.

[39] W.C. Duesterhoeft, M.W. Schultz, and E. Clarke. “Determination of Instantaneous Currents and Voltages by Means of Alpha, Beta, and Zero Components”. In: *Transactions of the American Institute of Electrical Engineers* 70.2 (1951), pp. 1248–1255.

[40] A. Elhaffar. “Power transmission line fault location based on current traveling waves”. PhD thesis. Helsinki university of technology, 2008. ISBN: 9789512292448.

[41] J. Han and P. Crossley. “Traveling Wave Fault Locator for Mixed , Overhead , and Underground Teed Transmission Feeders”. In: *IEEJ transactions on electrical and electronic engineering* 10 (2015), pp. 383–389. DOI: 10.1002/tee.22097.

[42] G. G. Karady. “Transmission System”. In: *The Electrical Engineering Handbook*. 2001, pp. 115–217. ISBN: 0849385784.

[43] L.M. Wedepohl. “Application of matrix methods to the solution of travelling-wave phenomena in polyphase systems”. In: *Proceedings of the Institution of Electrical Engineers* 110.12 (1963), pp. 2200–2212.

[44] J. Susanto and F. Velagic. *Distributed Parameter Line Model*. URL: https://wiki.openelectrical.org/index.php?title=Distributed{_}Parameter{_}Line{_}Model.

[45] H.W. Dommel. *EMTP theory book*. Vancouver: Microtran Power System Analysis Corporation, 1992.

[46] L. Prikler and H. Hoidalen. *ATP DRAW users manual*. 2009.

[47] U.A. Bakshi. “Transmission line theory”. In: *Telecommunication Engineering*. Technical publications pune, 2009, 1–1:1–61.

[48] T.F.R.D. Martins, A.C.S. Lima, and S. Carneiro. “Effect of approximate impedance formulae on the accuracy of transmission line modelling”. In: *IET Gener. Transm. Distrib.* 1.4 (2007), pp. 534–539. DOI: 10.1049/iet-gtd.

[49] A. Ametani and T. Kawamura. "A Method of a Lightning Surge Analysis Recommended in Japan Using EMTP". In: *IEEE transaction on power delivery* 20.2 (2005), pp. 867–875.

[50] Z.Q. Bo, M.a. Redfern, and G.C. Weller. "Positional protection of transmission line using fault generated high frequency transient signals". In: *IEEE Transactions on Power Delivery* 15.3 (2000), pp. 888–894. ISSN: 08858977. DOI: 10.1109/61.871348. URL: http://ieeexplore.ieee.org/lpdocs/epic03/wrapper.htm?arnumber=871348.

[51] S. Abdulwadood Ali. "Modeling of Power Networks by ATP-Draw for Harmonics Propagation Study". In: *Transactions on electrical and electronic materials* 14.6 (2013), pp. 283–290.

[52] C.Y. Evrenosoglu and A. Abur. "Travelling wave based fault location for teed circuits". In: *IEEE Transactions on Power Delivery* 20.2 (2005), pp. 115–1121.

[53] X. Bustamante-Mparsakis et al. "Travelling Wave Fault Location Based on Pattern Recognition". In: *IEEE PES PowerTech Conference*. 2017.

[54] P.A. Crossley and P.G. McLaren. "Distance protection based on travelling waves". In: *IEEE Transactions on Power Apparatus and Systems* 102.9 (1983), pp. 2971–2983.

[55] B.S. Everitt and D.C. Howell. "Least Square Estimation". In: *Encyclopedia of Statistics in Behavioral Science, Volume 2*. Ed. by John Wiley & Sons Ltd. Chichester, 2005, pp. 1041–1045.

[56] A.B. Williams. *Active Filter Design*. Artech House on Demand, 1975.

[57] E. Gockenbach. "Basic testing techniques". In: *High voltage engineering and testing*. Ed. by Hugh M. Ryan. 2nd editio. London: The institution of Electricat Engineers, 2001, pp. 503–532.

[58] M. Aguet and M. Lanovici. "Générateurs de hautes tensions transitoires". In: *Traité d'électricité volume XXII: Haute tension*. Suisse: Editions Georgi, 1982, pp. 157–190.

[59] E. Kuffel, W.S. Zaengl, and J. Kuffel. "Generation of high voltages". In: *High Voltage Engineering: Fundamentals (second edition)*. Elsevier Ltd, 2000. ISBN: 978-0750636346.

[60] C.L. Wadhwa. "Transients in power systems and". In: *High voltage engineering*. New age international (P) Limited, 2007. ISBN: 9788122423235.

[61] *IEC 60060-1:2010: High-voltage test techniques - Part I: General definitions and test requirements*. Tech. rep. 2010.

[62] Eupen cables. *LV power cables datasheet*. 2017.

[63] Siemens AG. *SIPROTEC 5 Protection , automation , and monitoring*.

[64] Pico Technology. *PicoScope 4824*. 2014.

[65] Power Electronic. *CWT specification*. 2010.

[66] X. Bustamante-Mparsakis and J C Maun. "Fault Locator Using Travelling Waves : Experience in the Belgian Transmission Network". In: *International Conference on Power Systems Transients*. 2017.

[67] X. Bustamante-Mparsakis and J.C. Maun. "Travelling Wave Fault Location Based on Pattern Recognition : Application to Complex Topologies and Field Records". In: *Protection, Automation and Control world, Wroclaw*. 2017.

[68] Testec. *TT-SI 9001 / TT-SI 9002 instruction manual*.